Chemistry on Graphene

Dissertation submitted for the degree of

Doctor rerum naturalium
(Dr. rer.nat.)

to

the Faculty of Mathematics and Natural Science

by

Gerardo Algara Siller

Ilmenau University of Technology

2014

urn:nbn:gbv:ilm1-2014000459

1. Gutachterin Prof. Dr. Ute Kaiser

2. Gutachter apl. Prof. Dr. Uwe Ritter

3. Gutachter apl. Prof. Dr. Lothar Spieβ

Tag der Einreichung: 09.07.2014
Tag der wissenschaftlichen Aussprache: 08.12.2014

Kurzfassung

Das hohe Auflösungsvermgen moderner Transmissions-Elektronenmikroskope (TEM) unter einem Ångstrom ermöglicht die Untersuchung von Materialien auf atomarer Ebene. Mit dem TEM können sowohl die atomare Struktur als auch dynamische Prozesse direkt beobachtet und damit Rückschlüsse auf physikalische und chemische Eigenschaften gezogen werden. Diese Arbeit beschäftigt sich mit der Untersuchung und Charakterisierung von Graphen - einer einlagigen Kohlenstoffschicht mit herausragenden physikalischen und chemischen Eigenschaften - mit Hilfe unterschiedlicher TEM Verfahren. Einerseits konnte die Qualität von unterschiedlich hergestellten Graphen-Proben an Hand von Strukturuntersuchungen verglichen werden. Andererseits wurden die Einsatzmöglichkeiten von Graphen als Träger- und Schutzschicht, Ausgangsmaterial, Substrat, sowie als Nano-Behälter untersucht. Als Trägermaterial wurde Graphen für Nanoteilchen verwendet, welche für biologische Anwendungen konzipiert wurden. Um geeignete Proben für TEM Untersuchungen herzustellen, waren Oberflächenpräparation und Optimierung der Transfermethode entscheidend. Die TEM Untersuchungen an Nanoteilchen (Au NCs, QDs und Nano-Diamanten mit atomaren Fehlstellen) auf Graphen ermöglichten eine direkte Beschreibung ihrer atomaren Struktur, Größe und Größenverteilung. Untersuchungen von DNA auf Graphen zeigten, dass die Abbildung von biologischen Proben auf Graphen-Trägermaterialen mittels TEM möglich ist. Des Weiteren konnte nachgewiesen werden, dass Graphen auch als Schutzschicht für strahlempfindliche Materialien, wie z.B. g-C_3N_4 oder MoS_2, geeignet ist und damit die Abbildung dieser Proben in ihrem ursprünglichen Zustand erlaubt. In Bestrahlungexperimenten konnten einwandige Kohlenstoff-Nanoröhrchen aus einer Graphen-Doppellage geformt werden. In einem weiteren Experiment gelang es aus den Adsorbaten auf Graphen eine weitere Graphen-Lage (in-situ) unter Elektronenbeschuss zu wachsen. Weitere Experimente an Wasser, das zwischen zwei Graphen-Lagen eingeschlossen wurde (nano-confinement), erlaubten erstmals die direkte Beobachtung und Charakterisierung einer neuen Modifikation von Eis bei Zimmertemperatur: dem “square ice”. Nicht zuletzt wurde im Rahmen dieser Arbeit eine neue Methode zur Säuberung von Graphen-Oberflächen von Adsorbaten mit Hilfe von Adsorptionsmitteln entwickelt, dem sogenannten “dry-cleaning”.

Abstract

State-of-the-art transmission electron microscopes (TEMs) are capable to achieve sub-ångstrom resolution. Therefore matter can be studied at the atomic level, i.e., with a TEM the atomic structures and processes can be observed, consequently physical and chemical properties can be derived. In this work, graphene, one atom thick material with outstanding physical and chemical properties, has been thoroughly characterised by different TEM techniques. The structural description of graphene allowed us to compare graphene samples fabricated by different methods and to assess their quality. Furthermore, graphene has been used as a substrate, protective layer, raw material, surface template and nano-confiner. Graphene substrates were used to support nano-objects which were designed for biological applications. Treatments of the graphene substrates prior to sample deposition as well as sample deposition techniques provided the means to obtained samples suitable for TEM investigations. The TEM studies in nano-objects (Au NCs, QDs, nanodiamond with NV centres), deposited on graphene, resulted in the characterisation of their structure, size and dispersion. DNA deposited on graphene was also investigated by TEM. The results showed that the approach of using graphene as substrate can be used to image the structure biological samples. It is presented also in this thesis that graphene can protect radiation sensitive materials such as g-C_3N_4 and MoS_2 from the electron beam, allowing imaging these materials in their pristine state. By using the electron beam to nano-engineer bilayer graphene it was possible to create single-walled carbon nanotubes. In another experiment, graphene served as surface template where an adlayer graphene grew from residual contamination during imaging. Experiments with water trapped between graphene layers (nano-confinement) resulted in the detection, observation and characterisation of a new form of ice at room temperature, i.e. square ice. Additionally, atomically clean graphene was obtained by the development of a new cleaning method using adsorbents — dry-cleaning —.

Contents

§ 1 Introduction

> By the means of Telescopes, there is nothing so far distant but may be represented to our view; and by the help of Microscopes, there is nothing so small, as to escape our inquiry; hence there is a new visible World discovered to the understanding.
>
> Robert Hooke. *Micrographia or some physiological descriptions of minute bodies made by magnifying glasses: with observations and inquires thereupon.* London: J. Martyn and J. Allestry, 1665.

Aiming to understand nature to its smallest units, humanity has been developing instruments capable of revealing the finest details of matter, e.g. microscopes. The power of a microscope, i.e. resolution, is directly proportional to the wavelength of the light source. Therefore, the smaller the wavelength of the source, the smaller the distance that can be resolved between two objects by the microscope. Following this criterion, Ruska and Knoll developed a microscope, that instead of light uses electrons, i.e. electron microscope, therefore highest resolution is achieved. Nowadays, electron microscopes are a key tool in scientific research, because with microscopes we do not only observe details but we are able to describe the structure of materials up to the atomic level as well as their physical and chemical properties.

> One of the principles of chemistry is to study the transformations of matter "and one of the key chemical concepts is the Structure-Properties relationship, if we understand the structure we can understand the chemical, physical and biological properties and, therefore, can control the transformations of matter."[i]

Materials can be categorized by their size, i.e., from the macroscopic over the nanoscopic level down to the single atom level, and it is the size that defines the properties of the materials. For example, graphene, just one atom thick material, exhibits new and unexpected properties than those of graphite. For this reason, in the past decade, graphene has been modelled and characterised, its properties have been tested and measured, and many of its structure-properties relationships have been unveiled.

[i] Dr. Andrei Khlobystov. Private communication. 2013

An instrument that has provided means to understand the structure of graphene is the transmission electron microscope (TEM). Therefore, a summary on the theory of transmission electron microscopy is the starting point of this thesis (Chapter 2).

In Chapter 3, transmission electron microscopy techniques have been used to characterise graphene samples which were fabricated by different methods. The samples investigated were micromecachanical cleaved graphene and graphene grown on copper foils by chemical vapour deposition. For the latter, a new method to transfer graphene to a TEM grid has been developed in order to avoid residual polymer contamination on the samples. The TEM characterisations resulted in the full structural description of these graphene samples.

Hybrid nano-objects can be used in many biological applications, e.g. drug delivery, biolabeling or biosensors. Due to their sizes, nano-objects have to be deposited on a substrate (grid) to be imaged in the TEM. Grids made of continuous amorphous carbon films are common substrates used to image nano-objects, but the signal from the carbon film is too strong that in some cases it obscures the signal of the nano-objects. Graphene is a material with minimal signal contribution, hence graphene is used as a substrate to study nano-objects such as Au nanoclusters, quantum dots and nanodiamond with a nitrogen-vacancy defect centres (Chapter 4).

Molybdenum disulfide (MoS_2) and graphitic-carbon nitride (g-C_3N_4) are two dimensional materials which have an intrinsic band-gap. This band gap is the reason why these materials are of great interest for electronic applications. These two dimensional materials are radiation sensitive, e.g. the electron dose that these materials can sustain before structural damage takes place is low, therefore the characterisation of their pristine structure using a TEM has been challenging. In transmission electron microscopy, an approach to reduce radiation damage is the use of a protective layer. Graphene with its low signal contribution to the image, its mechanical, electrical and chemical properties is, thus, the most suitable material to protect radiation sensitive materials. Hence, in Chapter 5, graphene is used as a protective layer to investigate the pristine structure of MoS_2 and g-C_3N_4.

Graphene does not only protect materials from radiation damage, it can also be used, as it is demonstrated in Chapter 6, as raw material, as a surface template

or as nano-confiner to create new structures, i.e. single-walled carbon nanotubes, adlayer graphene and square ice.

Methods for producing and transferring graphene, and exposure to air render its surface contaminated. The contamination on graphene (mostly hydrocarbons) is not desirable because it hinders some structural details or properties of graphene or any other materials deposited on graphene that could be characterised by TEM. A new method to clean graphene (dry-cleaning) is reported in Chapter 7, where porous materials, adsorbents, have been used to remove the contamination from the graphene surface. The characterisation of the dry-cleaned samples by TEM denotes the high efficiency of the method.

§ 2 Background

2.1 High Resolution Transmission Electron Microscopy

The purpose of a transmission electron microscope (TEM) is to illuminate with an electron beam an electron transparent specimen, the result of this interaction is magnified and then recorded on a detector. For that a TEM is constituted, basically, by: electron gun (tip and accelerator), condenser system, stage, objective lens, projection system and recording device. To generate an electron beam, conduction electrons have to be extracted from a crystalline material, i.e. tip (cathode). For an electron to be emitted it should overcome the work function of the tips material. There are 3 types of electron emission in TEM, thermionic, Schottky, and field emission. Thermionic emission is made by heating the tip, thus the electrons have enough kinetic energy to overcome the work function. Schottky emission is made by applying an electric field to the tip decreasing the work function of the material and by heating to give kinetic energy to the electrons to escape in to vacuum. In field emission, the work function is decreased by applying a strong electric field until the work function is lowered to the point that the electrons then escape the material by quantum-mechanical tunneling effect. The electrons once in vacuum travel towards the anode, then the electrons are accelerated gaining kinetic energy proportional to the voltage applied between anode and cathode. Most microscopes work within 80-300 kV acceleration voltages. The electron beam then passes through the condenser system. This system has at least two lenses, C1 and C2. C1 is used to control the electron beam current and C2 to control the convergence or divergence of the beam or get parallel illumination. At the sample stage, the electron beam interacts with the specimen and exit. The electron beam is, then, focused and magnified by the objective lens and the image is formed. Thereafter, the image is transferred and further magnified by the projector system to be acquired by a recording device (CCD).

There are many techniques within electron microscopy and each technique is used to obtain specific features from a specimen. High resolution transmission electron microscopy (HRTEM) is one technique which enables atomic-resolution, thus struc-

tural features, e.g. atom positions, of the specimen can be obtained. The basics of HRTEM image formation will be describe in the next section (in the context of the weak phase object approximation), thereafter the resolution achievable by HRTEM, the radiation damage caused by electrons, and the challenges in sample preparation for HRTEM will be discussed.

Image formation

The following sections are a summary on the theory of TEM, thus these sections are based on published literature and, mostly, on the books:

> Rolf Erni. Aberration-corrected imaging in transmission electron microscopy, Imperial College Press, London, 2010
>
> Ludwig Reimer and Helmut Kohl. Transmission electron microscopy, Springer Science+Business, New York, 2008.

Image formation in HRTEM can be described in a simplified form as an incident electron wave that goes through the specimen. Then, the wave at the exit surface of the specimen, exit-plane wave, now carries the information of the specimen, and this exit-plane wave is transferred by the objective lens to the image plane. The incident electron wave is described by a plane wave. If the specimen is taken as a phase object, the amplitude of the incident electron wave is not changed but the phase of the electron wave is modulated. The phase modulation can be written as exp(-i$\phi(r)$), where:

$$\phi(r) = \frac{\pi}{\lambda U} V_t(r) \qquad \text{U} = \text{acceleration voltage} \tag{2.1}$$

$$V_t(r) = \text{projected electrostatic potential}$$

$$\lambda = \frac{hc}{\sqrt{2EE_0+E^2}} \qquad \lambda = \text{relativistic wavelength of the electrons} \tag{2.2}$$

$$h = \text{Planck}'\text{s constant}$$

$$c = \text{speed of light}$$

$$E = \text{kinetic energy of the electrons}$$

$$E_0 = \text{rest energy of the electrons}$$

If the specimen is taken now as a weak phase object then $\phi(r) << 1$, and thus the expanded phase modulation is exp(-i$\phi(r)$) $\approx$ 1-i$\phi(r)$. The product of the plane wave

by the expanded phase modulation by the object results in the exit-plane wave:

$$\psi_{ep}(r) = 1 - i\phi(r); \quad \text{Weak phase object approximation.} \tag{2.3}$$

Although the weak phase object approximation applies only to very thin materials, usually, at higher voltages than 80 kV it helps to understand the origin of image contrast in HRTEM.

The exit-plane wave can be also described as a set of diffracted partial beams that experienced the crystal potential. Every diffracted partial beam is transferred, i.e. focused, by the objective lens to the back focal plane and these diffracted beams form the diffraction pattern. The wave at the back focal plane, ψ_{bfp} is the Fourier transform of the exit-plane wave:

$$\psi_{bfp}(q) = F[\psi_{ep}(r)] = \psi_{ep}(q) \tag{2.4}$$

with q a two dimensional reciprocal space vector. The intensity of the diffraction spots is obtained by:

$$I_d = |\psi_{ep}(q)|^2 \tag{2.5}$$

After propagation of the electron wave from the back focal plane, $\psi_{ep}(q)$, to the image plane, $\psi(r)$, the transfer characteristics of the objective lens are noticeable. So the wave function at the image plane is expressed by:

$$\begin{aligned} \psi(r) &= F^{-1}[\psi_{ep}(q)t(q)] & (2.6)\\ &= \psi_{ep}(r) \otimes t(r) & (2.7) \end{aligned}$$

where the $t(q)$ (complex transfer function) describes the characteristics of the microscope, and $\otimes$ is the convolution. If we substitute equation 2.3 (weak phase object approximation) in 2.7 then the electron wave at the image plane is:

$$\psi(r) = (1 + \phi(r)) \otimes \Im[t(r)] \; - i\phi(r) \otimes \Re[t(r)] \tag{2.8}$$

with $\Im$[t(r)] and $\Re$[t(r)] the imaginary and real parts, respectively, of the complex transfer function. The image intensity for a weak phase object approximation can be written as:

$$I(r) = |\psi(r)|^2 = (1 + 2(\phi(r)) \otimes \Im[t(r)] \tag{2.9}$$

The factors influencing the complex transfer function, $t(q)$ in equation 2.6, are: the characteristics of the objective lens, the coherence of the electron beam, the mechanical instabilities of the specimen and the TEM, and the recording process.

Because the objective lens in a TEM is non-ideal, the spatial frequencies of the phase of $\psi_{ep}(r)$ are not equally transferred to the image plane. That is, the objective lens induces, also, phase shifts. The effects of the objective lens on the complex transfer function $t(r)$ are, therefore, expressed by the transfer function ($t_l(q)$) in the form:

$$t_l(q) = \exp\left(-\frac{2\pi i}{\lambda}\chi(q)\right) \tag{2.10}$$

where $\chi(q)$ is the wave aberration function expressed by:

$$\chi(q) = \frac{1}{2}q^2\lambda^2\Delta f + \frac{1}{4}q^4\lambda^4 C_s \tag{2.11}$$

with Δf as defocus and C_s as the spherical aberration. For small angles $\mathrm{q}\lambda \approx \theta$, then the wave aberration function can be expressed, also, as a function of the scattering angle, $\chi(\theta)$:

$$\chi(\theta) = \frac{1}{2}\theta^2\Delta f + \frac{1}{4}\theta^4 C_s. \tag{2.12}$$

It is important to notice that the above described wave aberration functions does not take in account higher order aberrations, for the general wave aberration function refer to the literature.[1,2]

The image intensity (equation 2.9) for the weak phase object approximation depends on the imaginary part of the complex transfer function, hence the imaginary part of the transfer function from the objective lens $t_l(q)$ is, only, of importance. The imaginary part of $t_l(q)$ is the coherent phase contrast transfer function which is denoted by $t_c(q)$. This coherent phase contrast transfer function is obtained by the substitution of equation 2.11 in equation 2.10 and is described as follows:

$$t_c(q) = sin\left[-\pi\left(\lambda q^2\Delta f + \frac{1}{2}\lambda^3 q^4 C_s\right)\right] \tag{2.13}$$

In equation 2.13, if Δf and C_s are both zero then $t_c(q)$ is zero, thus there is no contrast in the image. To obtain the best phase contrast imaging conditions in HRTEM then the parameters of $t_c(q)$ (the objective lens) should be optimized. As $t_c(q)$ is a sine function then for $q \rightarrow 0$ the coherent phase transfer function is 0,

hence small spatial frequencies will not contribute to phase contrast imaging (see Figure 2.1.1 for $t_c(q)$).

The spherical aberration in a non corrected TEM is a constant value defined by the characteristics of the objective lens. Thus Δf can be changed to optimize the coherent phase contrast transfer function. The optimization of the defocus for the coherence phase contrast transfer function is called Scherzer condition or Scherzer focus and is expressed as:

$$\Delta f_s = -\left(\frac{4}{3}\lambda C_s\right)^{-1/2} \tag{2.14}$$

Scherzer conditions are also applied for an aberration corrected TEM, but in this case the values of the spherical aberration and high order aberrations are reduced.

The coherence of the electron beam influences also the transfer function. The coherence of the beam can be partial temporal or partial spatial. The partial temporal coherence function $E_t(q)$ is a function that depends on the focus spread (Δ_f). Where the focus spread depends on the chromatic aberration (C_c) and the energy spread of the beam. The partial temporal coherence function is:

$$E_t(q) = \exp\left(-\frac{1}{2}\pi^2\Delta_f^2\lambda^2q^4\right) \tag{2.15}$$

$$\Delta_f = C_c\sqrt{\left(\frac{\Delta U}{U_0}\right)^2 + 4\left(\frac{\Delta I}{I_0}\right)^2 + \left(\frac{\Delta E_{rms}}{E_0}\right)^2} \tag{2.16}$$

where $\frac{\Delta U}{U_0}$ and $\frac{\Delta I}{I_0}$ are the instabilities of the high tension and lens current, respectively, and ΔE_{rms} is the root mean square of the energy spread of the electron beam. The function $E_t(q)$ produces a damping envelope which results from the dependence of defocus on the wave aberration function, i.e., the damping of high spatial frequencies in the image.

The partial spatial coherence function, another characteristic of the TEM, is due to finite size of the electron source. In consequence, the electron beam consists of partial waves with different wave vectors diverging with a semi-angle θ_s, thus each partial wave produces a partial image. The partial spatial coherence function is thus expressed by:

$$E_s(q) = \exp\left[-\pi^2\theta_s^2\left(q^2\Delta f^2 + 2\lambda^2q^4\Delta f C_s + \lambda^4q^6{C_s}^2\right)\right] \tag{2.17}$$

Another contribution to the transfer function is the effects of the objective aperture by $t_a(q)$. Since HRTEM investigations are normally done without objective aperture this function is consider 1.

The product of all contributions to the transfer function in the frequency spectrum is the phase contrast transfer function for partial coherent illumination:

$$t(q) = t_a(q)t_c(q)E_t(q)E_s(q). \tag{2.18}$$

With this equation it is possible to characterized the resolving power — resolution — of a transmission electron microscope. The individual contributions to the contrast transfer function and the contrast transfer function have been plotted in Figure 2.1.1. This plot takes in account the experimental and microscope values (i.e. Aberration-corrected TITAN 80-300) used in this thesis.

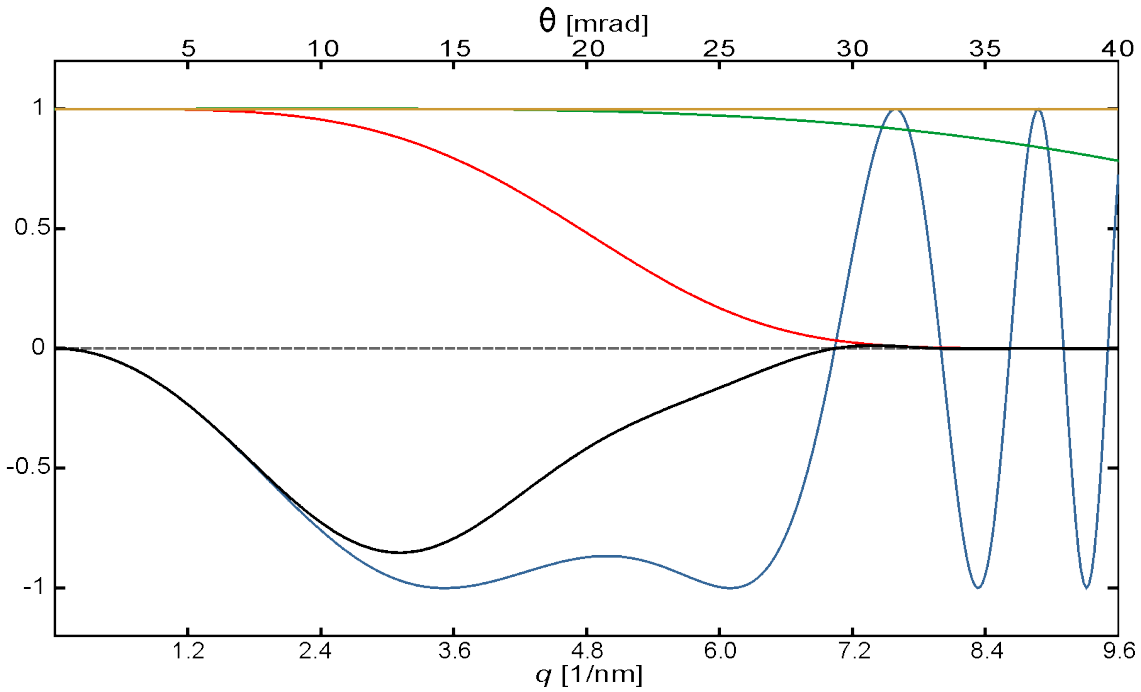

Figure 2.1.1. Phase contrast transfer function and its individuals contributions ($t_a(q)$ yellow, $E_s(q)$ green, $E_t(q)$ red, $t_c(q)$ blue and $t(q)$ black. The values used to obtain the contrast transfer function are: E= 80 keV, Δf=-129 Å, C_s=0.03 mm, Δ_f=40 Å, θ_s=0.5 mrad, λ=4.017 pm).

The information transferred by the microscope under the described settings reaches up to $q \approx$7.2 nm^{-1}.

Resolution

The smallest distinguishable distance between two discreet objects.

Diffraction-limited resolution

Using Abbe's formula $d = \lambda / 2\eta sin\,\alpha$ (η = refraction index and α aperture angle) is possible to derive the theoretical resolution limited by diffraction (diffraction limit) of any microscope without aberrations using the Rayleigh criterion for a circular aperture:

$$d = \frac{0.61\lambda}{sin\,\alpha} \approx 0.61\lambda \tag{2.19}$$

As seen in this approximation the diffraction-limited resolution is thus restricted mainly by the wavelength.

Point resolution

The information of the specimen that can be directly interpreted in TEM is defined by the optimization of equation 2.12 under Scherzer conditions (equation 2.14). The first zero crossing of the phase contrast transfer function under Scherzer conditions is the point resolution (d_r) and is expressed by:

$$d_r = 0.66(C_s\lambda^3)^{1/4}. \tag{2.20}$$

The point resolution then can be improved either by decreasing the wavelength of the electrons (increasing acceleration voltage, see equation 2.2) or by decreasing the value of C_s.

Another way to express the point resolution is in terms of usable angle θ_0.

$$d_r = \frac{0.61\lambda}{\sin\theta_0} \tag{2.21}$$

where the usable angle is related to the value of the spherical aberration by $\theta_0 = 0.92(\lambda/C_s)^{1/4}$.

Information limit

Partial spatial and temporal coherence functions (equations 2.17 and 2.15) damped the amplitude of the phase contrast transfer function. It is this damping envelope functions which determined the signal of high spatial frequencies that contribute to

imaging. As definition, the information limit is the spatial frequency (q) for which spatial or temporal coherence functions (E_s and E_t) reach the value $1/e^2$. Therefore the information limit (d_t) due to partial temporal coherence is:

$$d_t = \frac{1}{q_t} = \left(\frac{\pi \Delta_f \lambda}{2}\right)^{1/2} \tag{2.22}$$

and the information limit (d_s) due to partial spatial coherence deduced from setting E_s=$1/e^2$ and defocus=0 is:

$$d_s = \frac{1}{q_s} = \left(\frac{\pi^2 \theta_s^2 \lambda^4 C_s^2}{2}\right)^{1/6} \tag{2.23}$$

Specimen-limited resolution

The resolution has been described, until now, only in terms of the physical limitations of the microscope but there is also a limit on resolution imposed by the specimen. i.e. specimen-limited resolution[3] (d_m):

$$d_m = \sqrt{d_r^2 + \frac{(S/N)^2}{C^2 D}} \tag{2.24}$$

d_r = point resolution
S/N = signal to noise ratio
C = contrast
D = specimen tolerable dose

$$C_w = \frac{I_b - I_a}{I_b} \tag{2.25}$$

C_w = Weber contrast
I_b = Intensity of the background
I_a = Intensity of lattice fringes

(2.26)

where the S/N=4-5[4] and D is the electron dose which can be given to the specimen before degradation. Therefore the second term of the radical is dependent on the sample. The definition of contrast may vary according to the features of the images, for example in some cases Michelson contrast or the root mean square contrast should be apply.[5–7] The incident energy of the electrons and the sample dependence to dose will then limit the applicability of HRTEM. Next section will discuss the radiation damage mechanisms in TEM.

2.2 Radiation damage mechanisms

This section has been based in the following literature:

> David B. Williams and C. Barry Carter. Transmission electron microscopy 2nd edition. Springer Science+Business Media, New York, 2009.
>
> Florian Banhart. In-situ electron microscopy at high resolution. World Scientific Publishing, Singapore, 2008.

The interaction of electrons with atoms can be separated as electron-nucleus and electron-electron interactions. One important damage mechanism caused by electron-nucleus interaction is knock-on damage. Electron-nucleus interactions can be expressed by the energy transferred from the electron to the nucleus (E) in terms of the scattering angle (θ) by:

$$E(\theta) = E_{max}\, cos^2\,(\theta) \qquad E_{max} = \text{maximum transferred energy} \tag{2.27}$$

$$E_{max} = \frac{2E_0(E_0 + 2m_e c^2)}{Mc^2} \qquad \begin{aligned} M &= \text{mass of the nucleus} \\ E_0 &= \text{energy of the incident electron} \\ m_e &= \text{electron mass} \end{aligned} \tag{2.28}$$

The threshold energy E_T is the energy needed to displace an atom from the material by an electron-nucleus collision. Thus E_T depends on the material and is obtained by taking into account bonding, crystal arrangement and the atomic weight. If $E(\theta)$ is greater than E_T then atom displacement will occur.

The probability for an electron to be scattered is the cross section (σ) and the angular distribution of scattering from the nucleus is the differential scattering cross section ($\frac{d\sigma}{d\Omega}$ with Ω being a solid angle).[8]

$$\Omega = 2\pi(1 - cos\theta) \quad d\Omega = 2\pi sin\theta d\theta \tag{2.29}$$

Depending on the scattering process, the definition of cross section σ varies, for example Mott[9] or screened Rutherford[10] scattering. The relevant quantity (experimentally measured) in TEM is the differential scattering cross section. In TEM the

screened Rutherford differential scattering cross section is widely used:

$$\frac{d\sigma}{d\Omega} = \frac{Z^2\lambda_R^4}{64\pi^4 a_0^2}\frac{1}{\left[sin^2(\frac{\theta}{2}) + \frac{\theta_0^2}{4}\right]^2} \qquad \lambda_R = \text{relativistic wavelength} \tag{2.30}$$

$$Z = \text{Atomic number}$$

$$a_0 = \text{Bohr radius}$$

$$\theta_0 = \frac{0.117\, Z^{1/3}}{(E_0)^{1/2}} \qquad \theta_0 = \text{screening parameter}$$

from this equation is possible to obtain the total elastic cross section (σ_{el}) by integrating it over the range of scattering angles, e.g. from 0 to θ. The total elastic scattering cross section is then:

$$\sigma_{el} = 2\pi \int_0^{\theta} \frac{d\sigma}{d\Omega} sin\,\theta\, d\theta \tag{2.31}$$

The electron-electron interactions are far more complicated than the electron-nucleus interactions because there is no direct correlation to the scattering angle. Electron-electron interactions may cause electrostatic charging, specimen heating, radiolysis and mass loss. Ionization damage occurs if the energy transferred, in an electron-electron interaction, is high enough for the electron to leave the atom, that is the atom is ionized. An atom in this state may suffer subsequent damage produced by electrostatic forces, weak bonding leading to a lower threshold energy thus increasing the knock-on damage, and heating. The cross section for electron-electron interaction will depend on the critical ionization energy (E_c). To excite electrons from a shell, the electron energy E_0 should be greater than the critical energy for ionization. E_c increases for electrons closer to the nucleus, that is, an electron in the L shell will have lower E_c than an electron in the K shell. Also, as the atom increases in mass then the E_c increases proportional to Z. The cross section for ionization σ_{in} is then:

$$\sigma_{in} = \left(\frac{\pi e^4 b_s n_s}{E_0 E_c}\right) log\left(\frac{c_s E_0}{E_c}\right) \tag{2.32}$$

n_s is the number of electrons in the ionized subshell, b_s and c_s are constants for the specific shell. The lower the E_0 the higher the electron-electron interaction, hence with lower E_0 more damage due to ionization occurs. Ionization damage processes are common for organic materials, which are mostly composed of low atomic number elements and the weak steric constrains. Electronic excitation may change the

structure of the sample, bond breaking and mass loss.[i] Most of these effects are correlated to the electron dose, i.e., the number of electrons that hit the sample per area.

The knock-on damage can be avoided by decreasing the electron energy but then ionization damage is stronger. Therefore, the imaging conditions (electron energy) of the TEM have to be optimized in accordance to the type of sample.

2.3 Materials in HRTEM

As we have seen in the previous sections, the electron energy and the dose are limiting factors for resolution achieved in HRTEM. The electron energy in an aberration corrected TEM defines the point resolution (equation 2.20) of the microscope, and this electron energy is directly correlated to the knock-on damage (equation 2.27). That is, if one wants to avoid knock-on damage the electron energy should be reduced but this will result in lost of resolution and increase the probability of ionization damage (e.g. for organic and low Z materials). An increase in electron dose at low electron energies results in an increase of the specimen resolution (equation 2.24), but at the same time increases the ionization damage.

Another problem arises in HRTEM if one wants to image non periodic structures (e.g. molecules or clusters) which need to be imaged on a substrate, because the substrate contributes to noise. An increase in noise means loss of detected intensity from the specimen (i.e. contrast), hence lost of specimen resolution. It is, thus, very important the choice of substrate when imaging nanomaterials, either organic or inorganic, by HRTEM.

The requirements of a good substrate for HRTEM are:

1. As thin as possible, to reduce scattering effects from the substrate.
2. Low Z number, to lowered the signal contribution to the contrast.
3. Mechanically and thermally stable, to avoid instabilities during imaging.
4. Electronic conductor, to avoid charging.

[i] Detailed description in Chapter 11 of L. Reimer and H. Kohl. Transmission electron microscopy [1]

Graphene, which is one atom thick crystalline carbon material, possesses all mechanical, thermal and electrical properties needed for a perfect substrate for HRTEM investigations.[11] Moreover, the contribution of the graphene lattice to the image can be Fourier filtered, therefore specimens can be image as if they were free-standing in vacuum. In the next section an overlook on graphene properties is given, also the methods for fabrication of graphene are discussed, as well as the characterisation of graphene by TEM.

§ 3 Graphene

This chapter gives a basic overview of the main characteristics of graphene and its physical properties to its increasingly importance in research; Explains the fabrication and transfer processes and characterization methods. In particular it is discussed the TEM techniques to characterise graphene from the microscopic to the atomic regime.

3.1 On the structure of graphene

The two dimensional form of carbon, graphene , was studied *theoretically* long before its discovery,[12] because it signified the starting point for calculations of properties of graphite.[13] The discovery of graphene , has overcome its theoretical expectations and its projected applicability and usefulness in many areas of research and nanotechnology.

A carbon atom has four electrons available for bonding and can be distributed in three types of bonding configurations: sp, sp^2 and sp^3. The sp hybridized bond is linear, usually found in long carbon chains. The sp^3 distribution is tetrahedral, i.e. a carbon atom has four neighbouring atoms as the carbon atoms in diamond. In graphene, from those four electrons three are hybridized in a sp^2 state allowing the creation of σ bonds with three neighbouring carbon atoms. These bonds distribute at 120° angles forming a trigonal planar structure, whence the known honeycomb like structure. The fourth electron arranges in a p_z orbital perpendicular to the plane, enabling π bonding and becoming delocalised by lateral overlapping. The C-C bonds in graphene are, therefore, conjugated bonds with a length of 1.42 Å. The crystal structure of graphene is hexagonal and consists of two atoms per unit cell with lattice parameters of a=b=2.46 Å (Figure 3.1.1). From the arrangement of the carbon atoms in graphene and its unique binding, graphene possesses extraordinary structural, electrical and chemical properties.[14–17]

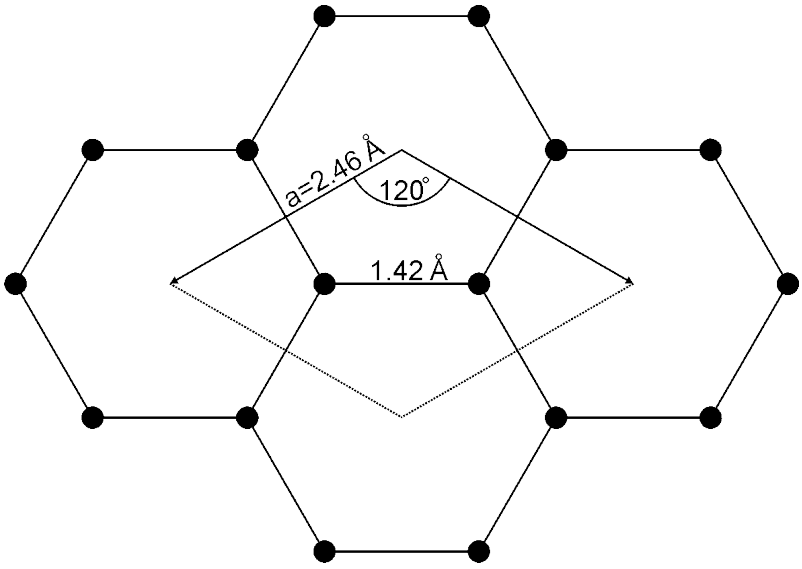

Figure 3.1.1. Structure of graphene. Each carbon atom in graphene is bonded to three other C atoms, with a bond length of 1.42 Å. From this hexagonal lattice the in plane lattice parameters of graphene are a=b=2.46Åand γ=120° .

3.2 Graphene fabrication

The interlayer binding of the graphene sheets in graphite is van der Waals, which is a weak force in comparison to the force binding the atoms in the plane. Accordingly, it is easier to separate the graphene layers than break the C-C bonds in the plane. Novoselov et al.[12] achieved to observe, select and characterise graphene by cleaving graphite using adhesive tape and depositing it on SiO_2. Other groups have worked in the fabrication of graphene, to make its production scalable, using different approaches: liquid phase exfoliation, anionic bonding, carbides sublimation and chemical vapour deposition on metals.[18] But every fabrication process produces different graphene quality, i.e., crystallinity, size of the graphene flakes and intrinsic defects. Also, some fabrication processes produce multilayer graphene. Thus each graphene grown by an specific fabrication method gives the material different properties and, therefore, applicability.

Micromechanical cleaved graphene

The fabrication of micromechanical cleaved graphene (MC-graphene) is a top-bottom process. The binding van der Waals energy in-between layers of graphite[19] is about 2 eV/nm^2 which means, according to Zhang et al.,[20] that the force needed to separate two layers of graphite with an area of 1 μm^2 is around 300 nN which is, indeed,

small and reachable by mechanical means, for example friction of graphite on paper, an AFM cantilever or peeling layers with adhesive tape.

MC-graphene is fabricated with a portion of natural graphite glued to a tape, and repetitively cleaved. Then, an area on the tape is put in contact to SiO_2 surface and pealed off leaving graphene flakes on the SiO_2. By means of an optical microscope the prepared sample can be investigated. Graphene has a refractive index of $n = 2.6 - 1.3i$ which is independent on the λ, but SiO_2 and Si refractive indexes are dependent on λ, thus the relative intensity of the reflected light from the substrate, I(1), and through graphene, $I(n_1)$ is:

$$C = \frac{I(1) - I(n_1)}{I(1)} \tag{3.1}$$

The contrast expected (C) for single-layer graphene in the green region of the visible spectrum is about 12% for a 90 nm SiO_2 substrate.[21] If the optical microscope has not a wavelength selector, it is still possible to, approximately, check the contrast by splitting a RGB image in channels and corroborate the contrast by a line profile.[i] The typical size of a single-layer MC-graphene sample is 10μm.

Graphene grown by chemical vapour deposition (CVD-graphene)

Contrary to MC-graphene, the growth of graphene by chemical vapour deposition is a bottom-up process. Depending on the substrate used to grow graphene the mechanisms in its formation varies. For example, the growth of CVD-graphene on nickel is mediated by surface segregation due to the high solubility of C on Ni, whereas on copper, the graphene grows by a surface-catalysed process.[22] The highest quality CVD-graphene, e.g. big grains consisting mostly of single-layer graphene, has been achieved by growing it on copper substrates.[23] But the growth of CVD-graphene on Cu is strongly influenced by the carbon source (solid, liquid or gas), the pressure, and the temperature rates at which is heated and cooled. The size of a CVD produced graphene is as big as the Cu substrate, e.g. cm.

The CVD-graphene used in this work comes from 3 different sources:

- Commercial CVD-graphene[ii] grown on Cu at low pressure and methane as carbon source.

[i] Master thesis: G. Algara-Siller. Graphene - preparation methods and characterisation. Ulm University 2008

[ii] Graphenea S.A.

- Liquid phase CVD-Graphene using ethanol as carbon source at atmospheric pressure.[iii]
- CVD-graphene grown with low pressure and methane.[iv]

Transfer of graphene to TEM grids

MC-graphene transferred to TEM grids

MC-graphene after been deposited and spotted on the SiO_2 substrate is transferred to a TEM grid (Quantifoil) via potassium hydroxide (KOH)[24] to be, then, characterised by TEM. This transfer method consists of bringing the TEM grid into contact to the graphene by the evaporation of isopropyl alcohol. Once the grid is in contact with the graphene then the grid with MC-graphene is detached from the SiO_2. This process is possible by etching the SiO_2 with KOH. After transfer the sample has to be rinsed in distilled water to remove remaining KOH.

CVD-graphene transferred to TEM grids

The transfer of graphene grown on Cu by CVD is a variation and optimisation of the method reported by Pantelic et al.[25]

Materials

1. 3 low form beakers (200 mL) with spout.
2. Ammonium peroxodisulfate (APS).
3. Demineralized and deionized (DI) water.
4. Isopropyl alcohol (IPA).
5. TEM grids (Au Quantifoil, 1.2 ⊘)
6. Graphene grown on Cu by CVD
7. Stainless steal mesh.

[iii] Fabricated by Dr. Jessica Campos-Delgado, ICTEAM, Université Catholique de Louvain, Louvain-la-Neuve, Belgium

[iv] Fabricated by Dr. Jessica Campos-Delgado, ICTEAM, Université Catholique de Louvain, Louvain-la-Neuve, Belgium

Solutions

1. (Beaker 1) 8 grams APS diluted in 100 mL DI water.
2. (Beaker 2) 200 mL DI water.
3. (Beaker 3) 100 mL isopropyl alcohol.

Pre-etching one side of Cu foil

(This step is made to remove graphene from one side of the Cu foil. The Cu foil should be as flat as possible. To flatten the Cu foil use 2 glass slides.)

1. Float the Cu foil with the desired graphene side upwards in APS for 5 minutes.
2. Fish the Cu foil from APS with the mesh and rinse it in DI water.
3. Dry the Cu foil in filter paper.

Transfer

(The Cu foil should be as flat as possible. To flatten the Cu foil use 2 glass slides.)

1. Place grids on the graphene with IPA and let dry, avoid overlapping of the grids.
2. Check the contact of the grids with optical microscope.
3. Float the grid/graphene/Cu on APS (grid side up).
4. Let to etch until Cu has been removed.
   (Normally takes 5 hours for 25 μm thick copper. Is recommended to let etch over night but no more than 24 hrs, otherwise the grid is destroyed.)
5. Tap each grid from the top to improve the contact of the grid with graphene.
6. Fish each grid with the stainless steal mesh.
7. Rinse the grid in DI water and then IPA.
8. Let the grid dry on filter paper with the graphene side up.
9. Check the transferred graphene by optical microscope.

3.3 Experimental imaging conditions

Throughout this work, the used instrumental and experimental TEM conditions were the following:

- E= 80 keV
- λ= 4.017 pm
- Δf$\approx$ -129 Å (Scherzer)
- $C_s \approx$ 0.03 mm
- Δ_f= 40 Å
- θ_s= 0.5 mrad

If these values are substituted in to the equations (2.19, 2.20, 2.22, 2.23), the obtained diffraction-limited resolution (d) is 0.025 Å; the information-limited resolution due to temporal coherence (d_t) $\approx$ 1.6 Å and spatial coherence $d_s \approx$ 0.9 Å; and the point resolution (d_r) after C_s correction is $\approx$ 1.43 Å.

3.4 Characterisation of graphene by TEM

The produced graphene samples were investigated in the TEM at an acceleration voltage of 80 kV. At this voltage, the corresponding energy of the electrons is sufficiently small that, for defect-free graphene, the probability to sputter an atom by knock-on damage mechanism is minimal.[26] Also, as graphene is a good electrical conductor ionization damage is not existent. Thus, a high electron dose rate can be used. With a very high dose rate, the specimen-limited resolution can reach the value to the point resolution.

Characterisation of graphene by selected area electron diffraction

By using selected area electron diffraction technique an electron diffraction pattern (SAED pattern) can be recorded from a defined area of the specimen. Because an SAED pattern contains all scattered electrons, from its analysis is possible to obtain the arrangement of all the atoms in our sample. Also by the geometry of the SAED pattern the crystal structure and the orientation of the sample, with respect to the electron beam, can be deduced.

Figure 3.4.1 shows SAED patterns of micromechanically cleaved single and bilayer graphene. The hexagonal geometry of the diffraction pattern confirms the crystal structure of graphene and its orientation with zone axis [001]. By indexing the diffraction spots and analysing the reciprocal distance – r – in the SAED pattern the interplanar distances and the unit cell length – a – are obtained for this zone axis by:

$$r = \frac{1}{d_{hkl}} = \frac{2}{\sqrt{3}} \frac{1}{a} \left(h^2 + hk + k^2\right)^{\frac{1}{2}} \tag{3.2}$$

where hkl are the Miller indices of every diffraction spot.

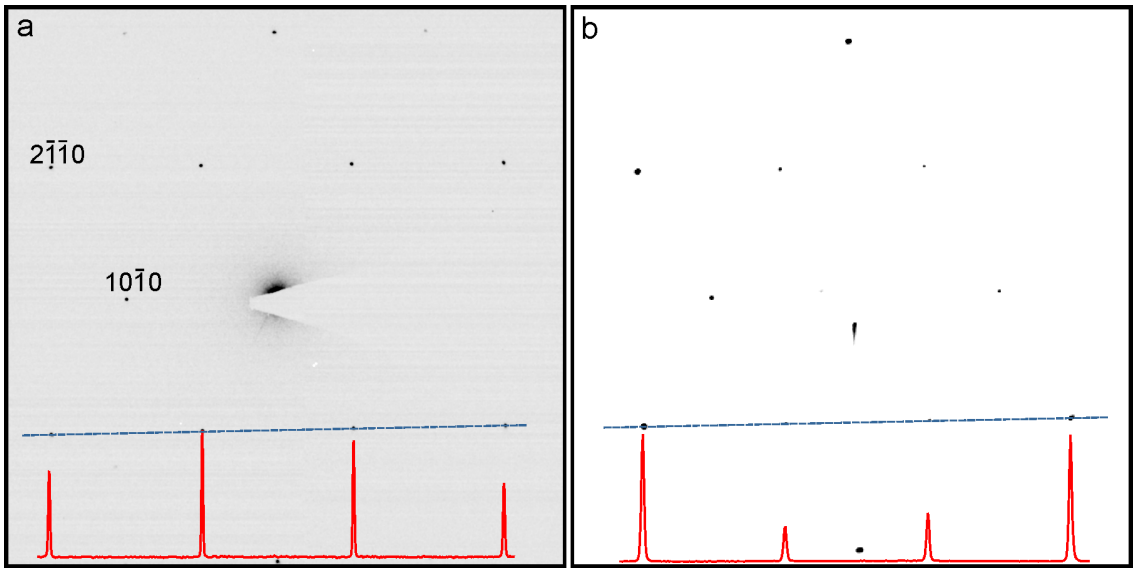

Figure 3.4.1. (a) SAED pattern of single-layer graphene and (b) SAED pattern of double-layer graphene. Blue dotted lines in both images indicate where the line profile has been taken to obtain the intensities of the diffraction spots (shown in red).

The first diffraction spots are at r_1 =4.69 nm^{-1}, and the second spots at r_2=8.13 nm^{-1}. The first spots, in this zone axis, correspond to the <100> reflections and the second to the <110> reflections. With these values, according to equation 3.2, the unit cell length of graphene is a= 2.46 Å.

Information about the number of layers of graphene can be also obtained by SAED pattern analysis. The unit cell of graphene is made of the superposition of 2 trigonal cells rotated by $\pi/3$, thus, for single layer graphene, the intensity of the <100> reflections will be higher than the <110> reflections,[27] just as shown in the line profile in Figure 3.4.1 (a). For bilayer graphene, the intensities of the second reflections are almost double by the stacking arrangement of graphene, line profile in

Figure 3.4.1 (b). Using this approach is possible to conclude, with certainty, if the sample is either single- or bi-layer graphene.

Additionally, by the information obtained in an SAED pattern the crystallinity of graphene can be also be assessed. Figure 3.4.2 (a) shows a SAED pattern of commercial CVD-graphene where two sets of diffraction <100> spots appear in the image indicating the existence of two graphene grains with different orientation. The analysis of angles between the two <100> diffraction spots (marked in blue and red in Figure 3.4.2 (a)) tells the orientation mismatch between crystal orientations, i.e. 9.1°. If a graphene sample is polycrystalline then a ring should appear in the SAED pattern, just as seen in Figure 3.4.2 (b).

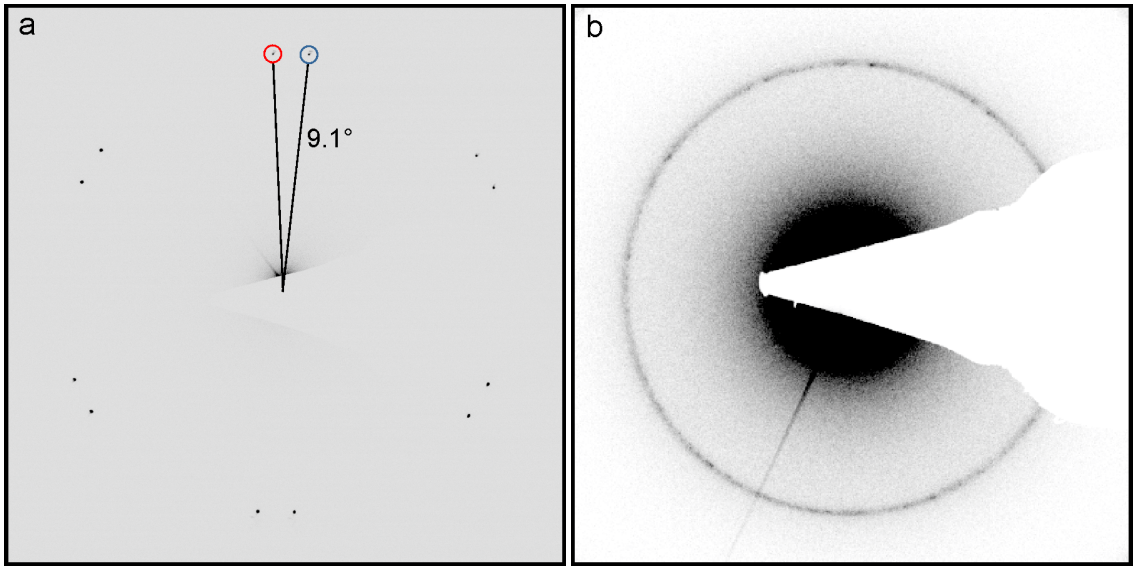

Figure 3.4.2. (a) SAED pattern of two graphene grains at different crystallographic orientations. The angle between graphene grains is 9.1°. (b) SAED of a polycrystalline area of a liquid phase CVD-graphene sample.

Characterisation of graphene by dark field imaging

In dark field (DF) imaging the central beam of an ED pattern is blocked in the back focal plane by an objective aperture. Thus only the scattered beams through the objective aperture contribute to the DF image formation.

On samples that contained many reflections, as is the case of two graphene crystals misoriented, by choosing one of the diffraction spots with the objective aperture then the resulting DF image will contain only the signal from the sample with that specific crystal orientation. As an example, DF imaging was performed in the same

sample area from where Figure 3.4.2 (a) was obtained. The objective aperture was place at one of the <100> reflections thus selecting one graphene crystal orientation (red circle in Figure 3.4.3 (a)). Then a DF image was acquired (Figure 3.4.3 (b)). This DF image shows the two misoriented graphene grains and the boundary between them (here delineated with red line). With DF imaging technique is, thus, possible to characterise the grain size and orientation of grains in a polycrystalline graphene sample.[28]

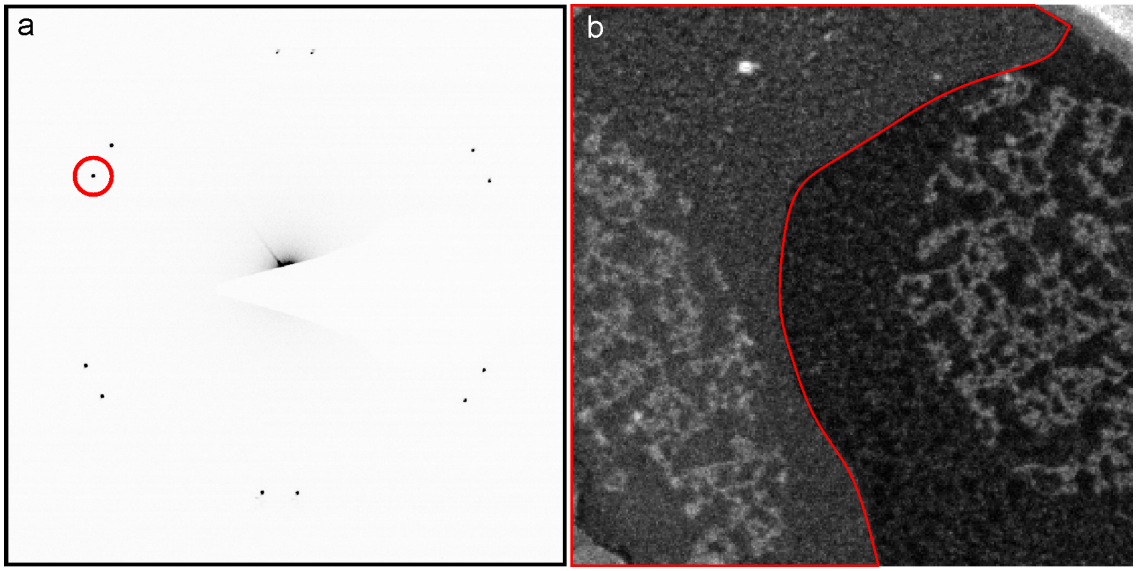

Figure 3.4.3. (a) SAED pattern of commercial CVD graphene (retaken from Figure 3.4.2). Red circle circumscribes the position of the objective aperture for DF imaging. (b) DF image of (a) where the area enclosed by the red line is the graphene crystal with the orientation selected by the objective aperture. Bright features are contamination on graphene.

HRTEM on graphene

Due to the resolution obtained (see Section 3.3) by the use of an aberration corrector the atomic structure of graphene has also been investigated by HRTEM. Working in HRTEM at these imaging conditions, a HRTEM image with positive contrast is obtained, for graphene the C atoms appear as black.

Figure 3.4.4 shows an averaged HRTEM image of graphene where the hexagonal arrangement of the C atoms in graphene is clearly seen. The C-C bond distances and unit cell parameters are obtained by a line profile analysis in this HRTEM image. The results of the line profiles are shown in the bottom images of Figure 3.4.4. The line profile across C-C bonds (b) shows a distance between atoms of 1.42 Å and the line profile across hexagons (c) results in a measured unit cell length of 2.46 Å.

Results which are in perfect agreement with the known structure of graphene and with our SAED pattern analysis.

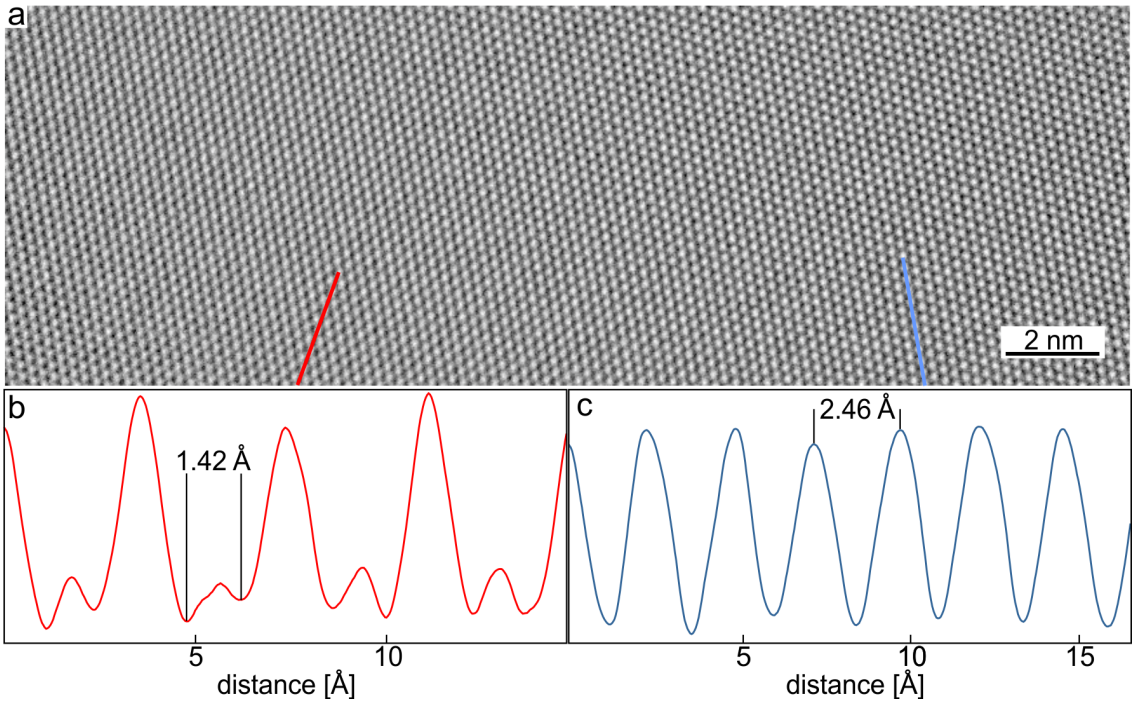

Figure 3.4.4. (a) Image of graphene (summation over 10 frames) where the hexagonal structure is visible. (b) The plot of the line profile across C-C bonds (red line). Distance between C atoms is 1.42 Å. (c) Line profile (blue line) across unit cells. The measured unit cell length is 2.46 Å.

Due to the direct interpretation of a HRTEM image (positions of the atoms) not only does the hexagonal structure of graphene is unveiled, its intrinsic defects and atom dynamics can be described. The stacking configuration and orientation arrangements when the sample is multilayer graphene is also possible to obtained by HRTEM.

A grain boundary in graphene is, mostly, constituted by heptagons and pentagons[28] or by defective sites. Thus, carbon atoms at the grain boundaries are more reactive and as consequence contamination adsorbs on these sites. Figure 3.4.5 (a) shows a grain boundary which is decorate by contamination. Within the same figure but in image (b) a HRTEM image of the area delimited by the red square in (a) is shown, here the defective sites along the gain boundary are pointed out by a red arrow. Apart from the defects and deviations from the hexagonal structure at a grain boundary, intrinsic defects are found in the middle of a graphene crystal, as shown in Figure 3.4.5 (c). These defects occur, mainly, by the surface-catalyse process mediating the growth of graphene on copper. Although defects can be created in

pristine graphene under high electron dose[29] (1 x 10^8 e^-/nm^2), the imaged defects are intrinsic due to our experimental beam settings resulting in a dose of $\sim$ 1 x 10^6 e^-/nm^2 per single exposure.

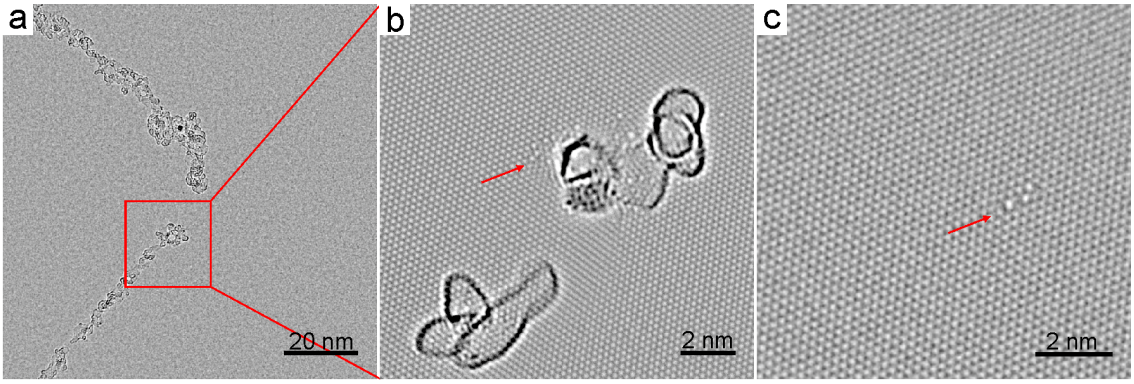

Figure 3.4.5. (a) Grain boundary decorated with contamination. (b) Defective sites along the grain boundary. (c) intrinsic defects in commercial CVD-graphene.

As shown before, by SAED (Figure 3.4.2 (b)) the liquid phase CVD-graphene is polycrystalline, but now with the potential of HRTEM imaging, is also possible to give a detail characterisation of the specimen at the nanometer scale. Studies on CVD-graphene using liquid phase precursor reported the growth of bilayer graphene either in AB or random (turbostratic) stacking configurations.[30]

Liquid phase CDV-graphene grown on Cu foil[v] (25μm) at 980°C and atmospheric pressure, and ethanol as carbon source has been studied on the atomic level describing the adlayer's grain sizes, stacking configurations and their orientation relative to the underlaying graphene layer. Also, with these investigations was possible to assessed the number of adlayers in the sample.[31]

In order to quantify the number of layers in graphene by HRTEM, a hole in the sample has to be produced. Although sputtering of atoms is minimal with 80 keV electrons, it is possible to create a hole due to catalytic reactions between adsorbates and the carbon atoms of graphene. The graphene is chemically etched under the electron beam.[32] The holes, once created, grow under the e-beam by atomic displacement because a carbon atom at an edge of graphene has lower threshold energy for displacement.[33] Once a hole has been created through the graphene layers the number of layers on graphene can be counted, as it is shown in Figure 3.4.6 (a).

[v] Campos-Delgado J., Botello-Méndez A.R., Algara-Siller G., Hackens B., Pardoen T., Kaiser U., Dresselhaus M.S., Charlier J.-C., Raskin J.-P. Chemical Physics Letters **2013**, 584,142-146.

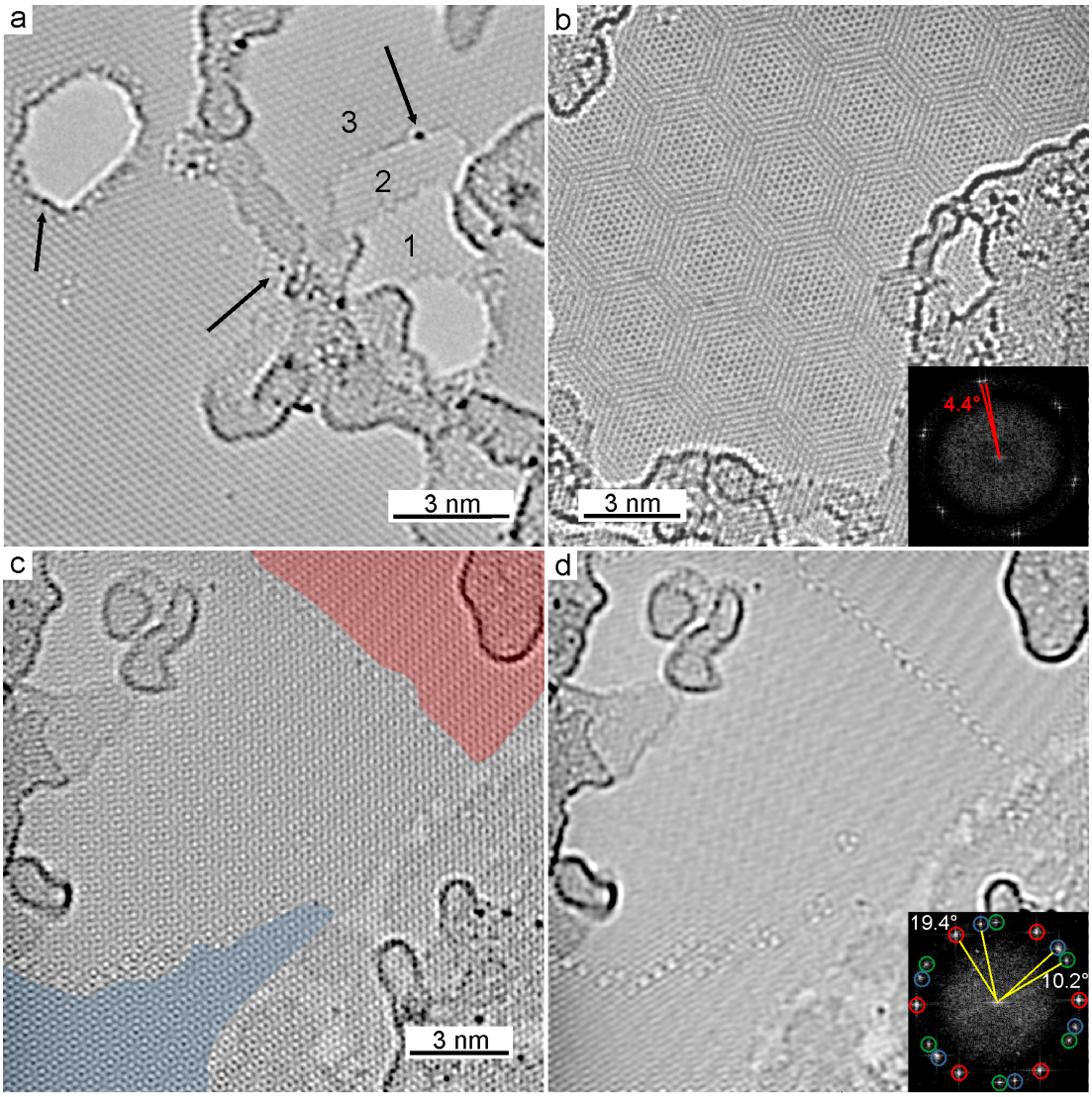

Figure 3.4.6. (a) Quantification of the number of graphene layers in a HRTEM image. The holes seen were produce by chemical etching (black arrows). (b) An area of the sample with twisted adlayer graphene seen clearly by its Moiré pattern. The twist angle between layers is 4.4 ° as measured from the FFT (inset). (c) Grains of adlayers with different orientations (coloured). One grain has not been highlighted to allow a better view of the Moiré pattern. (d) The Fourier-filtered image of (b). The grain boundaries are marked with black lines. The inset (FFT) shows the quantification of the twist angles.

In this image, the adsorbates which chemically etched graphene are marked by black arrows and the number of layers are counted to be 3 (each layer has been marked with its corresponding number). Additionally, it is determined that the stacking of graphene layers in this area of the sample is not turbostratic by the absence of a Morié pattern. Nevertheless, this stacking configuration is not predominant, as shown in Figure 3.4.6 (b and c), where twisted adlayers of graphene – a graphene adlayer with an angular rotation in respect to the underlying layer – are observed

due to the Moiré pattern. The rotation of the twisted adlayer is quantified by measuring the angle between spots in the FFT, see the inset in Figure 3.4.6 (b). Where two or more adlayers meet, a grain boundary is formed. The grain boundaries between graphene grains from liquid phase grown graphene (polycrystalline) are better seen if a Fourier filter is applied to the HRTEM image (Figure 3.4.6 (c)). The quantification of the twist angles between grains is shown in the inset of Figure 3.4.6 (c).

In summary, the fabrication of CVD-graphene using alcohols as carbon source produces bilayer to few layers graphene with small grains ranging from the nanometer to the micrometer scale but nonetheless as continuous film.

SAED and HRTEM to characterise graphene

> Campos-Delgado J., Algara-Siller G., Santos C.N., Kaiser U., Raskin J.-P. Twisted bi-layer graphene: Microscopic rainbows. Small **2013**, 9, 3247-3251.[34]

A combination of SAED and HRTEM techniques has been used to fully characterise a CVD-graphene sample. The graphene sample was produced by low pressure CVD with methane as carbon source.[34] In contrast to the commercial CVD-graphene this sample was first transferred to (100 nm) SiO_2/Si and analysed by optical microscopy. Bilayer and multilayer graphene deposited in SiO_2, when observed in an optical microscope, should exhibit the same colouration of single-layer graphene but with higher contrast.[21] After optical characterisation (Figure 3.4.7) this sample showed to have single-layer graphene (black arrow) and some patches of bilayer graphene (dotted arrow). But some distinctive areas have a colouration (inset), e.g. pink, yellow, green and blue (coloured circles Figure 3.4.7 inset). Because these coloured patches do not follow the optical properties of graphene, thus SAED and HRTEM imaging were used to characterised and demonstrate the nature of the coloured patches.

The SAED pattern of the pink area shows an interlayer orientation of 12.8° (Figure 3.4.8 (a)). Twisted bilayer graphene produces a Moiré pattern in the HRTEM image and from its FFT the angle of rotation can also be corroborated (Figure 3.4.8 (b) and (c), respectively). The same characterisation and analysis was applied to the yellow area, resulting in a twisted angle between graphene layers of 13.4°.

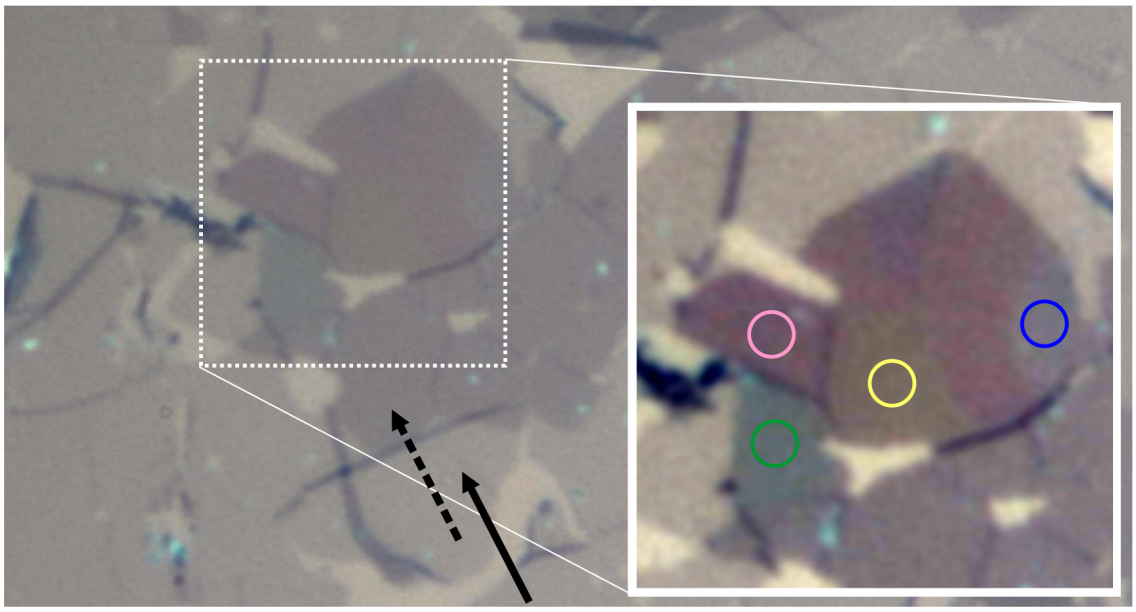

Figure 3.4.7. Optical image of low pressure CVD-graphene with methane transferred to SiO_2. The black arrow shows single layer graphene and the dotted arrow bilayer graphene. The inset shows a magnified imaged of coloured areas. Each area is colour coded with the circles. The brightness and contrast has been adjusted in the inset image.

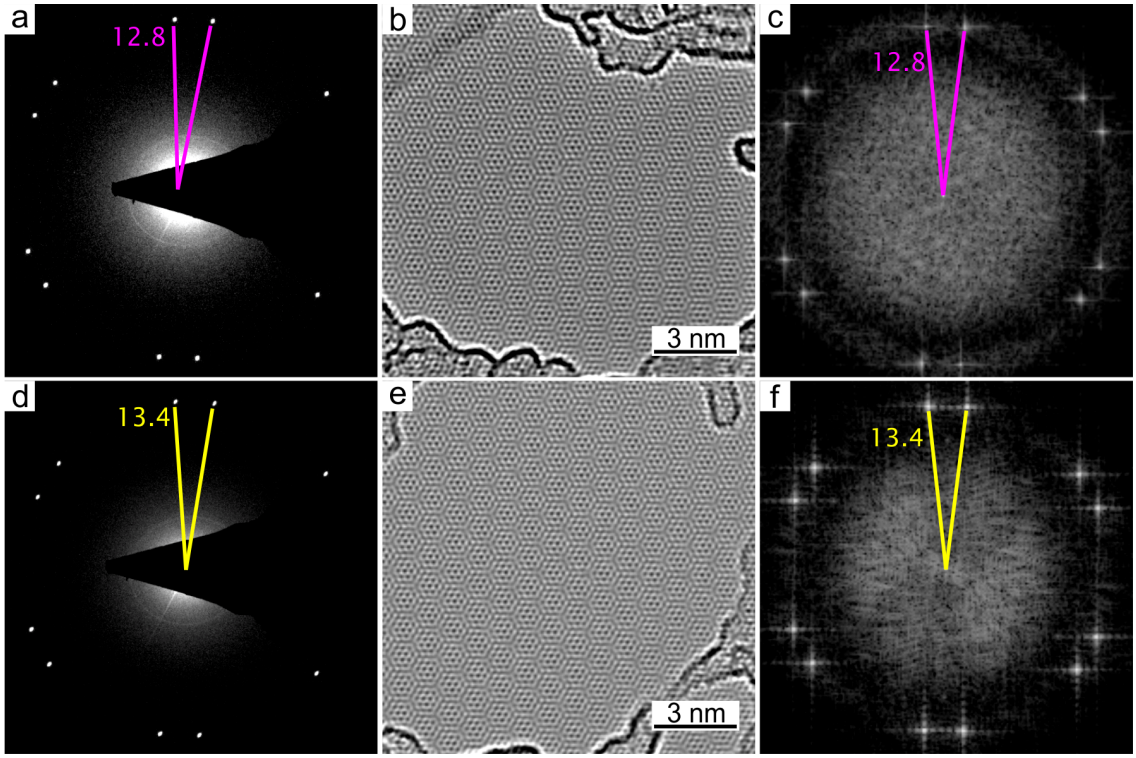

Figure 3.4.8. SAED, HRTEM images and FFT of coloured areas (pink (a–c) and yellow (d–f)). Twist angle marked in the corresponding images.

Relating the rotation angles obtained by TEM and the different colouration observed by optical microscopy, it is possible to conclude that rotation angles in bilayer graphene have an influence in the optical properties of bilayer graphene. Thus, if the optical properties of twisted bilayer graphene change, then the electronic properties of bilayer graphene also change. This experiment corroborates the theoretical calculations which predict that on twisted bilayer graphene the band velocity oscillates with twist angle, and at some angles it vanishes at the Dirac points rising a large DOS.[35]

In contrast to the liquid phase CVD-graphene sample, this sample, low pressure CVD-graphene, has large and continuous areas of single layer graphene with grain sizes (>2 μm) which are similar to the grains in commercial CVD-graphene and to those samples of MC-graphene.

3.5 Comparison of graphene samples

As was shown in the previous sections, TEM techniques allow the detailed characterisation of graphene. The quality of the presented graphene samples (e.g. number of layers and crystallinity) is important on the thesis, thus a comparison between the graphene samples is here presented. Graphene fabricated by micromechanical cleavage is, in fact, single crystalline and it does not exhibit intrinsic defects. Low pressure CVD-graphene with methane as carbon source showed to be mostly constituted by single-layer, however, made of many graphene grains with sizes on the micrometer range. Because those grains arrange in all possible orientations grain boundaries can be found. Also, these samples, due to their fabrication process, contain intrinsic defects. The graphene grown by CVD with a liquid phase precursor is composed of many layers (2-5 layers) and the observed graphene grains sizes are in the nanometer range.

In the following table the results from the TEM characterisation of different graphene samples for each of the different fabrication methods are summarised. From this table it can be concluded that MC-graphene and CVD-graphene grown on Cu from gas phase are the best graphene samples to use as a substrate for TEM for the characterisation of nano-objects, mostly because they are single-layer and have high crystal quality. Thus, those types of graphene samples were used to investigate nanometer size objects by TEM.

Fabrication method	**Num. of layers**	**Sample size**	**Intrinsic defects**	**Grain size**	**Stacking**
MC-graphene	1	5-20 μm	—	5-20 μm	—
Commercial CVD-graphene	1-2	cm	yes	>2 μm	Bernal
Liquid phase CVD-graphene	2-3	cm	yes	nm-μm	Turbostratic
Low pressure CVD-graphene	1-2	cm	yes	>2 μm	Turbostratic

Table 3.5.1. Comparison of the graphene samples, used in this thesis, produced by different fabrication methods.

§ 4 Nano-objects on graphene by HRTEM

> A **nano-object** is that object which has "one or more external dimensions in the nanoscale."
> Ramsden Jeremy. Nanotechnology: an introduction. William Andre/Elsevier. 2011. **ISBN: 978-0-08-096447-8.**

> **Nanomaterial:** "a natural, incidental or manufactured material containing particles, in an unbound state or as an aggregate or as an agglomerate and where, for 50 % or more of the particles in the number size distribution, one or more external dimensions is in the size range 1 nm-100 nm. [...]"
> Communication from the Commission to the European Parliament, The Council and the European Economic and Social Committee. **Brussels, 03.10.2012. COM(2012) 572.**

According to this definition, nano-objects or nanomaterials can be encompassed by a broad range of disciplines in science. But one important characteristic of nano-objects is that their properties and functionalities are different from the micron size and bulk materials, and this difference rises by their size and structure, hence:

> "... if we understand the structure of nano-objects then we can understand their chemical and physical properties, and, therefore is possible control the transformations of matter."

Nano-objects are *per se* or as the building blocks for nanomaterials of great scientific and technological interest. Nanomaterials such as hydrid organic-inorganic systems can be used in many applications in nanotechnology, e.g. biolabeling, biosensing or drug delivery. This chapter contains TEM characterisation of hydrid organic-inorganic systems. Also, in this chapter, another nano-object, i.e., desoxyribonucleic acid (DNA) has been studied by TEM.

4.1 Hydrid nano-objects

In this section is discussed the characterisation of hybrid nano-objects deposited on a graphene substrate by HRTEM .

> " Hybrid nano-objects [...] are constructed by using organic components to coordinate the nucleation, growth, organisation and transformation of inorganic nanophases to produce discrete integrated objects of higher-order structures under equilibrium and non-equilibrium conditions." Stephen Mann. Self-assembly and transformation of hybrid nano-objects and nanostructures under equilibrium and non-equilibrium conditions. Nature Materials **2009**, 8, 781-792 .[36]

The hybrid nano-objects here studied have been developed: for bioimaging and nanotherapeutics; as label free DNA detectors ; and as single protein nanosensors.

Au nanoclusters coated with albumin-derived copolymer

Au nanoclusters or nanoparticles are one of the most common examples of nano-objects because of their distinctive size dependent properties.[37] For example, if the size of a Au nano-object is about the size of the electron mean free path (≈50 nm), i.e. nanoparticle (NP), then its optical properties change compared to the optical properties of bulk. If the Au nano-object is $\sim$ 0.5 nm, i.e. nanocluster (NC), then the whole chemical and physical properties change.[38] For example, Au NPs emit light in the visible spectrum, but Au NCs emit light in the near infrared. The study of Au NCs is of great interest because Au NCs are thought to be the link between a single Au atom and a Au NP. It is worth noticing that in order to achieve Au NCs they should be stabilized, e.g. by protein coating.[39]

It has been reported that a graphene substrate has low noise contribution in a TEM image.[11] As result, it is expected that the contrast of a nano-object will increase when it is deposited on graphene. To corroborate this statement, Au NCs coated with albumin-derived copolymer were produced using hybrid peptide-copolymer functionalised with thiotic acid (dcBSA-147-PEO$(5000)_{28}$-$(TA)_{26}$)[i, 40] and deposited by drop casting on two substrates, standard amorphous carbon films and on graphene (Figure 4.1.1 (a and b), respectively).

[i] Samples produced by Goutam Pramanik. Institute for organic chemistry III, Ulm University.

The contrast obtained from a Au NC (∼2.5 nm ⌀) on amorphous carbon is 10% and the contrast from a similar size Au NC on graphene is 15%. Furthermore, the organic molecules surrounding the Au NCs can not be observed when the sample is deposited on amorphous carbon, whereas in graphene are easy to discern (dark lines in the area left from the red line).

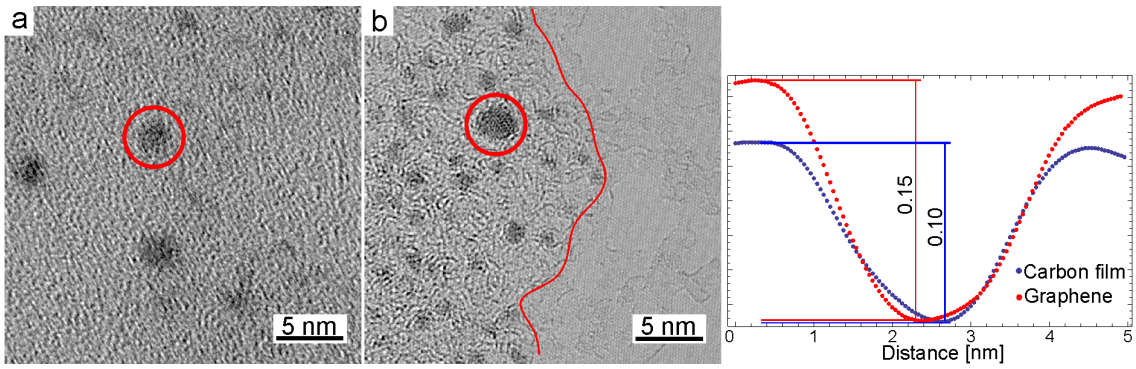

Figure 4.1.1. Copolymer coated Au NCs deposited on amorphous carbon (a) and graphene (b). On the graph, the line profiles across the ∼ 2.5 nm particles (red circles) showing a contrast difference of 30%. The copolymer coating the Au NCs is seen as dark lines in the left area, delimited by red line in image (b).

The size distribution of Au NCs was obtained by particle analysis of low magnification TEM images[ii] (Figure 4.1.2). The size distribution analysis shows that Au NCs can be found in two size ranges or modes, 0.7±0.1 nm and 0.9±0.1 nm. The standard deviation (0.1 nm) is attributed to the Gaussian filter and threshold adjustment applied to the raw image for the particle size analysis. The predominance of clusters with diameter below 1.0 nm (66%) is attributed to the ratio between thiotic acid and Au^{3+} (1:1) and, also, to the type of copolymer used for stabilisation. Because ∼99% of the Au NCs have diameters below 2 nm it is expected that the sample will yield narrow fluorescence emission.[iii]

Another important characterisation for Au NCs coated with albumin-derived copolymer is the structure and conformation of the copolymer, peptides and thiols. Here, several problems rise for this characterisation which are: (1) from deposition, the copolymer, a long and flexible molecule, piles upon drying thus the original three dimensional conformation is lost and (2) as hydrocarbon molecules are radiation

[ii] ImageJ software, Analyze particles plug-in.

[iii] Full description on Au NCs fabrication and characterisation can be found in: Goutham Pramanik. Near infrared emitting nanoemitters for bioimaging applications, Ph.D. Thesis, Ulm University, 2013[40]

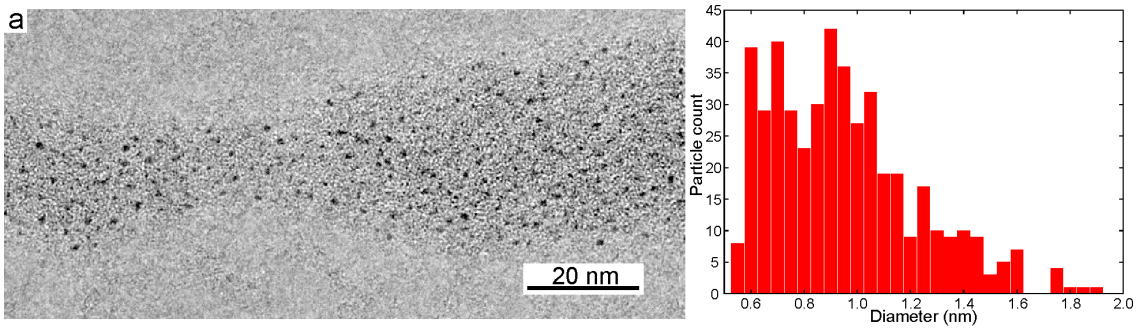

Figure 4.1.2. Bright field image of copolymer coated Au NCs deposited on graphene and histogram of the size distribution.

sensitive materials, C-H and C-C bonds break[1] with electron doses between 400-1200 e^-/nm^2, thus the pristine state of the organic molecules is not conserved during HRTEM imaging ($\approx$ 1x $10^6 e^-/nm^2$). Nevertheless, due to the low noise contribution from the graphene substrate is possible to discern the existence of organic molecules coating the Au NCs (Figure 4.1.3).

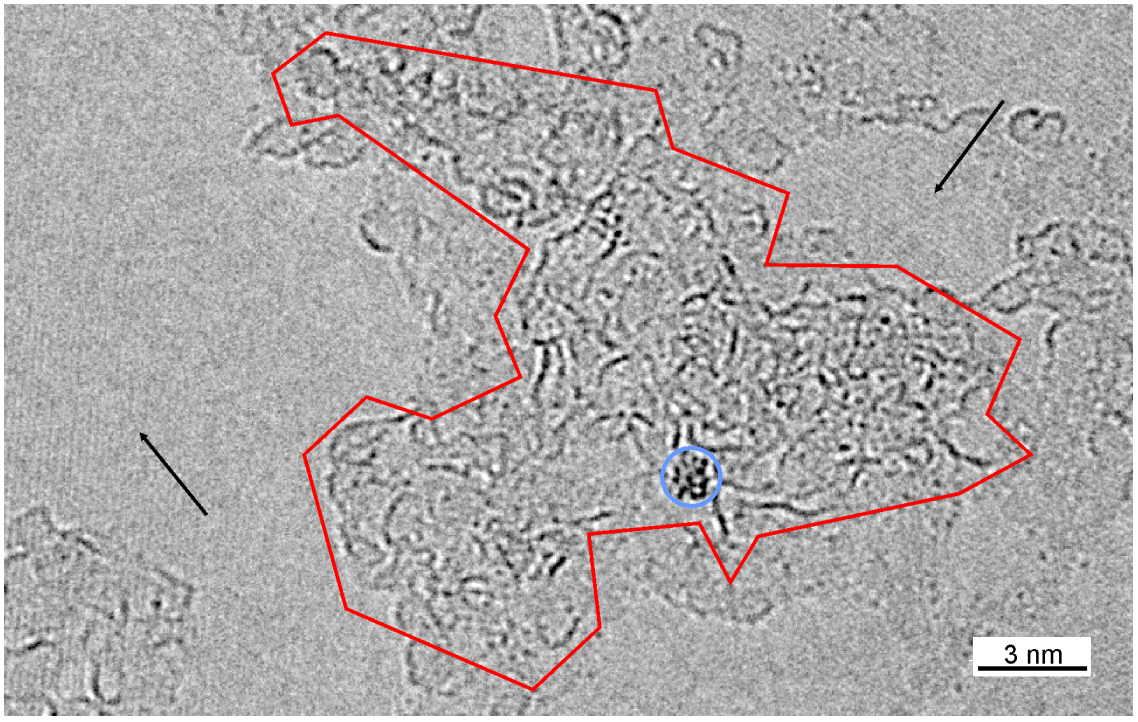

Figure 4.1.3. HRTEM image of Au NC coated with copolymer. The red line delineates the extension of the copolymer upon drying and the blue circle the Au NC (⌀=1 nm). The lattice of the graphene substrate is also observed (marked with black arrows).

QDs coated with an albumin-derived copolymer.

> Wu Y., Eisele K., Doroshenko M., Algara-Siller G., Kaiser U., Koynov K., Weil T. A quantum dot photoswitch for DNA detection, gene transfection, and live-cell imaging. Small **2012**, 8, 3465—3475.[41]

Semiconductor quantum dots (QDs) have remarkable size dependent properties, for example strong photoluminescense with specific emission.[42] This photoluminescence can be used for biolabeling delivery vectors or as it has been reported as label-free DNA detection systems due to the emission quenching by the electron transfer between QDs and DNA.[43]

CdSe/CdZnS QDs coated with cationic polypeptide copolymer (cBSA) (cBSA-QDs)[41] were investigated by TEM. By drop coating, the cBSA-QDS were dispersed on an annealed (250° C for 5 minutes) and plasma (H_2:O_2) treated MC-graphene. To enable the characterisation of the QDs, the concentration of the dispersion was 1 ng/μL. This concentration was used to avoid the superposition of QDs in top of each other, as seen in Figure 4.1.4 (a). An example of the QDs dispersion is seen in Figure 4.1.4 (b). From the particle analysis of many images it was possible to determined the size distribution of the QDs, yielding an average diameter of 8 $\pm$2 nm.

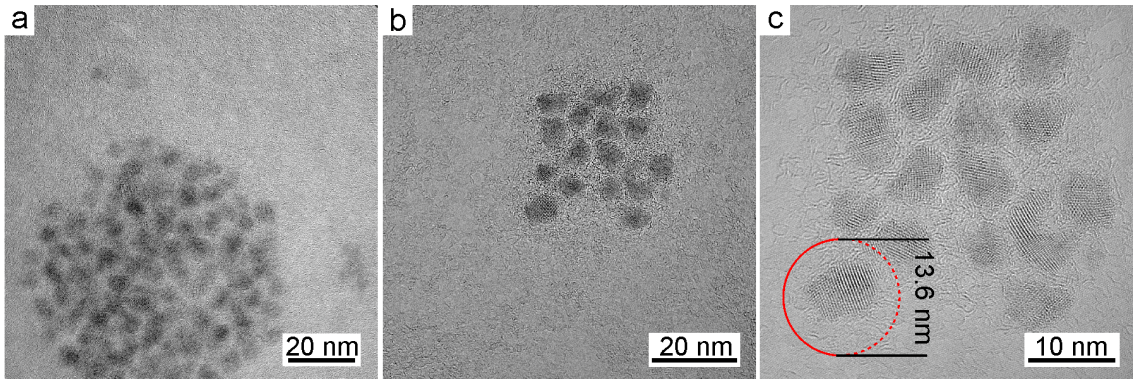

Figure 4.1.4. HRTEM images of clusters of QDs. (a) QDs from a high concentrated solution. (b) A cluster of QDs with a concentration of $\approx$ 1 ng/μL. (c) A high magnification HRTEM of QDs coated by cBSA copolymer where the lattice fringes of QDs are visible.

Also, the morphology of cBSA-QDs was investigated by HRTEM (Figure 4.1.4 c). In this image, the lattice fringes originating from the CdSe-CdZnS cores are clearly seen. The cBSA can be inferred as the shell-like structures surrounding the QDs (enclose by red circle in Figure 4.1.4 (c)). The approximate radial extension of the

cBSA out from the QDs has been calculated to range between 5-15 nm. Thus, the total diameter of a copolymer coated QD can be 13-25 nm. Within this range, the total diameter of any coated QD observed by TEM is smaller than the theoretical and experimental hydrodynamic size of cBSA-QDs ($\approx$ 39 nm).[41] The large difference is due to the fact that cBSA-QDs deposited on graphene are dry.

Nanodiamond with Ferritin on Graphene

> Ermakova A., Pramanik G., Cai J.-M., Algara-Siller G., Kaiser U., Weil T., Tzeng Y.-K., Chang H. C., McGuinness L. P., Plenio M. B., Naydenov B., Jelezko F. Detection of a few metallo-protein molecules using color centers in nanodiamonds. Nano Letters **2013**, 13, 3305–3309.[44]

Interest in studying nanodiamonds with nitrogen-vacancy defects centres (NVs) has grown due to their magnetic sensitivity at ambient conditions, their strong fluorescence, and their biocompatibility, thus making nanodiamond with NVs highly applicable for biosensing. The fluorescence of nanodiamons with NVs is dependent on the NV spin state.[45] Thus if the spin state in the NVs is changed, e.g. by spin coupling from an atom or molecule, then its fluorescence also changes.

On this principle nanodiamond with NVs coated with protein complexes were produced. By electrostatic attraction ferritin proteins (iron storage molecules) were adsorbed on nanodiamond.[44] The thermal fluctuations of the iron electron spins in ferritin led to coupling with the NV spin, as proved by optically detection of magnetic resonance. This coupling shorten, as proved by Ermakova et al.,[44] the coherence and relaxation time.

HRTEM studies where made on a sample of nanodiamond-ferritin complex to corroborate the adsorbed ferritin molecules. Figure 4.1.5 shows a low magnification and a HRTEM image of ferritin molecules adsorbed on a single nanodiamond with NVs deposited on graphene substrate. The iron based cores (pointed out by arrows) are easily observed by their strong contrast. Their average diameter is 5 nm, this value of the size of the iron cores in ferritin is consistent with literature.[46]

Although the ferritin cores were observed to be adsorbed on the surface of the nanodiamond, their pristine structure, i.e. hydrous ferric oxide, could not be imaged. The total dose that organic compounds can sustain before complete destruction

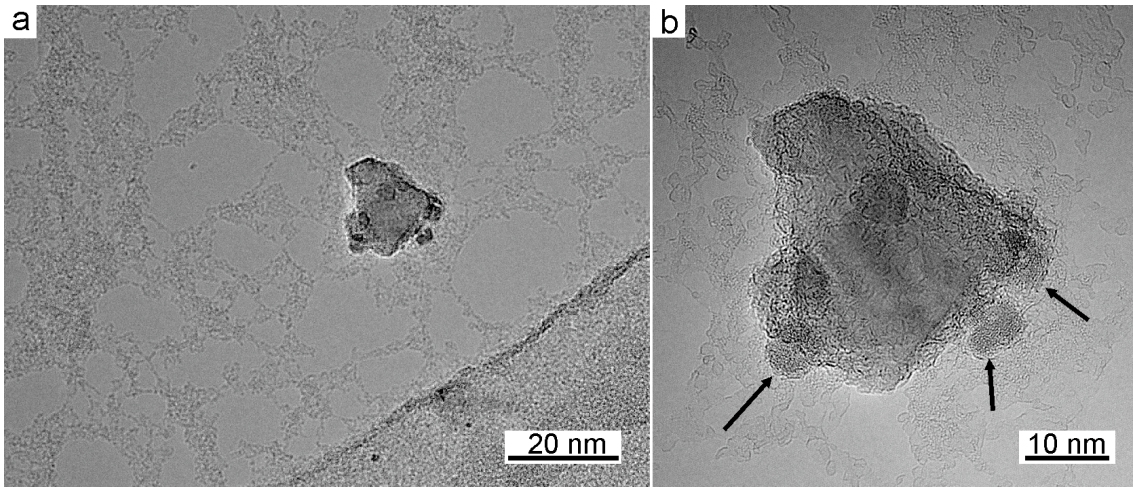

Figure 4.1.5. (a) Low magnification image of a nanodiamond with NVs and the adsorbed ferritn molecules. (b) A HRTEM image of the same nanodiamond where the ferritin molecules are pointed out by arrows. The avergae diameter of the iron core is $\sim$ 5 nm.

is approximately 100–10000 e^-/nm^2.[1] In this study the used electron dose rate for HRTEM imaging was three orders of magnitude higher than the total dose for destruction, therefore the structure of the cores could not be studied.

4.2 DNA/Graphene

This section is dedicated to describe the development of sample preparation and deposition, to approach the imaging of the DNA structure at the atomic scale. Additionally, it gives first results on imaging pristine (unstained) DNA by HRTEM and it discusses the challenges for successfully image DNA.

Double strand DNA consists of nucleobases (adenine, cytosine, guanine and thymine), deoxyribose and phosphates, hence, DNA is an electron beam sensitive molecule.[iv] For example, the total electron dose for complete destruction of nucleobases range from 2.4 x 10^2— 3.6 x 10^4 e^-/nm^2.[1] Due of the nature of the constituent atom species in DNA (e.g. C, O, N, H, and P) low contrast from the molecule is expected.

Because of the importance of the DNA for the understanding of life Kleinschmidt and Zahn[47] developed a method to imaging DNA in TEM. This method consisted in spreading the DNA molecule in a protein based film and deposited the sample on carbon or formvar TEM grids. To increase the contrast of the DNA, for imag-

[iv] Sections 2.2 and 2.3

ing, the sample was either stained with molecules containing heavy atom species (e.g. uranyl acetate) or shadowed by metal films (e.g. by Pt evaporation). But the sample's spreading film and the treatments for contrast enhancement hindered the possibility to resolve the structure of DNA. Nonetheless, through this technique, vast information has been retrieved from the TEM experiments: heteroduplex analysis, DNA replication, transcription complexes or denaturation of DNA.[48] In order to improve the above mentioned constrains, staining or shadowing DNA should be avoided and, to decrease the substrate contribution of noise to the image, an alternative substrate should be use.

As reported by several groups[11,49] and proven in section 4.1, graphene is the ideal substrate to obtain high contrast from the atoms in DNA due to its minimal noise contribution to the image. Moreover, its robustness against electron irradiation and its high conductivity may aid to reduce some radiation damage effects in DNA.

Image calculations of DNA on amorphous carbon and graphene are shown in Figure 4.2.1 (a) and (b), respectively. The signal contribution by each substrate to the resulting image is obvious: the DNA structure is completely obscured by the amorphous carbon substrate, while on graphene is possible to distinguish the basepairs separation. This analysis corroborates that graphene is an ideal substrate to image DNA.

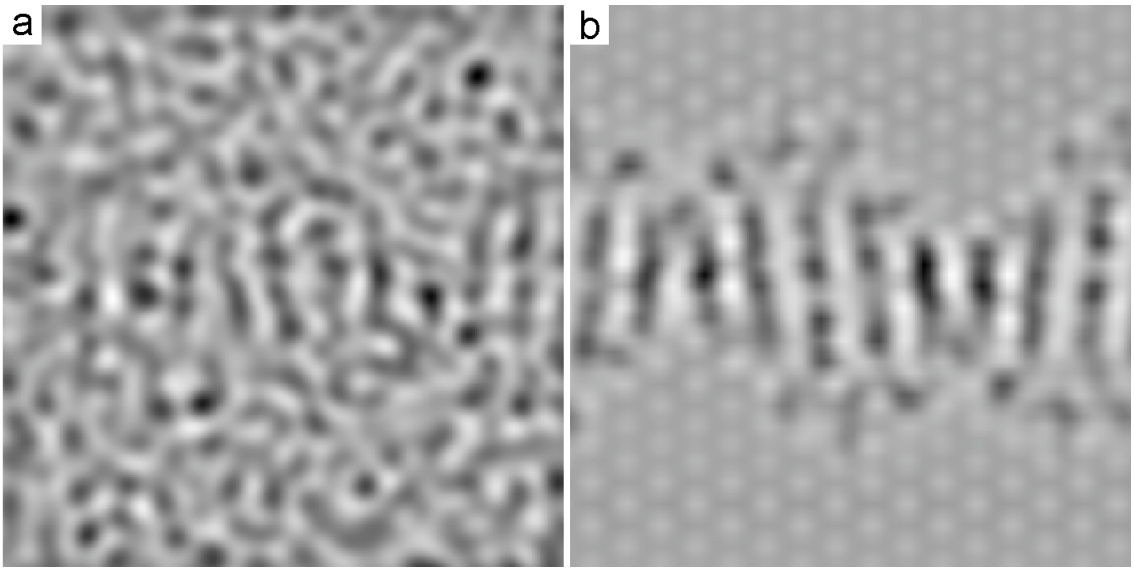

Figure 4.2.1. Image simulations of DNA on different substrates. (a) DNA on (5nm) thick amorphous carbon substrate and (b) on graphene. In (b) the base pairs and the backbone of DNA are clearly seen.

A DNA sample was prepared making a solution of plasmid DNA (pUC19) with concentration of 1 ng/μL. It was deposited by drop coating in an annealed-plasma treated graphene (200°C for 5 minutes and H_2:O_2 plasma for 3 seconds at 30 Watts) and let to dry under atmospheric conditions before inserting it in the TEM. The nominal width of a double helix DNA is 1.8 nm, the distance between base pairs is 3.3 Å and a complete helical twist is reached after 11 turns (3.3 nm).[50] As pUC19 is a circular DNA with 2686 basepairs, its circumference is, then, 886.38 nm. A low magnification image shows a pUC19 molecule as linear (Figure 4.2.2 (a)) with a contour length of $\sim$ 380 nm. This result suggests that the plasmid DNA is interwounded, as depict in the Figure 4.2.2(b). According to literature, interwounding is, normally, due to torsional stress and it is expected for DNA with close ends.[50]

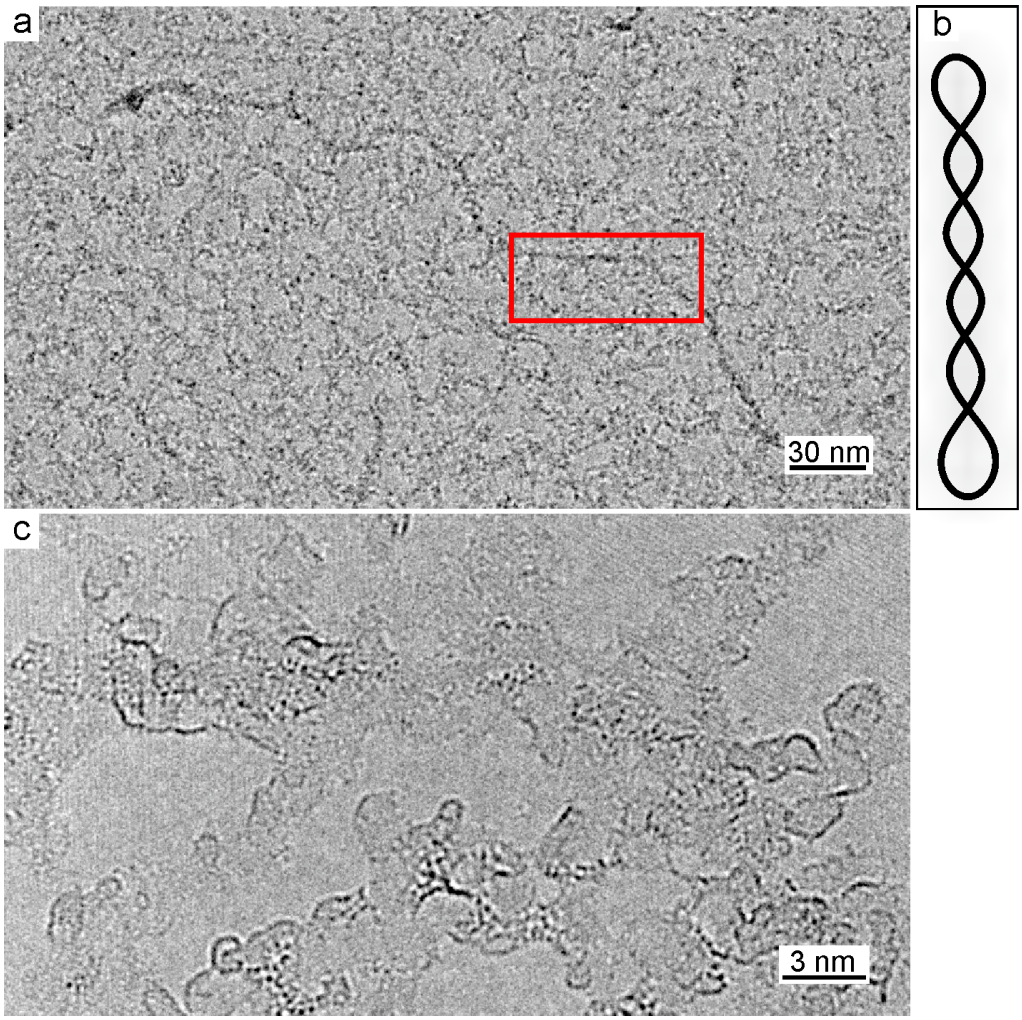

Figure 4.2.2. (a) Low magnification image of pUC19 deposited on graphene. The contour length is $\approx$ 380 nm. Drawing of interwounded DNA (b). (c) HRTEM image of the section delimited by the red rectangle in (a).

Although the DNA in this experiments was not stained or shadowed the observed contrast is due to the vast amount of contamination which accumulates on top of the DNA molecule. Therefore the contamination prevents the measurement of the width of the DNA, thus no information about the interwounding of DNA was retrieved. Moreover this contamination hinders the atomic resolution of the structure as seen in Figure 4.2.2 (b). Additionally, it is possible that in this image the structure of DNA has been already damaged by the high electron dose rate used (1 x $10^6 e^-/nm^2 s$), but, again, due to the contamination this cannot be determined.

With this experiment, although DNA could not be atomically imaged, it has been proven that the used substrate preparation methods make graphene hydrophilic and that the sample concentration and deposition technique allow good DNA dispersion on graphene, all these processes being important steps towards the atomically description of DNA by TEM.

§ 5 2D materials on graphene

Since graphene, the world of 2D materials has been growing because 2D materials have shown interesting and different properties to those of bulk (3D). For example some transition metal dichalcogenides (e.g. MoS_2) have a band gap, thus it can be used in electronics devices. Additionally, dichalcogenides showed to have good catalytic properties.[51] Another example of 2D materials are hexagonal boron nitride (h-BN) or carbon nitride (C_3N_4), graphitic-like materials. They show similitude to graphene in terms of mechanical robustness and thinness except the electrical properties.

The challenge in characterising many of these materials by TEM is their sensitiveness towards electron irradiation.[52–54] An approach to overcome this problem is to image these materials with a protective layer, which in this case is graphene.

5.1 Graphitic carbon nitride on graphene

> Algara-Siller G., Severin N., Chong S.Y., Björkman T., Palgrave R.G., Lavbourn A., Antonietti M., Khimyak Y.Z., Krasheninnikov A.V., Rabe J.P., Kaiser U., Cooper A.I., Thomas A., Bojdys M.J. Triazine-based, graphitic carbon nitride: a two-dimensional semiconductor. Angewandte Chemie **2014**, 53.[55]

Graphitic carbon nitride (g-C_3N_4) was theoretically predicted by Teter and Hemley[56] but its fabrication, since, had not yielded a well-defined material. Recently a new synthesis method was developed[i] to obtain large crystals of g-C_3N_4[55] (Graphical model shown in Figure 5.1.1). For TEM investigations, g-C_3N_4 was cleaved and deposited in SiO_2 and transferred to TEM grids using KOH.

First TEM characterisation of free standing g-C_3N_4 resulted in a rapid damaging of the material. Under a total electron dose of 1.4 x 10^6 e^-/nm^2 the crystallinity of the material was lost. In order to show the damage caused by the e-beam two images from a sequence are presented in Figure 5.1.2. The structure of g-C_3N_4 is

[i] Sample fabrication made at the University of Liverpool by Dr. Michael Bojdys.

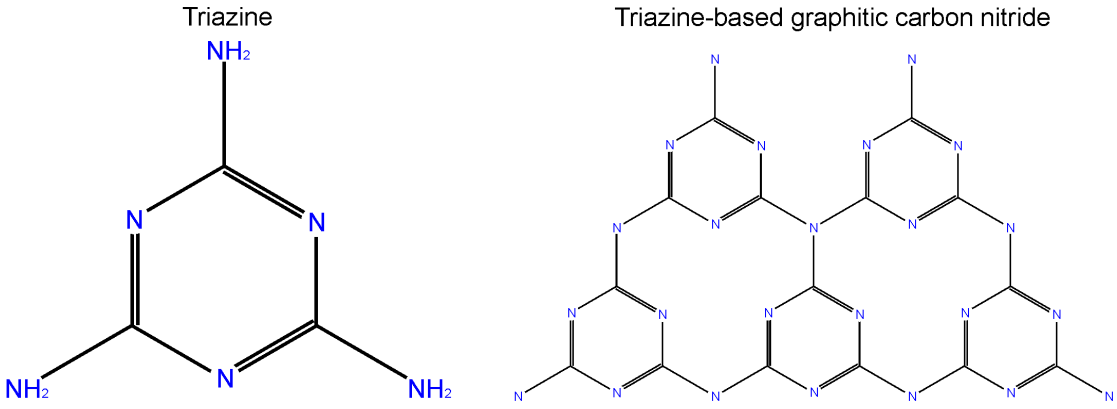

Figure 5.1.1. Chemical model of triazine molecule and triazine-based g-g-C_3N_4.

seen in panel (a) and the damaged structure in (b). The loss of crystallinity in the material is also observed by analysing the FFTs for each of the images (FFT (a) and FFT (b)). Where the FFT of image (a) shows clear hexagonal diffraction spots, these spots are very faint in the FFT of image (b).

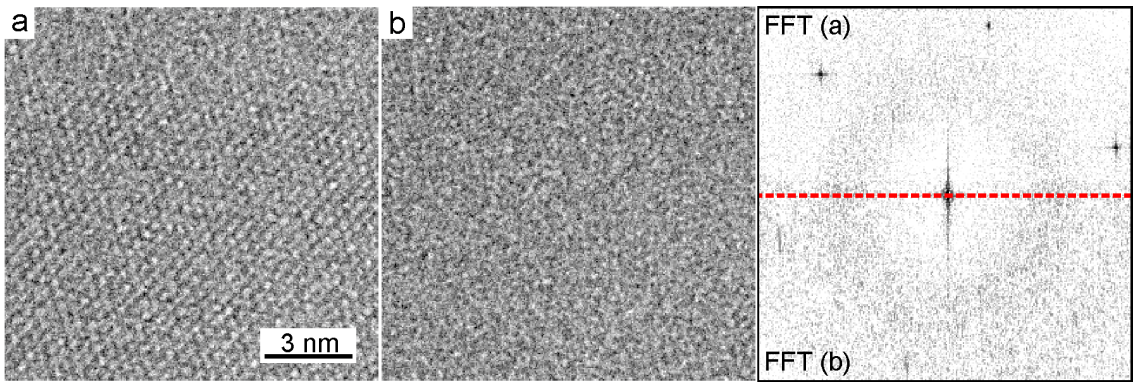

Figure 5.1.2. (a) HRTEM image of g-C_3N_4 where the hexagonal structure is observed. Dose rate 1.4 x 10 $^5e^-/nm^2$ s. (b) The same area of observation but after an accumulated dose of 1.4 x 10^6 e^-/nm^2 . Here the hexagonal structure is nearly lost (except bottom-right hand side corner). The loss of crystallinity is also seen from the comparison of FFT (a) and FFT (b), where the FFT (b) show faded spots.

A heterostructure of graphene/g-C_3N_4/graphene was prepared by transferring g-C_3N_4 to a graphene/grid and, subsequently, a MC-graphene was transferred to the g-C_3N_4/graphene/grid. The schematic representation of the heterostructure fabrication is shown in Figure 5.1.3.

Due to the different size of the g-C_3N_4 and the MC-graphene flakes, and the orientation of these during transfer it was possible to find, in the same sample, parts with graphene/g-C_3N_4/graphene, g-C_3N_4/graphene and free-standing g-C_3N_4 (Figure

Figure 5.1.3. (1) Transfer of graphene (black line) from SiO_2/SiO substratre (purple box) to quantifoil grid (yellow line)– graphene/grid. (2) Transfer of g-C_3N_4 (blue line) to graphene/grid. (3) Another graphene flake is transferred to g-C_3N_4/graphene/grid.

5.1.4 (a–c) respectively). In all these sample configurations the structure of g-C_3N_4 was imaged using an electron dose rate of 8.8 x 10^6 e^-/nm^2s without apparent structural damage, even for free-standing g-C_3N_4 (Figure 5.1.4 (c)). This result is an indication of the protective effects of graphene against radiation damage.

Each heterostructure configuration is assessed by the number of spots appearing in the FFT, for example Figure 5.1.4 (a) shows two sets of graphene spots (red arrows) and one set of g-C_3N_4 (blue arrow) while Figure 5.1.4 (b) show only one set of graphene spots. Figure 5.1.4 (c) shows free-standing g-C_3N_4 which is very thin, at least 3 layers, but no monolayers were found. From these images the unit cell parameters of g-C_3N_4 were obtained, resulting in a hexagonal structure with unit cell length a=b=2.60 ±0.05 Å.

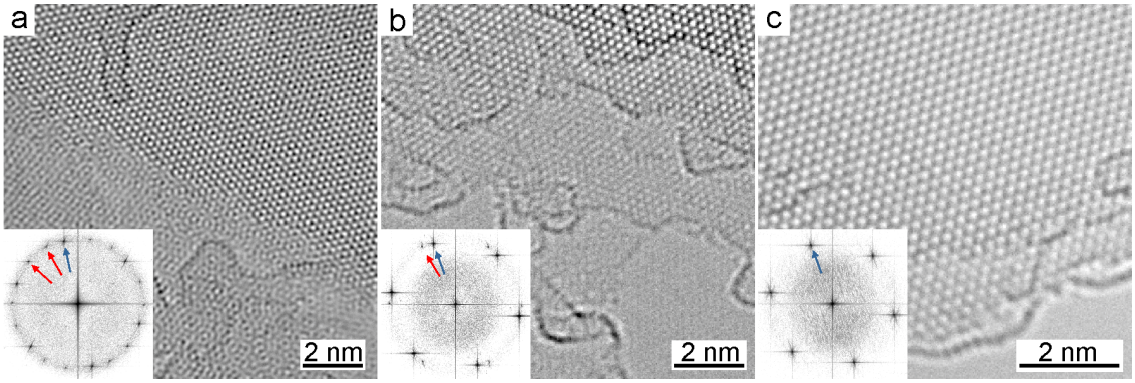

Figure 5.1.4. HRTEM image of (a) graphene/g-C_3N_4/graphene heterostructure, (b) g-C_3N_4/graphene, and (c) free-standing g-C_3N_4. Electron dose rate= 8.8 x 10^6 e^-/nm^2s. The inset in each of the panels shows the FFT for each image. Blue arrows point to a g-C_3N_4 spot and the red to the graphene spots. The unit cell length obtained from the HRTEM images and FFTs is 2.60 Å.

Layered materials like graphene or g-C_3N_4 can be stacked in different configurations, therefore possible stacking configurations for g-C_3N_4 were modelled. Images from these models were calculated and compared to experimental images. Figure 5.1.5 shows sketches of AA, AB, ABC stacking configurations (blue, red-blue and green-red-blue diagrams respectively) and their corresponding image calculation. A reference experimental HRTEM image is also shown in Figure 5.1.5 where the unit cell has been superimposed (yellow). The coloured dots correspond to the triple coordinated nitrogen atoms from the triazine molecule. By comparison of these images, the best fit to the experiments is the ABC stacking configuration. Turbostratic configurations were ruled out due to the lack of Moiré patterns in the images and the absence of rotated Bragg reflections in the FFTs (e.g. Figure 5.1.4 (c)).

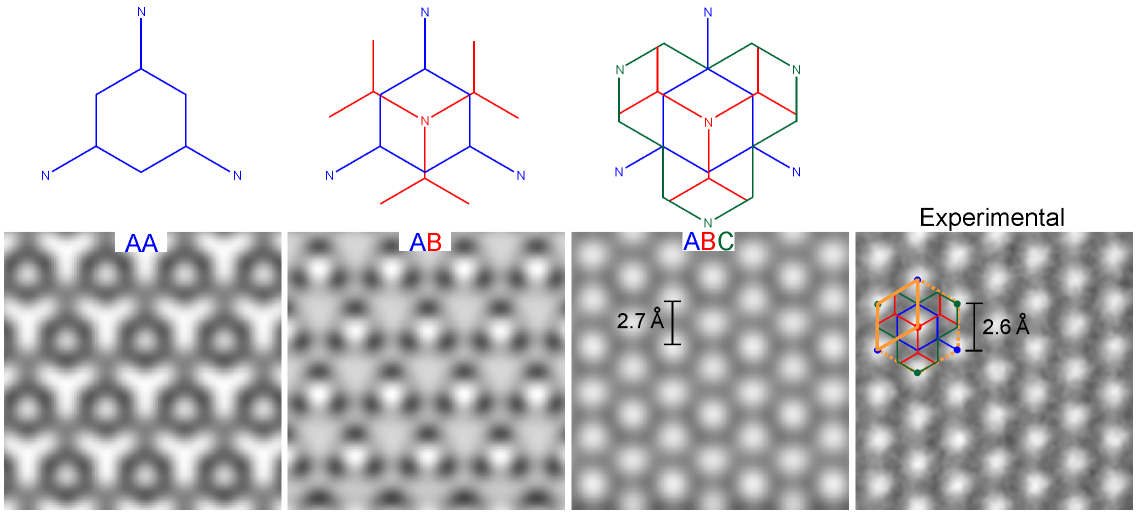

Figure 5.1.5. Sketch of the 3 possible stacking configuration for g-C_3N_4 and their image calculation. In blue AA; in red and blue AB; green red and blue ABC. Experimental image (right), the unit cell has been superimposed (yellow).

To prove the position of atoms, image calculations were performed on models where triple coordinated N atoms were removed from a triazine molecule in a g-C_3N_4 layer and its benzene ring (Figure 5.1.6). Panel (a) shows a perfect structure of g-C_3N_4, panel (b) one of the triple coordinated N has been removed (see missing green dot), and two N atoms for panel (c), and panel (d) shows the calculated image where a complete triazine molecule (3 N atoms and benzene ring) have been removed. Through these image calculations, the atom positions have been retrieved as well as their contribution to image formation.

By the characterisation of the g-C_3N_4 by HRTEM and the comparison to image

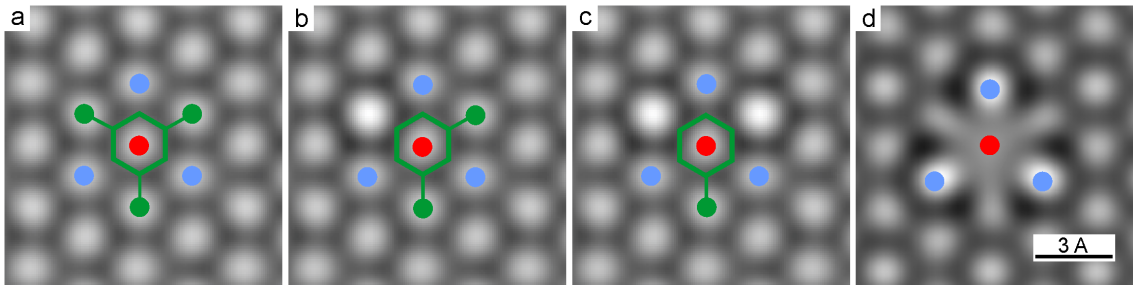

Figure 5.1.6. (a) Image calculation of perfect g-C_3N_4 with the three coordinated N atoms describe as coloured dots. (b) one N atom missing from the top layer, (c) two N atoms missing and (d) the benzene ring from the triazine molecule and the third N atom were removed.

calculations, the structure of g-C_3N_4 (in this stacking configuration) was resolved. With complementary techniques, e.g., SFM, optical spectroscopy and XPS, it was proved that the fabricated sample was indeed g-C_3N_4. This is the first time that g-C_3N_4 has been synthesized with the correct stoichiometry.

5.2 Molybdenum disulfide on graphene

> Algara-Siller G., Kurasch S., Sedighi M., Lehtinen O., Kaiser U. The pristine structure of MoS_2 monolayer protected from electron radiation damage by graphene. Applied Physics Letters **2013**, 103, 203107.[57]

Molybdenum disulfide (MoS_2), a dichalcogenide, is one of the new generation two dimensional materials, and it is interesting due to its band gap (1.8 eV) and feasability to fabricate complex materials.[58] The 3D structure of MoS_2 is hexagonal (space group number= 194, a=b=3.19Å, c=14.879Å, α=β=90°, γ=120°) and its unit cell contains 6 atoms (2 Mo and 4 S). A model of monolayer MoS_2 (half unit cell) is shown in Figure 5.2.1, from low angle (a) and top-down perspective (b). The sulphur atoms are coloured in yellow and the Mo atoms in blue.

MoS_2, as many layered structures, has van der Waals bonding between the layers, hence monolayer MoS_2 can be fabricated by micromechanical cleavage. The characterisation of free-standing pristine monolayer MoS_2 was not possible because MoS_2 rapidly damages under 80 kV electron beam.[54] To protect the monolayer MoS_2 from radiation damage, a heterostructure of graphene/MoS_2/graphene was fabricated following the method described in the previous section.

The sample was first inspected by SAED to identify the number of layers in the

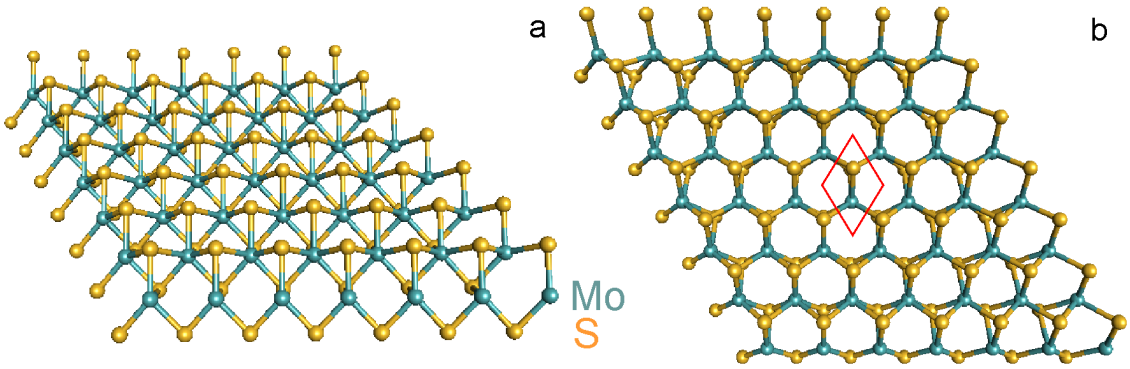

Figure 5.2.1. The MoS_2 structure model seen from low angle (a) and top-down perspective (b). Atoms of S and Mo are represented by yellow and blue spheres, respectively. Monolayer MoS_2, which is the half the unit cell of bulk MoS_2 contains 1 Mo and 2 S atoms (unit cell is drawn in red).

MoS_2. According to Brivio et al.,[59] due to the structure of monolayer MoS_2 (symmetry breaking) the intensity between first order diffraction spots should have a ratio of $\approx$ 1.1 or 0.9. A SAED pattern was recorded and analysed (Figure 5.2.2). The vertices of the red hexagon point to the first diffraction spots of MoS_2. A line profile across these diffraction spots (black dotted line) results in a ratio of 1.1, as expected from a monolayer MoS_2 (Figure 5.2.2 (b)). In addition, the diffraction pattern shows two graphene reflections, blue hexagon and blue dotted hexagon. These graphene diffraction reflections prove the existence of the top and bottom graphene membranes which are rotated relative to each other by 1.8°, hence MoS_2 is encapsulated, effectively, between graphene layers.

Once the existence of monolayer MoS_2 was corroborated, characterisation by HRTEM imaging was performed (Figure 5.2.3). During imaging the highest electron dose rate imposed on the sample was 7.5 x 10 ^{6} e^-/nm^2s, it is worth noticing that MoS_2 encapsulated between graphene withstands a total dose 1 x 10^{10} e^-/nm^2 without significant damage (5% of S atoms removed). The observed damage in monolayer MoS_2 at these doses is, only, the creation of single vacancies (red arrows in Figure 5.2.3 (b)).

Theoretical calculations for e-beam induced damage of MoS_2, described in the report of Komsa et al.,[54] show that the sulphur atoms are more prone to be removed from the lattice than the molybdenum atoms, if knock-on is the most dominant damage process. Image calculations of pristine MoS_2, single vacancy of S, double vacancy of S, and Mo single vacancy in MoS_2 (Figure 5.2.4 (a-d)) have been made

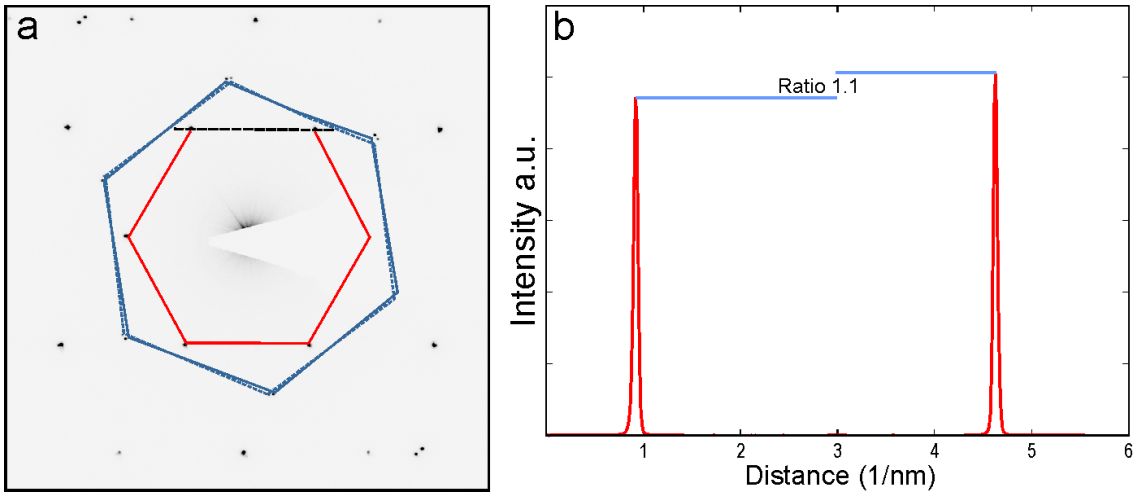

Figure 5.2.2. (a) SAED pattern of graphene/MoS_2/graphene heterojunction. Vertices of red hexagon point towards the first reflections of MoS_2 and the blue hexagon and blue dotted hexagon to the first reflections of the two different graphene layers in the heterojunction. (b) Result of a line profile across two of the MoS_2 first reflections (black dotted line in (a). The ration between reflections intensities is 1.1,thus the image MoS_2 is monolayer.[59]

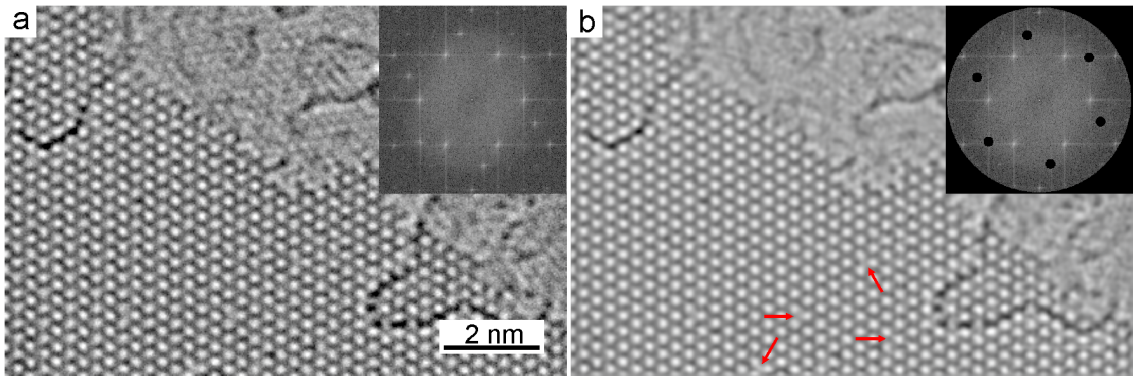

Figure 5.2.3. (a) Raw HRTEM image of graphene/MoS_2/graphene. The inset shows the FFT of the image. The FFT and has the same characteristics as the SAED pattern shown in Figure 5.2.2 (a). (b) Fourier filtered image of (a). The FFT mask used is shown in the inset where the graphene spots and high frequencies have been removed.

to compare them to the experimental image. As expected, the model with a single vacancy of S (Figure 5.2.4 (b)) in MoS_2 gives the closest match to the experimental image. In addition to this qualitative comparison, line profiles across these defects were made (graph of Figure 5.2.4). The similitude in shape and intensity between the line profiles of the experimental image and the single vacancy of S (image calculation) corroborates that the observed defect in MoS_2 is, indeed, a sulphur single vacancy.

Properties of monolayer materials may vary depending on the edge structure. For

example, Bollinger et al. observed that the edges of a monolayer MoS_2 terminated with S are metallic[60] and Botello-Méndez et al.[61] predicted that MoS_2 nanoribbons with edges terminated in zigzag, apart from being metallic, have unusual magnetic properties.

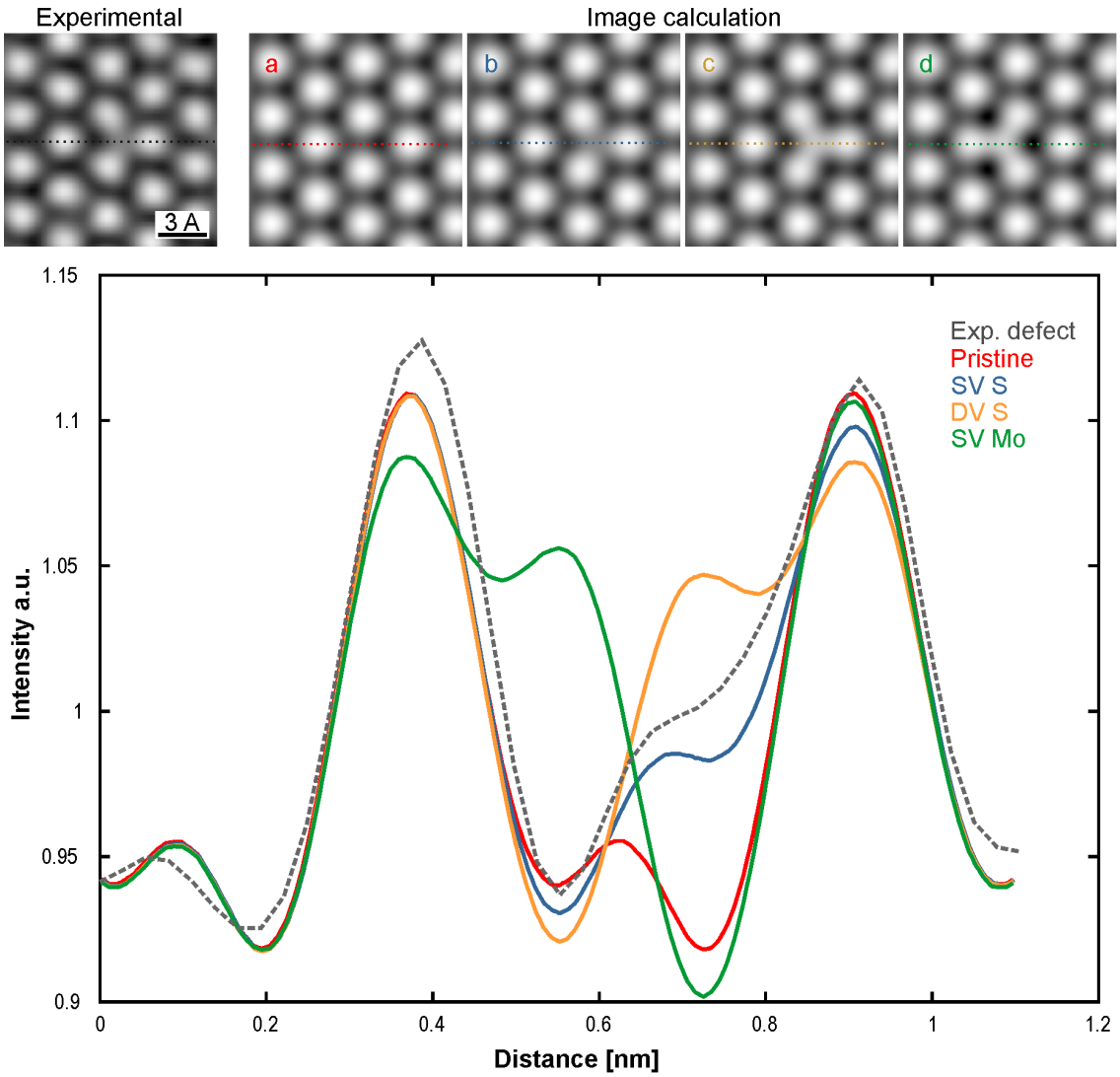

Figure 5.2.4. A defect in the experimental image can be seen by the decrease contrast. Image calculation of pristine MoS_2, single vacancy of S (SV S), double vacancy of S (DV S) and single Mo vacancy (SV Mo), a-d respectively. The graph shows a line profile from each image. The dotted line corresponds to the experimental image and the coloured lines correspond to the calculated images.

From the knowledge of the S and Mo atom positions (Figure 5.2.4), the structure of MoS_2 can be atomically characterised and its edge termination resolved. Based on detailed analysis of the edges of MoS_2 encapsulated between graphene membranes (Figure 5.2.5) it was determined that micromechanical cleaved MoS_2 has sulphur terminated edges, as has been theoretically predicted. The previous reported ex-

periments[54] on free-standing MoS_2 showed that the edges were terminated with Mo atoms. Mo atoms terminating the edge is evidence that during imaging the sulphur atoms have been sputtered by the e-beam. Moreover, this difference in results indicates that by encapsulating MoS_2 between graphene sheets the pristine structure of MoS_2 is preserved, i.e. graphene acts as protective layer against radiation damage.

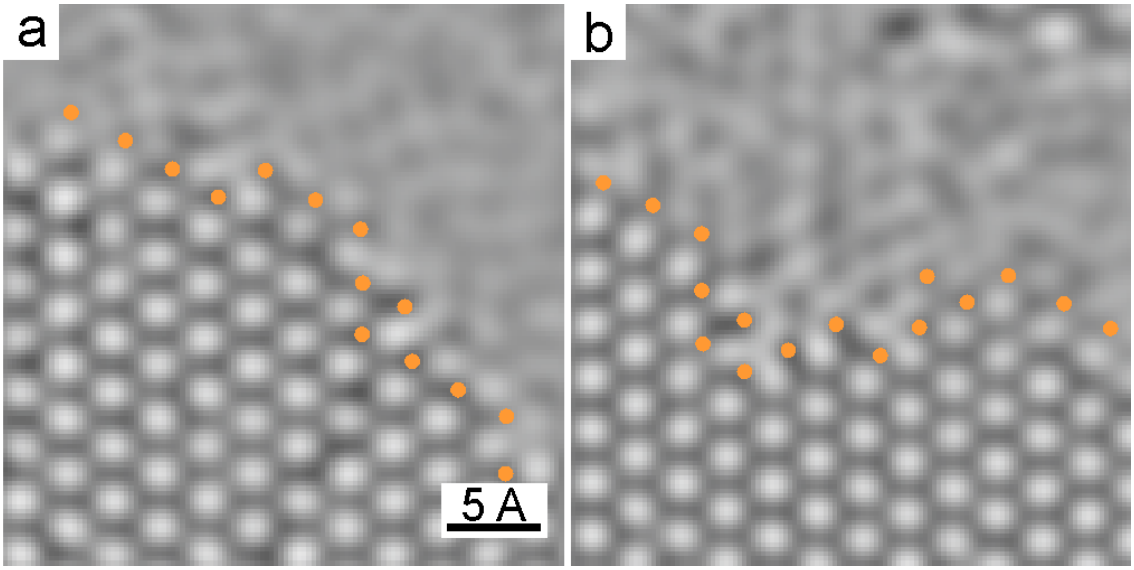

Figure 5.2.5. (a and b) Fourier filtered HRTEM images of MoS_2 in a graphene/MoS_2/graphene heterostructure. Positions of Sulphur atoms are marked with yellow circles to show that the edges are terminated with Sulphur atoms.

Because the heterojunction was made with micromechanical cleaved layers, in some parts of the sample was possible to find configurations where the MoS_2 was not protected by two graphene sheets but by only one (MoS_2/graphene). Therefore, this experiment has allowed the analysis of the vacancy production cross-section in different heterostructure configurations.[57] Vacancy production cross-section, ρ [barns]= $\frac{\Delta N}{N\phi}$ (ΔN number of S vacancies, N total number of S atoms and ϕ accumulated electron dose) was calculated for pristine MoS_2, MoS_2/graphene, graphene/MoS_2 and graphene/MoS_2/graphene configurations, resulting:

- pristine MoS_2= 4.5 ± 0.4 b
- graphene/MoS_2=1.5 ± 0.2 b
- MoS_2/graphene= 0.48 ± 0.04 b
- graphene/MoS_2/graphene= 0.008 ± 0.003 b.

From the calculated vacancy production cross-sections, the heterostructure configuration with the lowest vacancy production cross-section is graphene/MoS_2/graphene. This cross-section is 600 times smaller than the vacancy production cross-section for free-standing pristine MoS_2. Thus it has been quantitatively proved that graphene, indeed, protects electron beam sensitive materials.

§ 6 Creation of new structures on graphene

> "Irradiating solids with energetic particles is usually thought to introduce disorder, normally an undesirable phenomenon. But recent experiments on electron or ion irradiation of various nanostructures demonstrate that it can have beneficial effects and that electron or ion beams may be used to tailor the structure and properties of nanosystems with high precision. Moreover, in many cases irradiation can lead to self-organization or self-assembly in nanostructures."
>
> Krasheninnikov A.K. and Banhart F. Nature Materials. **2007**, 6, 723-733.[62]

6.1 Fabrication of SWCNT from bilayer graphene

> Algara-Siller G., Santana A., Onions R., Suyetin M., Biskupek J., Bichoutskaia E., Kaiser U. Electron-beam engineering of single-walled carbon nanotubes from bilayer graphene. Carbon 2013, 65, 80-86.[63]

Has been reported that energetic electrons (80 keV) do not cause displacement of carbon atoms in the pristine structure of graphene. Nevertheless under the electron beam the structure of graphene can be disturbed when catalyst or radical atoms interact with the carbon atoms of graphene, thus leading to structural transformations of graphene. Carbon atoms at the edges of graphene have lower threshold energy, compared to those atoms within the crystal, so these atoms can be displaced even with 80 keV electrons leading to the formation of new low dimensional carbon structures. For example, it was demonstrated[64,65] that single carbon atom chains formed from graphene constrictions or the formation of fullerenes from a small flat graphene patch.[66] If the energy of the electrons was to be higher, i.e. >90 keV, then atomic displacement will occur.[26] Thus, by using high energy electrons the structure of graphene can be tailored to formed new carbon structures.[67,68] These reports show that a wide range of carbon nanostructures can be produced by nanosculpting multilayered graphene with high energy electrons, e.g. nanoribbons.

A conventional microscope works within a range of acceleration voltages, e.g. 80-300 kV, and advanced microscopes can be used in TEM and scanning TEM mode. In TEM mode the beam is broad while in scanning TEM the beam is focused to form a beam with subnanometer diameter.

An experiment was designed to produce SWCNTs from nanoengineered bilayer graphene nanoribbons (BGNR).[63] Bilayer graphene (BG) was tailored by scanning TEM with a focused (300 kV) electron beam with a nanoprobe of 48 μA, dwell time 13 μs and a camera length of 0.160 m. To obtained BGNRs, sets of parallel lines were cut out by line scanning. The completeness of the cut through the BG was confirmed by annular dark field imaging. The width of the BGNRs ranged between 5-10 nm and their length between 20-70 nm. The resulting system was characterised with HRTEM at 80 kV with an electron beam dose rate of 1.88 x 10 ^{6} $e^{-}/nm^{2}s$.

Figure 6.1.1 (a) shows a HRTEM image of the initial state of a BGNR (5 nm wide and 20 nm long) after being nanoengineered with 300 keV electrons. In this frame is possible to observe remaining adsorbates (green arrows), small patches of graphene on the surface of BG and BGNR (red circle) and a BGNR-constriction in the middle of the BGNR (blue arrows). The loss of carbon atoms, induced by e-beam, destabilizes BG and BGNR structures at their edges by the increase of the number of dangling bonds. The carbon atoms at the edge of one layer reconstruct forming new bonds to edge carbons atom of the other layer, zipping up the edges, stabilizing the structure.[69] Figure 6.1.1 (b) shows the BGNR with most of its edges closed (black dotted lines). The closed edges are discerned by the strong contrast due to the increased number of atoms in the projection. It is also observed that a BGNR-constriction has thinned down to $\sim$2 nm, and the graphene patch has transformed under the e-beam to graphitic cage, i.e. fullerene (red circle).

This system of closed-edge BGNR and BGNR-constriction experiences further transformations under the e-beam as seen in the sequence shown in Figure 6.1.2 (a-d). The BGNR-constriction in Figure 6.1.2 (a) has open edges with a single layer graphene extension (inscribed by red line) which transforms to a closed-edge BGNR-constriction after an accumulated dose of 1.10 x 10^{9} e^{-}/nm^{2} (Figure 6.1.2 (b)). In panel (b) the edges of the constriction ($\sim$1 nm at the wider part and $\sim$0.7 nm at the thinnest section) have closed forming sharp kinks. Sharp kinks in a closed-edge structure are formed by a combination of pentagons and heptagons or vacancies.[70]

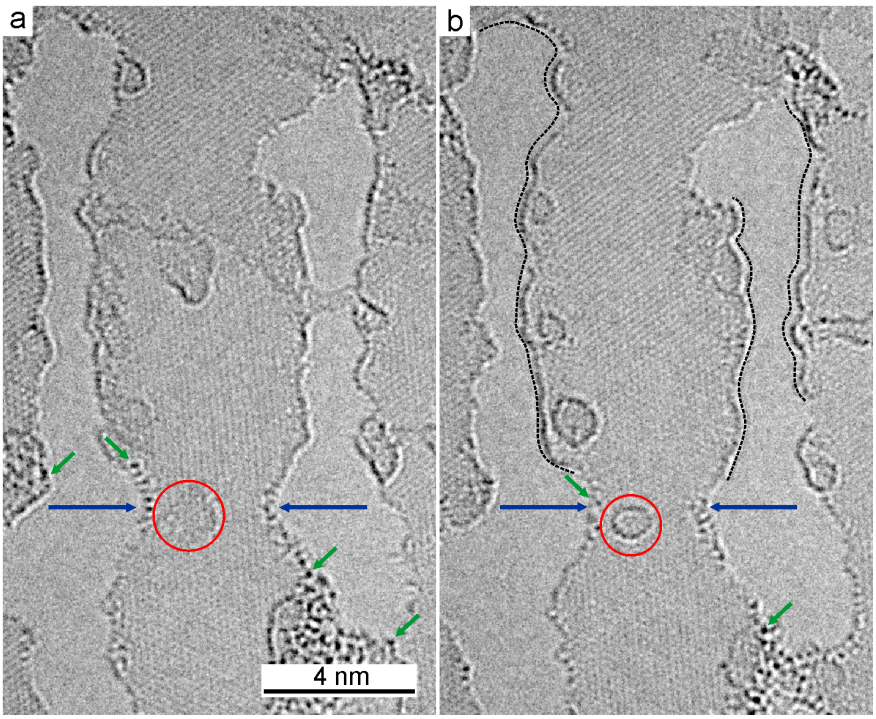

Figure 6.1.1. (a) BGNR engineered in BG, 5 nm width and 20 nm long. The blue arrows point to BGNR-constriction, black arrows to small graphene patches and green arrows point to adsorbates. (b) Image of the same BGNR after an accumulated dose of 4.32 x 10^8 e^-/nm^2. The edges of the system are already closed (black dotted lines). The BGNR-constriction has thinned down to 2 nm (blue arrows). Remaining adsorbates are still seen (green arrows).

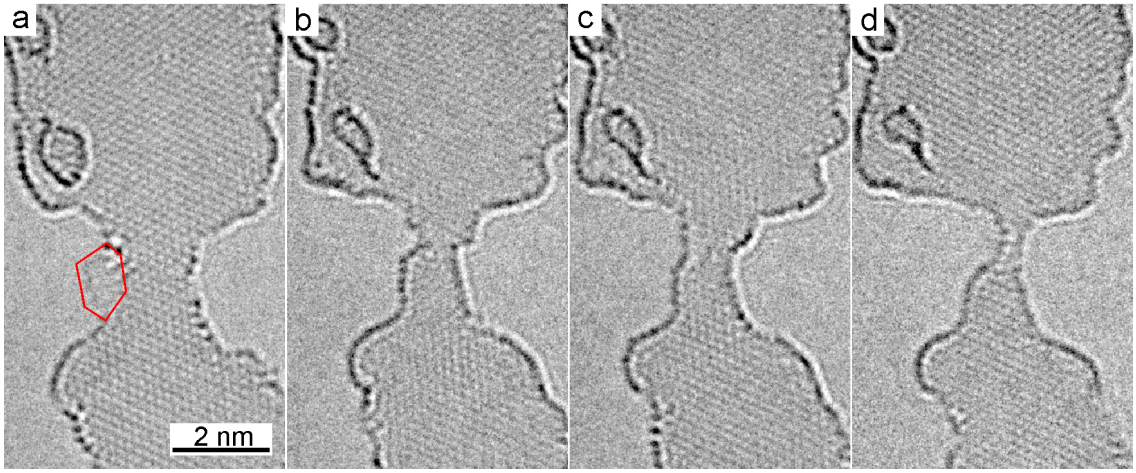

Figure 6.1.2. HRTEM images with an accumulated dose of: (a) 9.7 x 10^8 e^-/nm^2, (b) 1.10 x 10^9 e^-/nm^2, (c) 1.2 x 10^9 e^-/nm^2, (d) 1.44 x 10^9 e^-/nm^2. (a) Close-edge BGNRand a BGNR-constriction (1.5-2.0 nm width) where the BGNR-constriction has open edges and an extension of single layer graphene (within the red line). (b) The edges of the BGNR-constriction have thinned down and closed with sharp kinks. (c) Under the e-beam the closed-edges of the BGNR-constriction have been reconstructed leading to smooth edges (thinnest section 0.9 nm). (d) The closed-edge BGNR-constriction thinned down to a width of 0.5 nm. Thereafter the constriction breaks (not shown).

Hence the carbon atoms at these sites are easy to transform under the e-beam. After an accumulated dose of 1.2 X 10^9 e^-/nm^2 the constriction has reconstructed in to a closed-edge BGNR-constriction (width ∼0.9 nm) with smooth edges (Figure 6.1.2 (c)). The closed-edge BGNR-constriction suffers further transformations and thins down to a width of 0.5 nm before breaking (Figure 6.1.2 (d) accumulated dose of 1.44 x 10^9 e^-/nm^2).

Due to the fact that a HRTEM image is the projection of the atom positions, the 3 dimensional structure of the formed closed-edge BGNR-constriction can not be retrieved from a single image.

As a first approach to understand the structure in the formed system, a model of a BGNR (similar to the BGNR shown in image 6.1.1) with close edges (width=5.7 nm) was constructed and optimised using Dreideing-like force field method[i] (Figure 6.1.3 (a)). The separation, after optimisation, between graphene sheets is 3.4 Å and the closed-edges are seen as tubular. This model is in good agreement with literature, where a closed-edge BGNR has been predicted to have fractional nanotubes at its edges, with an optimum radius of curvature dependent on the width of the BGNR, such structure can be thought as a collapsed SWCNT.[71] In such systems, the greater the initial width of the BGNR the stronger the van der Waals forces between layers and the smaller the radius of curvature of the edges.[72,73] But if the width of a collapse nanotube decreases then the strain of the edges overcomes the van der Waals forces and pulls apart the graphene layers to form a SWCNT.

Molecular dynamics (MD) simulations on two systems similar to the obtained by experiments (Figure 6.1.2 (c and d)) showed that these thin (0.9 and 0.5 nm in width) closed-edge BGNR-constrictions are indeed SWCNTs (Figure 6.1.3 (b and c)). Moreover the simulations conclude that the formed SWCNT is flattened. The resulted simulations, from top view, can be seen in the left panels of (b) and (c). The red areas in these panels indicate the closed-edge BGNRs to which the SWCNTs are attached to. The right images in each panel are the image simulation of the models, which indeed, are in good agreement with the experimental results. The insets in Figure 6.1.3 (b and c) show the cross sections of the two SWCNTs where the red and blue axes indicate the major (R_x) and minor (R_y) axes respectively. The

[i]Discovery Studio Modelling Enviroment, Release 3.1, San Diego: Accelrys Software Inc. 2012

degree of flattening, described as a dimensionless parameter by $f = (R_x - R_y)/R_x$, has been calculated for the resulting SWCNTs. The larger tube has a degree of flattening f=0.23 and the smaller tube of f=0.12, Figure 6.1.3 (b) and (c) respectively. The degree of flattening in these SWCNTs can be attributed to the long range van der Waals interactions between graphene sheets from the BG and the closed-edge BGNR which dominate and affect structures with diameters close to the stability limit of SWCNTs.[62]

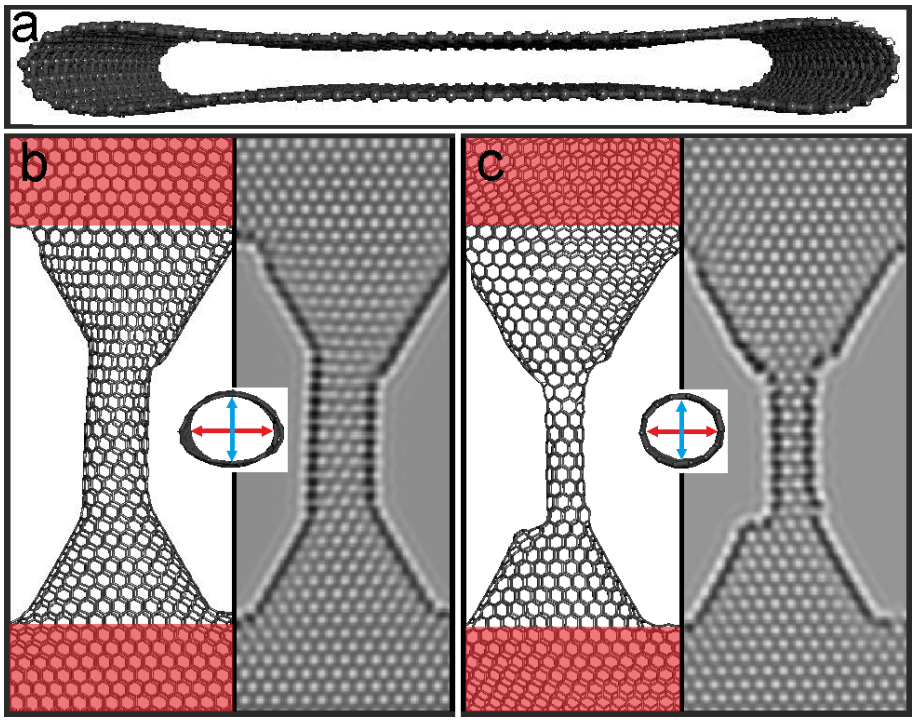

Figure 6.1.3. (a) cross section of closed-edge BGNR model depicting the experimental BGNR. The interlayer distance at the centre is 3.4 Å and its edges are fractional nanotubes. (b) top view of a model of a closed-edge BGNR-constriction (width 0.9 nm) simulating the experimental system in Figure 6.1.2 (c). The red areas are the nanoribbon sections to which the SWCNT is attached to. In the inset is seen the cross section of the SWCNT with the major and minor axes (red and blue arrows respectively). This deformed SWCNT has a degree of flattening of f=0.23. In the right panel of image (b) the image calculation is shown, which is in good agreement with experimental image. (c) Shows a model and image calculation (left and right) simulating the thinnest SWCNT obtained experimentally, 0.5 nm wide. In the inset, the cross section of the SWCNT. Its degree of flattening is f=0.12. This SWCNT is in the limit of stability for SWCNTs. (Image reproduced from Algara-Siller et al.[63] within reproduction rights given by Elsevier).

The electronic properties of SWCNTs change upon deformation, i.e., degree of flattening.[74–76] Thus, density functional theory (DFT) simulations, on pristine and deformed SWCNTs (7,0) and (11,0), were performed. With these simulations the density of states (DOS) were obtained (Figure 6.1.4). For a (7,0) SWCNT with f=0 the DOS revealed a bandgap of 0.5 eV. If this nanotube is deformed to f=0.15 the

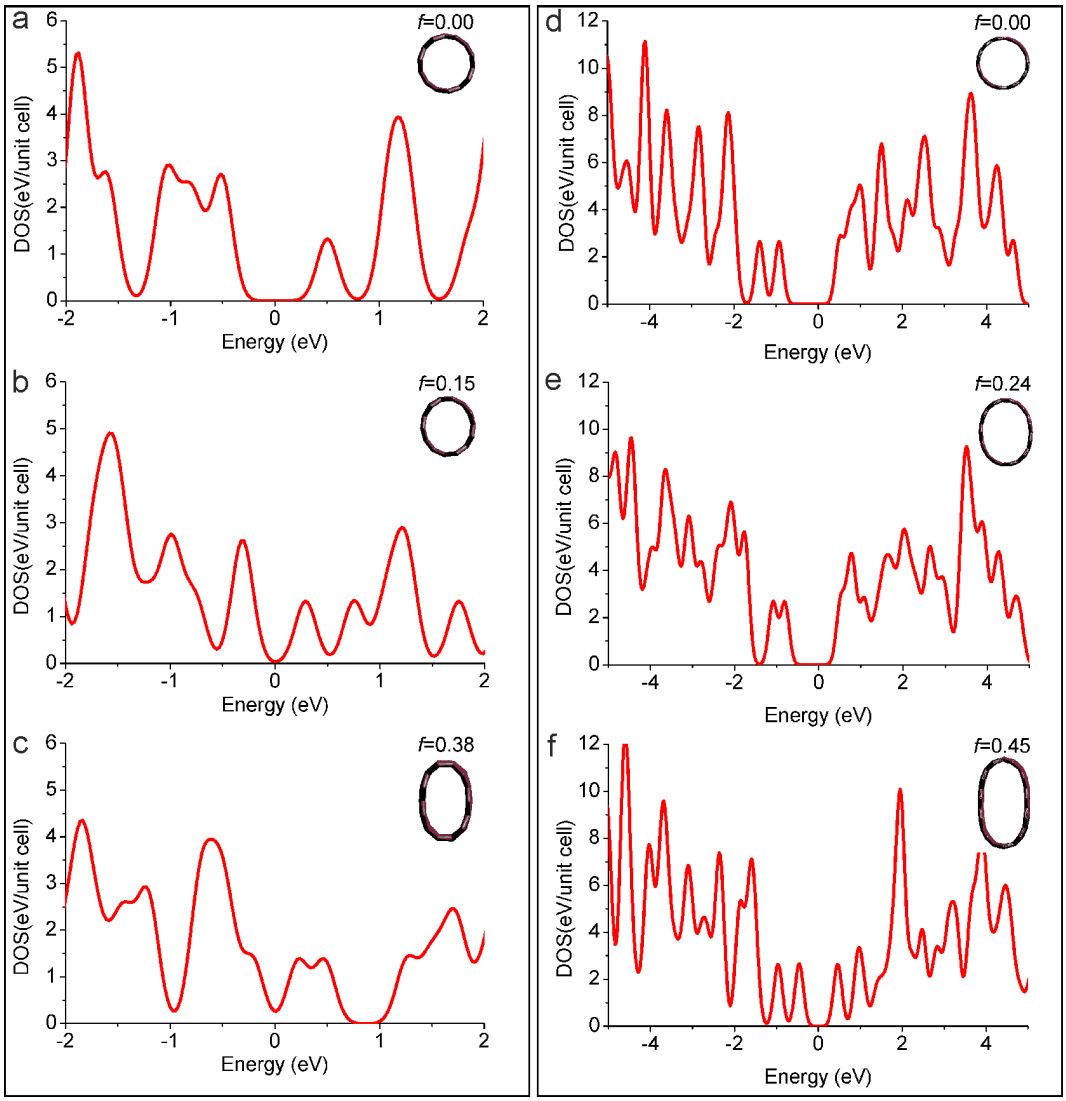

Figure 6.1.4. DFT simulations of density of states for (7,0) SWCNT (a-c) and (15,0) SWCNT (d-f) under different deformations.

bandgap is reduced to 0.1 eV (Figure 6.1.4 b), the degree of flattening in the latter tube is similar to the experimentally obtained in Figure 6.1.2 (d). But if the degree of flattening increases to f=0.38 then the SWCNT becomes metallic (panel (c)). The same simulation for the larger tube gives results that are in agreement with the decrease of bandgap upon flattening (Figure 6.1.4 (d-f)). For this larger tube, the metallization can not be reach even at a high degree of flattening f=45. Thus the insulator-metal transition in a large SWCNT will occur only upon collapsing.

6.2 Growth of single layer graphene by e-beam irradiation

The principle of CVD growth of graphene is to supply carbon atoms which will arrange in a sp^2 configuration on the surface of a metal surface (catalyst) under defined temperatures, pressures and gas flow conditions. Previous investigations have reported the growth of graphene on a non metal substrate, i.e graphene. Westenfelder et al.[77] investigated the formation of polycrystalline graphene (1-5 nm grain size) at very high temperatures on a graphene substrate. This report describes the transformation phenomena of hydrocarbon contamination (300 K) to amorphous carbon (1000 K) to polycrystalline graphene (2000 K). Nevertheless, the detailed description of the transformation process is left unclear. An independent work by Barrerio et al.[78] reported the growth of large graphene areas by current-induced annealing. The methodology, although similar to Westenfelder et al., differs on that the sample was annealed (cleaned), let to cool down allowing redeposition of contamination, and heated again up to $\sim$ 2000 K. This work suggests that high temperatures are required to transform the redeposited amorphous carbon to graphene. Furthermore, the transformation is described by molecular dynamics simulations where the amorphous carbon transforms to a glass-like phase at 600 K and it starts to form a new graphene layer on the graphene substrate at around 1800 K. Another type of graphene formation by carbon atoms from contamination is the re-knitting of holes on graphene reported by Zan et al..[79] Their results showed that carbon atoms from a nearby clump of contamination diffuse in to the graphene hole during imaging and knit it until the hole is mended. Apart from this observation, it was mention the formation of small patches of "near amorphous" carbon adlayers, i.e. very defective graphene, from contamination. Because the latter reports on growing graphene from contamination either involve high temperatures[77,78] or a focus probe,[79] i.e. low spatial and temporal resolution, the description of the growth of graphene from contamination on graphene at the atomic level is otherwise missed.

In this section a detailed (atomic level) characterisation on the formation of a graphene adlayer from contamination is presented. A sample, graphene grown on Cu by CVD and transferred to a TEM, was treated with activated alumina powder on a first approach to clean graphene (for more information see Chapter 7). Because at this stage of the thesis no optimization for the cleaning treatment was

done, the sample showed to have residual contamination (Figure 6.2.1). The leftover adsorbates, morphologically, do not resemble ordinary contamination of untreated graphene, i.e. they are in stripe-like form (red lines in Figure 6.2.1 (a) and seen with higher magnification in (b)).[ii]

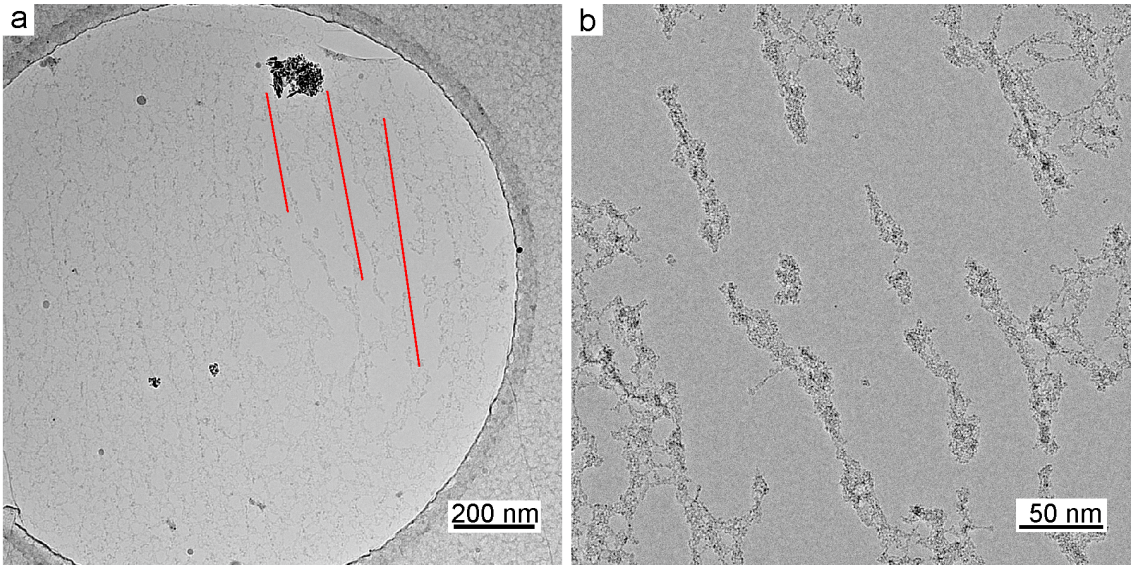

Figure 6.2.1. (a) Low magnification TEM image (3595 e^-/nm^2s) of the graphene sample after treatment with activated alumina. Some contamination stripes are pointed out by red lines. (b) High magnification image of an area from (a).

The contamination stripes, qualitatively, do not change morphology under electron dose rates of 3595 e^-/nm^2s - 4.2 x 10^4 e^-/nm^2s. But if a higher electron dose rate is applied (6.7 x 10^6 e^-/nm^2s), then at the end of one of the contaminations stripes an adlayer graphene starts to form from the contamination. The growing process of an adlayer graphene from contamination is shown in Figure 6.2.2 (a-l). This sequence lasts 354 seconds and with it the growth rate of graphene adlayer was obtained. The adlayer growth was measured from a reference point (red dot in all images) to a reference growing direction, i.e. bottom-right corner. Although these measurements are rough approximations they give a fair estimate of the growing rate.

The growth rate of graphene is better seen in Figure 6.2.3 where each measured point corresponds to each of the images, from (a)=0 s and 0 nm to (l)=354 s and 13.8 nm. The lack of growth between 0 to 100 seconds suggests that a reasonable amount of energy should be put in to the system before the single layer graphene starts growing. Perhaps physical and chemical processes, for example heating for

[ii]Discussion about contamination stripes see Chapter 7

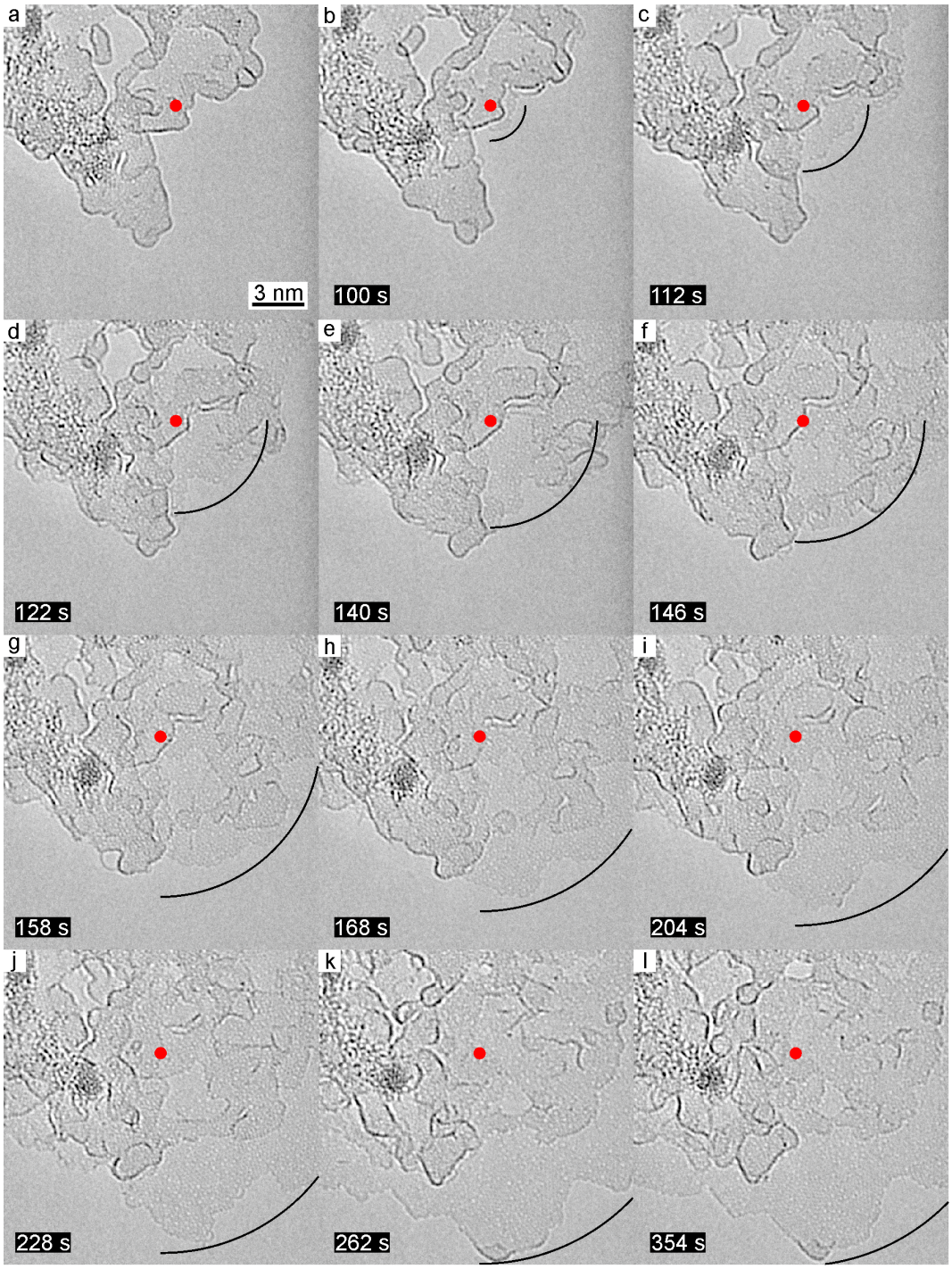

Figure 6.2.2. Fourier filtered image sequence of the growing of an adlayer graphene on a graphene substrate. The sequence from (a-l) last 354 seconds. The black lines indicate the edge front of the adlayer graphene. Each image shows the number of seconds after (a) when the image was taken.

diffusion, breaking up the contamination to obtain carbon species, have to be enable by the electron beam before the growth. Once the first edge of the adlayer graphene is formed (Figure 6.2.2 (b)), the growth rate is ~ 0.1 nm/s and leads to

the formation of polycrystalline graphene (panels (b-h) in Figure 6.2.2). After ∼ 186 seconds the growth rate starts to decrease (i-l), indicating that the reservoir of carbon atoms in the contamination is reaching depletion until the growth stops (≈ 354 seconds).

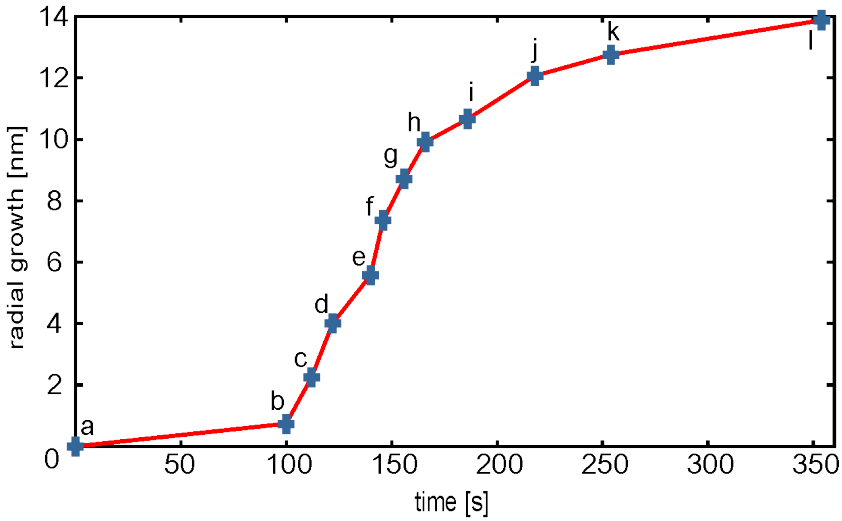

Figure 6.2.3. Graphene adlayer growth rate. Each point corresponds to measurements of radial growth length and time for each of the images in Figure 6.2.2.

During the growth of the adlayer graphene, the structure of the adlayer edge front can be characterised due to the spatial resolution achieved in our HRTEM studies. Figure 6.2.4 shows a frame from the image sequence to which a Fourier filter has been applied. In this image some edges have superimposed hexagons (black), heptagons (red) and pentagons (blue) to exemplified the edge termination of the adlayer. Grain boundaries in graphene are mostly formed by heptagons and pentagons[80] (example of grain boundaries marked by black lines) so it is expected that within a growing polycrystalline adlayer (many boundaries) some of those pentagons and heptagons will terminate the edge (green arrows).

Furthermore, as the adlayer grows with randomly oriented grain domains there are some grains at the edge-growing front that have zigzag termination, and as a zigzag edge has a high energy configuration per atom (1.3 eV/Å) thus it reconstructs with heptagons and pentagons which have the lowest edge energy configuration per atom in a graphene edge (≈0.95 eV/Å).[81] The analysis of the edges throughout the growing edge front of the adlayer graphene resulted in, as expected, that most of the edges were terminated in heptagon-pentagon (reconstructed zigzag) or armchair configurations. The latter description is in good agreement with the experimental

results of Koskinen et al.[82] and Westenfelder et al.[77]

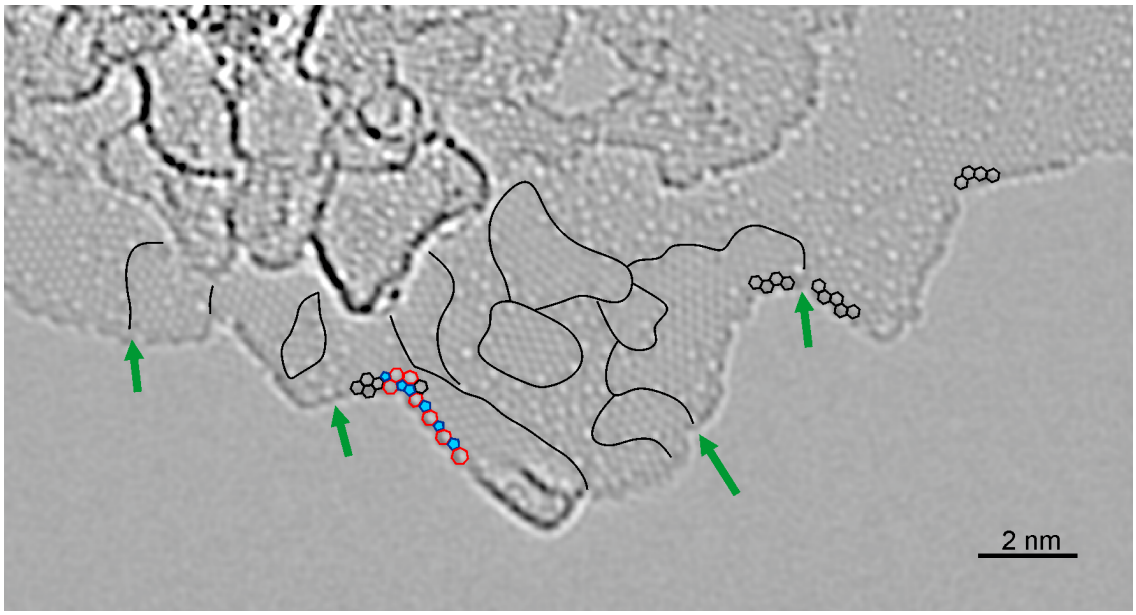

Figure 6.2.4. Fourier filtered HRTEM image of the adlayer edge front. Superimposed polygons (black hexagons, red heptagons and blue pentagons) at the edge indicate the termination of the edge front. Most of the edges terminate either in armchair or by heptagons and pentagons (reconstructed zigzag).[82]

From an overall view of the area where the adlayer graphene has grown, Figure 6.2.5 (a), it can be seen that not only one layer graphene grew but two layers (blue line delimits the first adlayer and red line the second adlayer). It is worth noting the nanometer size polycrystallinity of both adlayers. For example, the grains in the first adlayer range between 1-9 nm^2 (coloured areas in Figure 6.2.5 (b)). Moreover, the area of the grown adlayer graphene is restricted to the diameter of the electron beam during imaging i.e. $\approx$ 200 nm (Figure 6.2.5 (c)). The adlayer which radially grows from the contamination (see that clean areas are not fully cover), coalesces with other adlayers (from other contamination spots) creating a continuous polycrystalline graphene film. To corroborate that the growth of this adlayer graphene was not a fortunate incident, the same experimental parameters were applied in other areas of the sample. Results show that if an area which is qualitatively different in terms of contamination (Figure 6.2.6 (a)) than the one shown on Figure 6.2.1, the growth of an adlayer graphene does not occur, even after a total dose of 8.8 x 10^8 e^-/nm^2. But if another place in the sample (Figure 6.2.6 (b)) with similar contamination to Figure 6.2.1, i.e. big clean areas in-between contamination stripes, is imaged then the adlayer graphene grows from contamination (Figure 6.2.6 (c)).

This grown adlayer graphene shows the same characteristics as the one described before: edges growing in armchair termination, polycrystalline with grain sizes between 1-5 nm^2, second adlayer growth, and size of the adlayer dependent on the beam diameter.

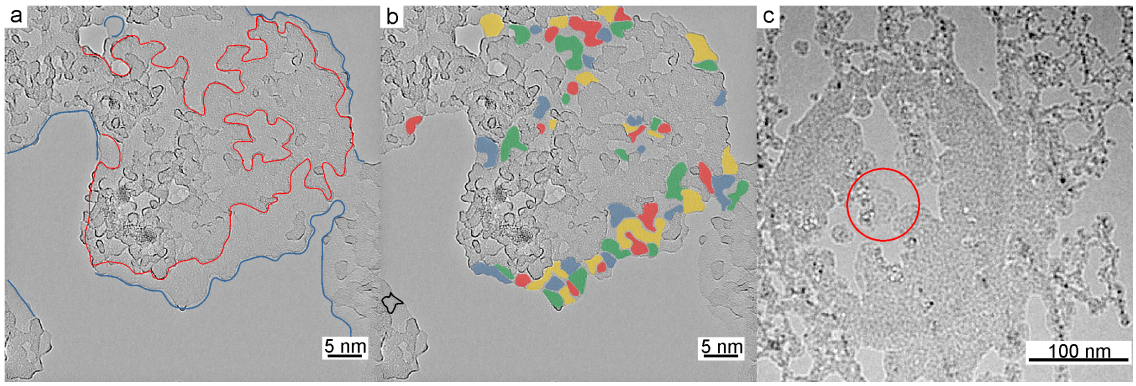

Figure 6.2.5. The Fourier filtered image on (a) shows a general view of the adlayer graphene that grew on graphene by e-beam. The blue line delimits a single adlayer and the red line the second adlayer. (b) Grains from the first layer are highlighted in colour. The area of these grains range between 1-9 nm^2 being 3 nm^2 the average. (c) Total area of the grown adlayer corresponds to the electron beam size $\approx$ 200 nm Ø.

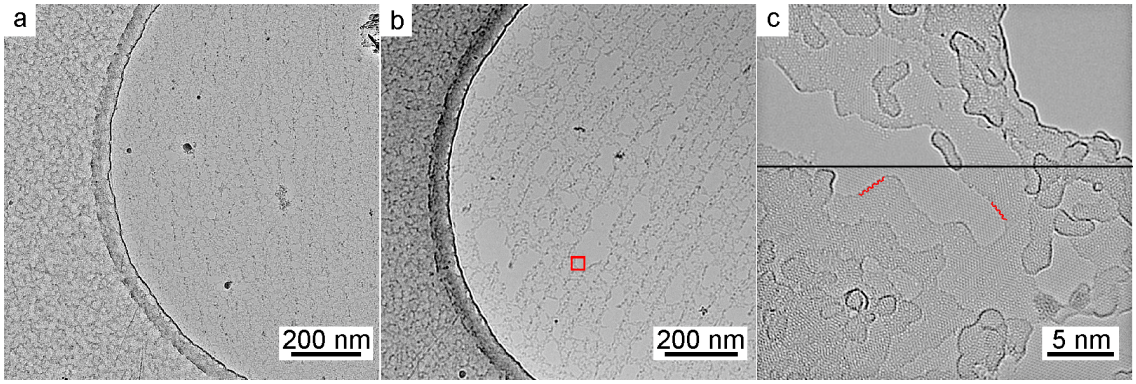

Figure 6.2.6. (a) Low magnification image of another place in the sample where the adlayer growth did not occurred (qualitatively different contamination to Figure 6.2.1). (b) Image of graphene with similar contamination to Figure 6.2.1. (c) A HRTEM image of an area marked in red in (b) (averaged over 10 frames). The bottom part shows the unfiltered image of the adlayer graphene where the armchair terminated edges are highlighted with a red line. The upper part shows the Fourier filtered image, where grains and grain boundaries are clearly discern (grains range between 1-5 nm^2).

It has been demonstrated with this experiment that the adlayer graphene can be grown on a graphene substrate by electron beam irradiation without the need of extreme heating. Furthermore, it has been proven that for an adlayer graphene to grow from contamination sites it needs big pristine areas of graphene substrate to

grow on. Although the exact elemental composition of the remnant contamination in this study, or in the reports mentioned before, is not known, the results converge to notion that for a new graphene adlayer to form, the right contamination, i.e. carbon source, should be present in the surface of the graphene substrate.

6.3 Formation of square ice from water encapsulated between graphene sheets

> Algara-Siller G., Lehtinen O., Wang F.C., Nair R.R., Kaiser U., Wu H.A., Geim A.K., Grigorieva I.V. Direct imaging of square ice in graphene nano-channels. Submitted. **2014**.

> "The phase transition of liquid water into ice is a physical phenomenon of abiding scientific interest related to environmental, biological, and technological processes."
> Choi E.-M., Yoon Y.-H., Lee S., Kang H. Physical Review Letters **2005**, 95, 085701.[83]

Experimental evidence in the dynamical properties of liquids (e.g. OMCTS[iii]) in a confined environment has proven that a liquid retains its bulk properties down to a critical gap separation. But upon further confinement (gap decreased by one molecular layer) the liquid abruptly solidifies.[84] Solidification of water to bulk ice is a complicated problem thus the existence of 16, experimental or theoretical, different types of ice phases. Gavish et al.[85] reported that nucleation of ice on hydrophobic surfaces may be initialised by a mechanism derived from an electric field. It was suggested that the electric field induces the alignment of water molecules thus promoting ice crystallization. Choi et al.[83] proved experimentally the formation of polar cubic ice at room temperature within a gap (7 Å) of gold electrodes by an small electric field (10^6 V/m) . With these results it was revealed that the gap distance, as expected for liquids, plays an important roll in the nucleation promoting ice formation. Theoretical simulations of confined water at 265 K,[86] predict the transition of monolayer water to monolayer ice in dependence of gap separation and that this transformation does not require an applied electric field. The simulations were extended[87] in order to predict the phase transition of a bilayer water at 300 K upon pressure or decrease gap separation. It was found that bilayer

[iii] octamethylcyclotetrasiloxane is a nonpolar liquid which has been used as a reference model for liquids.

ice will only form if water is confined within a gap separation between 6.4-7.2 Å. The dimensionality constrictions as an influential factor for ice formation has been proven by filling SWCNTs with water, these experiments confirm the formation of quasi 1 dimensional ice. Recent experiments on the permeation of water through a graphene oxide membrane[88] showed that water permeates unimpeded through graphene capillaries, i.e. water between two pristine graphene sheets. The molecular dynamics simulations on this system showed that a monolayer water rushing through a graphene capillary with a separation between 6 Å and 10 Å arranges in a an almost perfect crystalline square lattice, square ice. Furthermore, Zheng et al.[89] demonstrated that water crystallizes at room temperature under specific humidity conditions on the hydrophobic surface of graphite through nucleation at the interface between the hydrophilic graphene oxide and the hydrophobic graphite. These results corroborate the ideas that phase transitions for 2D liquids do not follow the established phase transitions concepts of bulk.

In order to prove the formation of 2D ice at room temperature in a confined environment, an experimental set up has been devised to trap water between graphene sheets, similar as the graphene liquid cell reported by Yuk et al.[90] The sample fabrication consists of two separate grids with CVD grown graphene transferred to them[iv] (Figure 6.3.1 (a)), where a drop of water was cast between the grids and let dry (b). Upon drying, water remained encapsulated between graphene sheets (c).

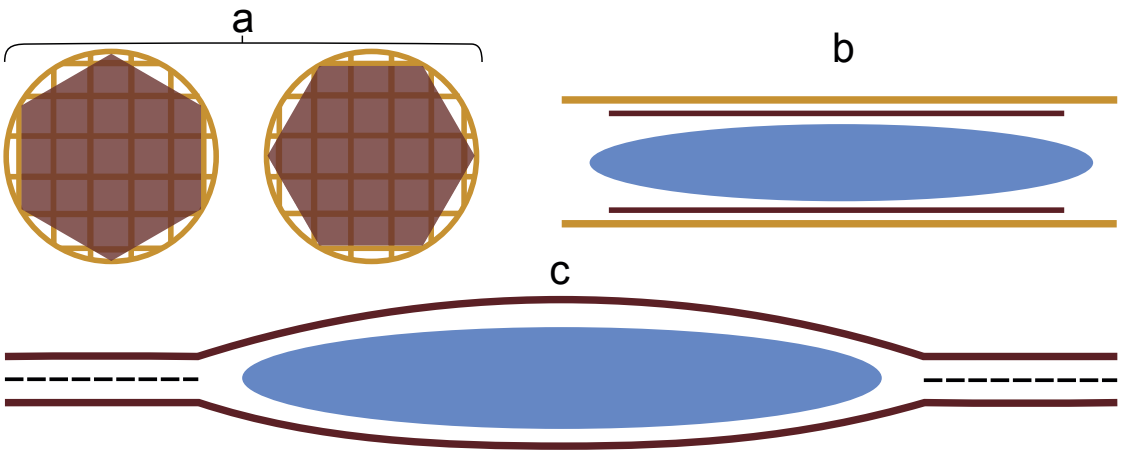

Figure 6.3.1. Graphical figure explaining the sample preparation for trapping water between graphene sheets. (a) Two grids with graphene. (b) a drop of water was cast on one grid and the second grid put on top, the sample was let to dry and water ends being encapsulated between graphene sheets (c). The dashed line emulates the contamination between graphene sheeets.

[iv] Higher reproducibility has been found when a 5nm Pt layer is deposited on the grid prior to graphene transfer.

The water encapsulated, in its initial state, between graphene sheets imaged at low magnification is shown in Figure 6.3.2 (a). Figure 6.3.2 (b) shows that the encapsulated water has transformed to crystallites. These crystallites hint the phase transformation of water in the confined environment of graphene sheets. It should be mentioned, again, that the experiment was performed at room temperature.

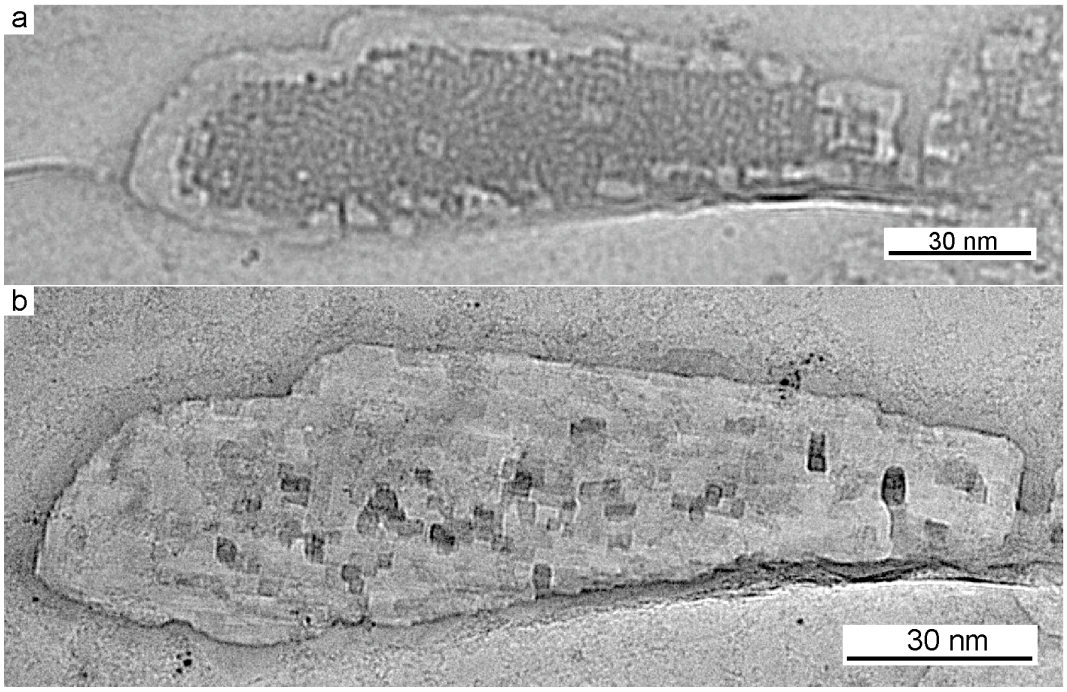

Figure 6.3.2. (a) Low magnification TEM image of water encapsulated between graphene sheets (electron dose of 600 e^-/nm^2). (b) The encapsulated water has transformed to crystallites, notice the geometrical shapes.

The exact phase transformation process could not be imaged because of the fast evolution from one phase to the other during imaging. Nevertheless, attempts can be made to explain this process. One approach is that the liquid trapped in the pocket is a mixture of water and contamination, and that upon electron irradiation the contamination separates from the mixture leaving only water confined between the graphene sheets provoking the formation of ice. Another scenario is that the gap between graphene sheets decreases, by decreasing the volume of the trapped liquid (diffusion promoted by electron beam), creating the optimum confinement environment for the water to crystallize. The exact chemical and physical processes for this phase transformation are far beyond this work, therefore the above mentioned approaches should be read as pure hypotheses which need further investigation to be proven or rejected.

Once the crystallites are formed, they become very mobile and they increase or decrease in thickness, i.e. number of ice layers, but always retaining their crystallinity during imaging. The former observation is direct evidence of the fast diffusion of water between graphene membranes[88] and the latter suggests that a second layer of ice can be grown without the need of the formation of a complete first ice layer.[91]

The resolution obtained in this study allows the retrieval of information about the structure of the crystallites. The water crystallites, which have prominent crystallographic edges (Figure 6.3.3), range in sizes between 1 to tens of nanometers. Under continuous imaging, they grow or decrease in lateral size, aggregate or diffuse. It is important to notice that the crystallites varied, also, in their thickness. For example, Figure 6.3.3 (b) shows a thin ice crystal where (c) a thicker one. The ice thickness can be correlated directly from the observable increase in contrast.

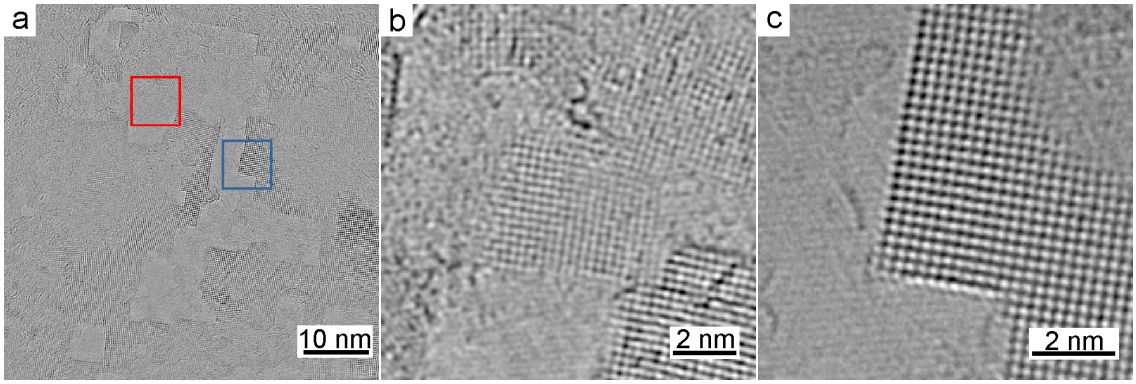

Figure 6.3.3. HRTEM images of ice crystals confined between graphene sheets. (a) Overview of ice crystals. (b and c) Examples of a thin and thick ice crystals, respectively.

With the advantage that the signal of the graphene sheets is low, compared to the signal from the crystallites, the structure of the crystallites is directly obtained (Figure 6.3.4). Analysis of the structure of ice from the HRTEM image and its FFT resulted in a measured lattice parameters a=b=2.83 $\pm$ 0.04 Å, — square ice —. In addition, the FFT (Figure 6.3.4 (b)) shows two sets of graphene reflections corresponding to the two graphene sheets confining the square ice. Square ice is the only phase observed during the experiments indicating its high stability in a confined environment. Furthermore, this is the first time to be experimentally reported the existence of square ice at room temperature.

To confirm the experimentally obtained phase of ice, molecular dynamics simu-

lations on water confined between graphene layers (6.5 Å apart) resulted in: a water monolayer arrange in square lattice with lattice parameter of 2.81 ± 0.01Å, which is in good agreement with the experiments (Figure 6.3.5 (a)).[v]

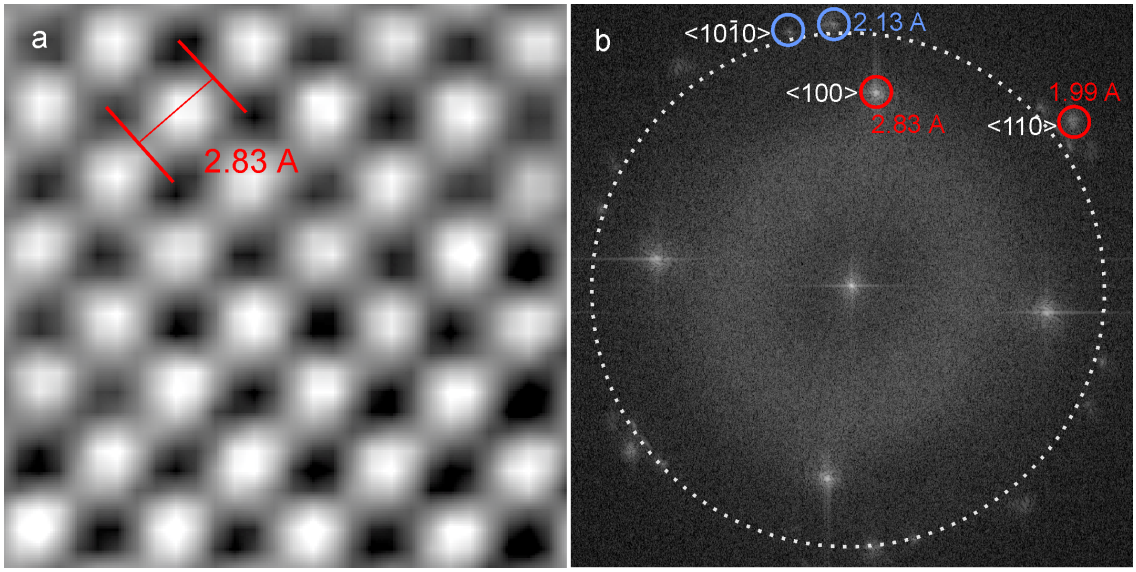

Figure 6.3.4. (a) HRTEM image of the structure of ice with lattice parameters a=b=2.83 ±0.04 Å. (b) FFT of the real space image (a). The ice reflections are circumscribed by red circles and the two sets of lattice reflections from the graphene membranes by blue circles.

With the resulted theoretical model image calculations were done, and by comparison of the calculated and experimental images (Figure 6.3.5 (b and c)) it was possible to determined the origin of the contrast. The dark spots in the image of square ice correspond to the positions of the oxygen atoms of the water molecules. Because of the lighter nature of hydrogen (Z=1) these atoms do not contribute significantly to the image contrast.

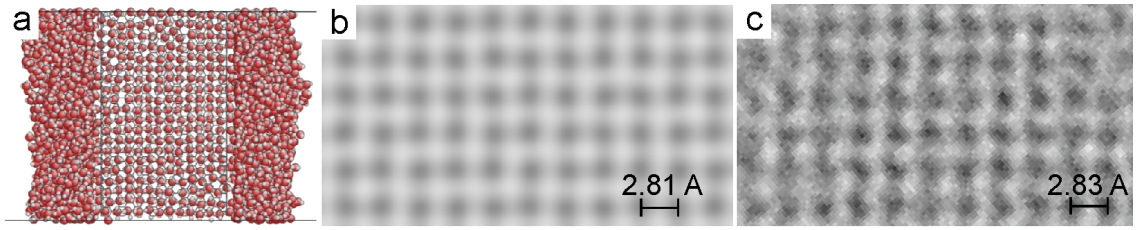

Figure 6.3.5. Comparative study between simulated square ice and experimental results. (a) MD simulation of monolayer water confined between graphene sheets. The square lattice is readily observable. (b) Image calculation based on the model obtained by MD simulations with a lattice parameter of 2.81 ± 0.01Å. (c) Experimental image of a thin ice.

[v] MD simulations were performed by Wang F.C. and Wu H.A. Chinese Academy of Sciences Key Laboratory of Mechanical Behavior and Design of Materials, Department of Modern Mechanics, University of Science and Technology of China, China.

Square ice in the experimental images showed to have a layered structure while confined within graphene sheets. As an example, Figure 6.3.6 shows a single crystal of square ice composed of a number of layers. The number of layers per increase in contrast is inferred by contrast analysis. The contrast comparison of the graphene sheets encapsulating the crystal and the contrast for each ice layer in the crystal has been calculated using the root mean square (RMS) contrast equation.[6] This equation is the standard deviation of the pixels intensity of an image. Taking the RMS of the areas of interest, the contrast resulted in an incremental stepwise variation of $\sim 2\%$ (inset top left in Figure 6.3.6) from bilayer graphene to triple-layer ice (BG, SLI, DLI and TLI respectively). Therefore, the square ice increments in one its number of layers per increase in contrast step. The layered ice is easier to discerned by: (1) applying a variance filter (10 px) to a normalize image, (2) taking the square root of the resulting image and (3) applying a Gaussian blur filter (Figure 6.3.6 top right inset). By this evidence then the experimentally obtained square ice varies between 1 to 3 layers.

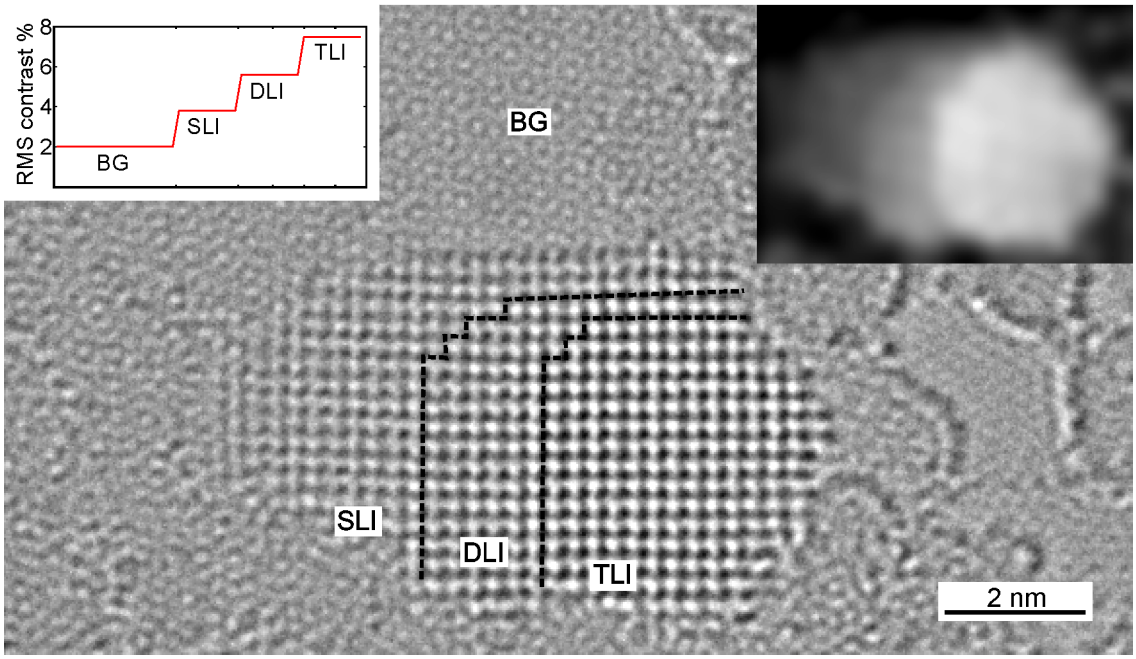

Figure 6.3.6. Layered ice. (a) HRTEM image of layered ice (dashed lines denote the increase of layers). The contrast between layers increases stepwise (b). Red green and blue line point to the start of each layer. Image simulation of triple layer square ice in (c) AA stacking and (d) ABA stacking configurations.

To verify stacking arrangement of layered square ice, image calculations were made on models of triple-layer ice with AA and ABA stacking configurations (Figure

6.3.7 (a and b), respectively). The comparison of these image calculations to the experimental image (Figure 6.3.6) results in the unambiguous determination of the stacking configuration of the square ice, i.e., in AA stacking configuration where the oxygen atoms stacked, exactly, on top of the the underlying oxygen atoms. This configuration has also been predicted for ice confined in a SWCNT,[92] therefore square ice could be the preferential phase for confined water within low dimensional carbon structures.

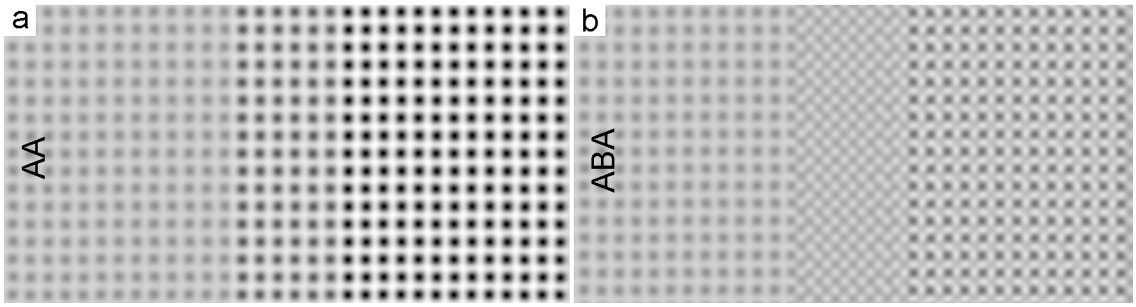

Figure 6.3.7. Image simulations of AA and ABA stacking configurations of triple-layer ice.

Crystal defects and grain boundaries can be formed because the ice crystals are highly mobile under the electron beam. For example, an edge dislocation is observed in Figure 6.3.8 (a), where the extra row of water molecules in the crystal is highlighted (blue line). In Figure 6.3.8 (b) a tilt grain boundary and dislocations originating from it are seen.

Near the grain boundary the bond length between water molecules in the ice vary up to $\sim 20\%$ (Figure 6.3.9 (a and b)). The large variation in molecule separation in strained regions like grain boundaries can be explained by the weak interactions between water molecules in ice, i.e. hydrogen bonding. Furthermore, the effect of this weak interaction becomes obvious when a row of water molecules at the edge of an ice crystal follows the contour of a contamination patch (Figure 6.3.9 (c)).

It should be pointed out that in several places within the sample, water trapped between graphene layers was found. In all cases crystallisation occurred and the crystal structure of square ice was the same, i.e. lattice parameters of 2.83 $\pm$0.04Å.

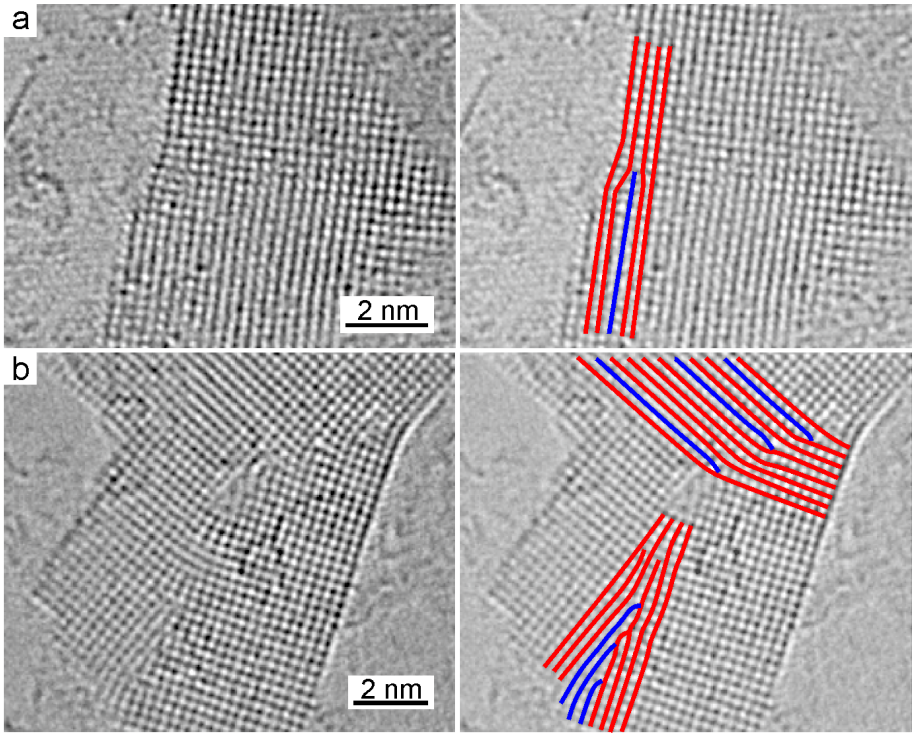

Figure 6.3.8. HRTEM images of crystal defects in square ice. (a) Edge dislocation in ice (extra row of water molecules highlighted in blue). (b) Two ice crystals coalesced and formed a grain boundary with dislocations originating from it.

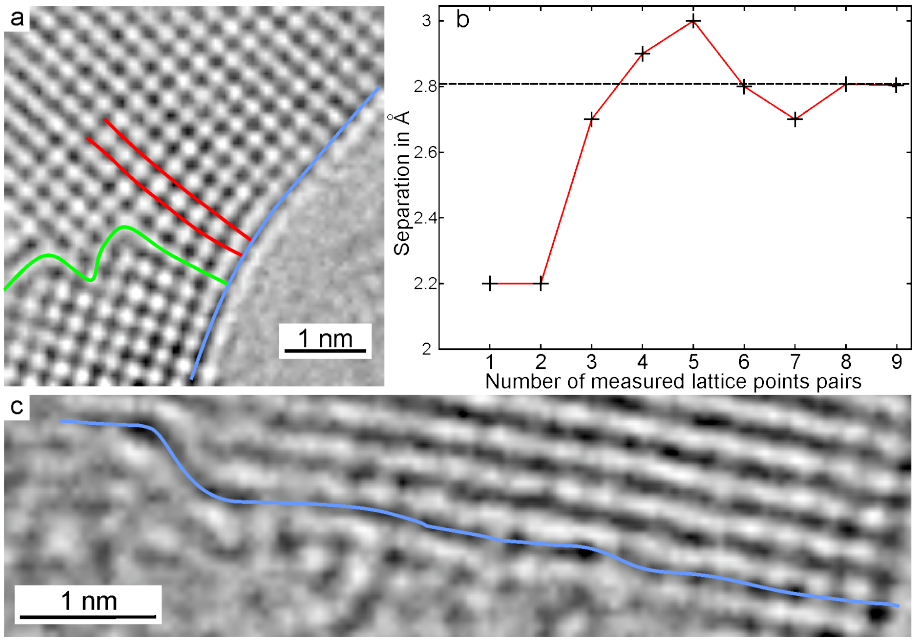

Figure 6.3.9. Effect of hydrogen bond between water molecules in square ice. (a) Bending of ice crystal (blue line) near a grain boundary (green line). Bond length variations are quantified by measuring the separation between molecules of two crystal rows (the red lines). (b) Graph showing the bond length variation. The bonds stretch and compress up to $\sim 20\%$ from the 2.83 $\pm$ 0.04 Å bond length (dashed line). (c) Bending of a crystal row which follows the contour of a contamination patch.

§ 7 Cleaning graphene

As seen in the previous chapters, graphene produced either by micromechanical cleavage or by chemical vapour deposition has all qualities to be used as TEM substrate. Recapitulating: graphene has outstanding thermal,[93,94] mechanical[95] and electrical properties.[15] The good electrical and thermal conduction lessen, if not avoid, the effects of charging and heating of the sample by the electron beam. The mechanical properties bring flexibility to sustain a wide range of objects while stability minimizes the risk of sample breakage and sample drift. Important properties of graphene concerning TEM imaging are the low signal contribution of graphene to the image and the ability to filter out its crystal reflections, therefore graphene can be regarded as a transparent substrate for TEM applications.[11] However, this holds true only if graphene is pristine. In praxis, graphene, after the transfer to TEM grids, has pristine patches only with sizes between a few nanometers to tens of nanometers in diameter, as can be seen in Figure 7.0.1. The patch of clean graphene has an area of $\sim$ 700 nm^2, which is about the size of the largest areas found, typically, in non-cleaned samples. The cleanness of graphene, ratio of contamination-free area to total sample area, without cleaning treatment is about 6%.

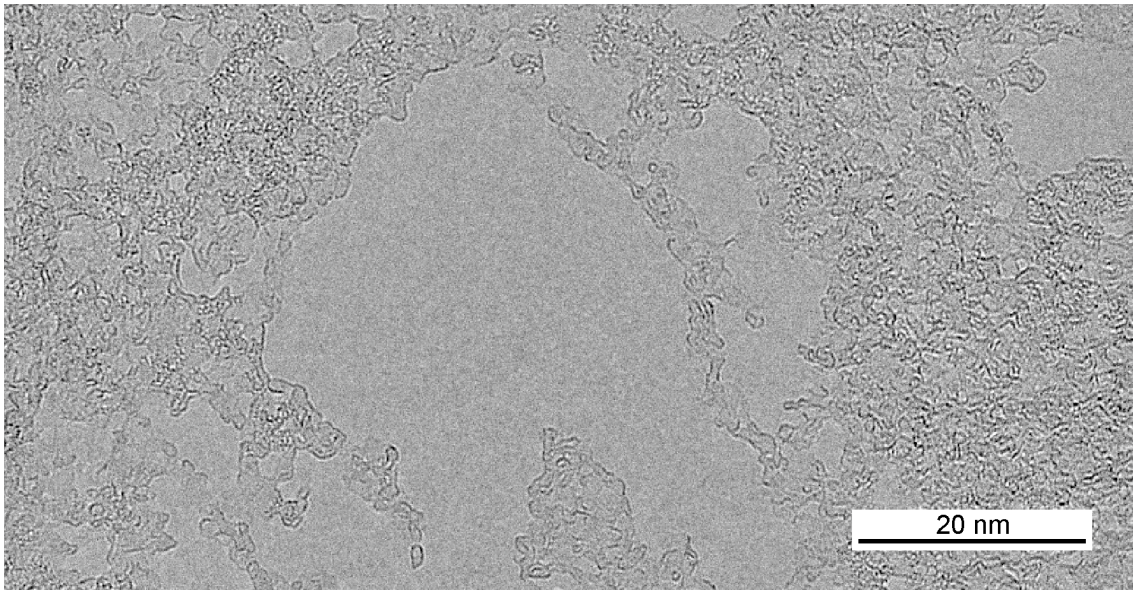

Figure 7.0.1. HRTEM image of graphene without a cleaning treatment. This image is an example of the largest clean areas ($\sim$ 700 nm^2) found, typically, in non-cleaned graphene.

Although small, in these clean areas has been possible to characterised graphene and revealed its atomic structure (Chapter 3). For some characterisations like momentum resolved electron energy-loss spectroscopy (EELS), the small pristine areas and the high amount of contamination hindered these investigations. This contamination also limits the usage of graphene as a substrate for TEM investigations of nanomaterials or molecules. One characteristic of hybrid nano-objects which was desired to obtained by TEM with the experiments reported in Chapter 4 was: how and how many of the polymer active groups, e.g. thiotic groups, are attached to the inorganic nano-object (Figure 4.1.3). This characteristic is necessary to know in order to determined the relation between materials ratio, structure, stability and properties of the nano-objects and the system. For example, if known how many thiotic groups are needed to stabilize a Au nanocluster < 1 nm, the chemistry to produce them could be optimized and high yields with smaller dispersion could be obtained. In the case of the TEM studies of DNA, the aggregation of contamination on and around the molecule contributed to the contrast in the low magnification image (Figure 4.2.2), nonetheless in HRTEM imaging, this contamination obstructed the atomic imaging of the DNA structure.

7.1 On the contamination on graphene

Surface contamination on most solids consists, often, of H_2O, CO, CO_2, and hydrocarbons, that come from the environment.[96] A clear example of the airbone contamination deposited in solids is the increase in weight of the standard kilogram.[97] In graphene, additional contamination may be introduced by the fabrication process and its storage conditions.

A surface characterisation technique that can be used to study the contamination on graphene is X-ray photoelectron spectroscopy (XPS). XPS has normally a large beam diameter, albeit its high energy resolution, thus the resulting information obtained about the contamination on graphene is the general elemental composition of the graphene and the grid. Thus an experimental set up was made to compare the elemental composition of an empty grid and a grid with CVD-graphene. The empty grid and the graphene sample were characterised by XPS under exactly the same experimental conditions. The spectra obtained (0.4 eV resolution) from both samples (Figure 7.1.1) have dominant carbon and oxygen peaks, as expected.

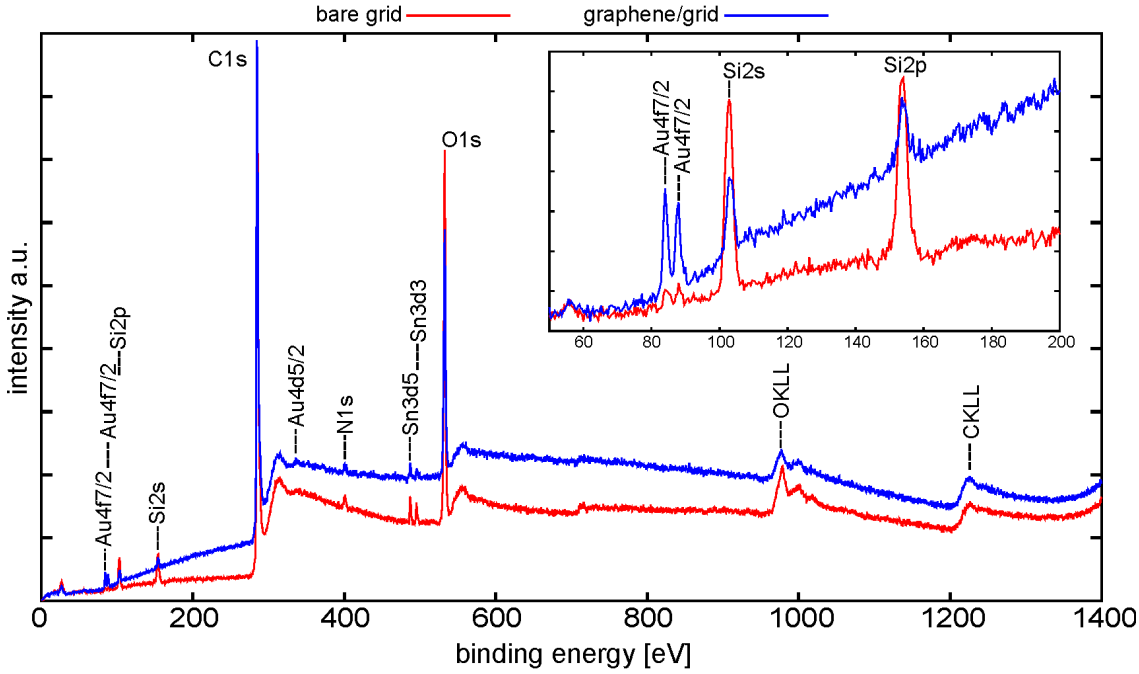

Figure 7.1.1. XP spectra of a bare quantifoil grid and graphene/grid (same experimental conditions). Inset shows detailed spectra of Au and Si (50–200 eV).

These C and O peaks originated from the graphene, its contamination, and from the amorphous carbon film of the grid. Also, common peaks, e.g. Au and Si, arise in both samples thus suggesting that these elements come from the grid and not from the graphene transfer process. A detailed comparison on the peak intensity of Au and Si (inset Figure 7.1.1) indicates that the transfer process of the graphene to the grid reduces the amount of Si but increases significantly the Au content.

7.2 Cleaning graphene

To improve the cleanness of graphene, in order to make it a suitable substrate for HRTEM investigations, standard surface cleaning methods were used and optimized (thermal cleaning), reported procedures were tested (using catalysts[98]) and new approaches for cleaning graphene were developed (dry-cleaning).

Thermal cleaning of graphene

Desorption energies for n-alkanes (n= 5 – 60) on graphite range between 65 ±2.4 — 289 ±7.7 kJ/mole but the desorption energy does not vary linearly with the chain length. Their peak desorption temperatures range between 164 – 728 K for

n= 5 to n= 60 respectively.[99] Thus the whole range of n-alkanes (n= 5 – 60) can be desorbed from the surface of graphite by heating the material up to $\sim 450°C$.

As seen from the XPS measurements carbonaceous material is present on the graphene sample. Under the electron beam these carbonaceous material can be cracked and pinned to the graphene. As demonstrated by Meyer et al.[24] the electron beam in the TEM can be used as an electron-beam induced deposition technique (EBID), i.e., using the contamination and the e-beam patterns of cracked carbon can be design in the surface of graphene. Although this technique can be used to produce graphene based electronic devices, EBID of hydrocarbons is neither desirable for the investigation of the intrinsic properties of graphene nor for the characterisation of nanomaterials on a graphene substrate by HRTEM. As an example of EBID of hydrocarbons, MC-graphene without annealing was irradiated with 80 keV electrons at a dose rate of $\sim 10^8 e^-/nm^2\,s$. With continuous irradiation the contamination kept building up until only thick amorphous carbon covered the surface. Figure 7.2.1 shows the sample after EBID of hydrocarbons at the edge of the e-beam. In addition to sample cleanness, the lack of EBID of hydrocarbons during imaging can be used as a measure of the effectiveness of a cleaning treatment.

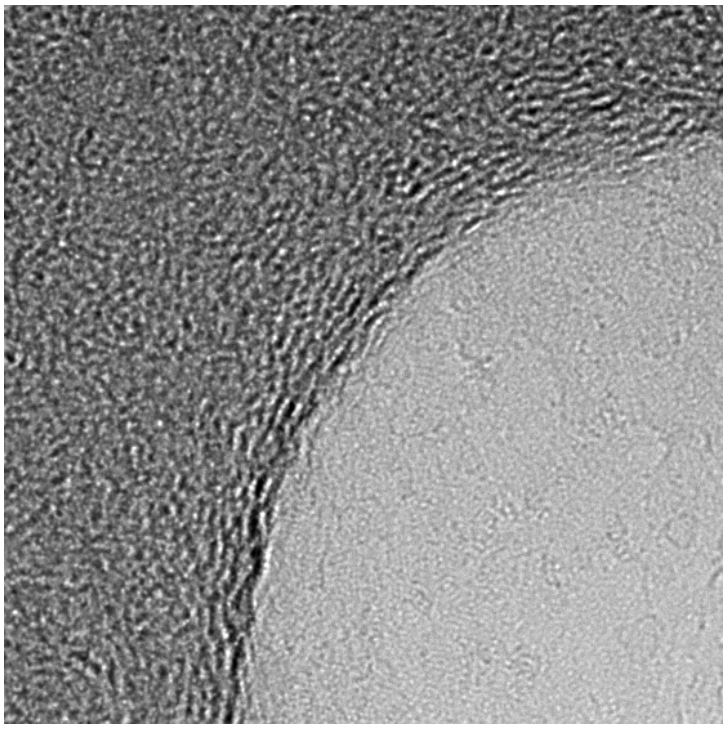

Figure 7.2.1. HRTEM image of EBID of hydrocarbons on graphene.

Annealing graphene in air

A MC-graphene sample was annealed in a heating plate in air at 200°C for 10 minutes and then inserted in the TEM. The sample was not heated at higher temperatures to avoid grid destruction and possible oxidization of graphene. Figure 7.2.2 shows an image of graphene after 2 hours of e-beam irradiation where no EBID of hydrocarbons was observed. Results in this experiment show that the clean areas of graphene range between 1 nm^2 – 5 x 10^2 nm^2. The cleanness was determined to be $\sim$ 6%, which is around the same value of the clean areas found in a non-annealed sample. In summary: annealing of graphene in air does avoid the EBID of hydrocarbons but it does not improve the cleanness.

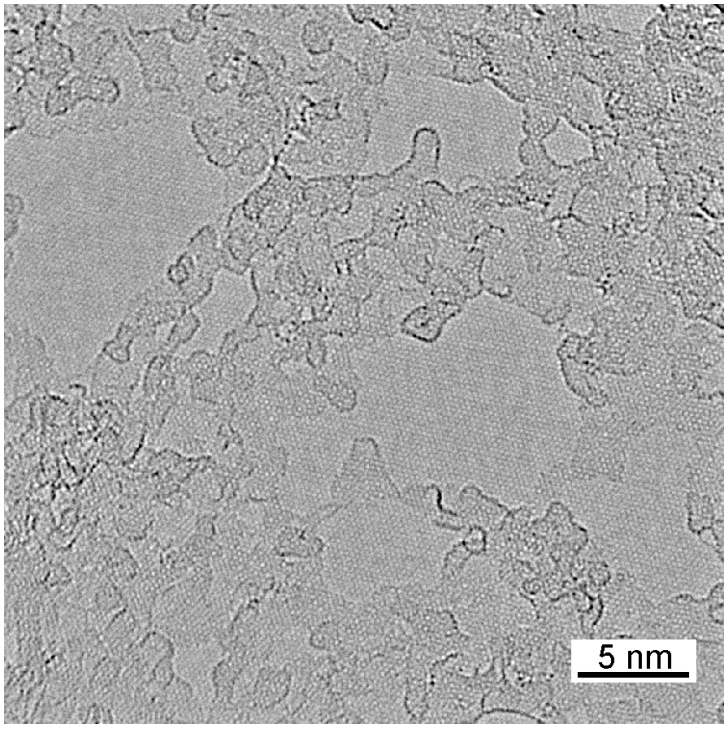

Figure 7.2.2. Low magnification TEM image of a graphene sample after annealing in air.

Annealing graphene in UHV

As mention before, annealing in air induces some type of cleaning on graphene, but in order to obtain larger clean areas much more contamination must be removed. By raising the temperature during annealing more energy is introduced to desorb larger hydrocarbon molecules, however, annealing at high temperatures in air conveys, on one hand, the oxidization of graphene (due to the presence of oxygen in the air), and on the other hand the destruction of the grid to which the graphene has

been transferred to. To overcome these drawbacks a graphene sample was annealed for 12 hours in UHV ($\sim$ 1 x 10^{-10} mbar) and the temperature was set near the limit of the heating element, i.e. 500°C .

Figure 7.2.3 shows a low magnification image of graphene after UHV annealing. This sample, as expected, did not show hydrocarbon deposition under the e-beam. Moreover, the size of the clean areas of graphene reach up to $\sim$ 2.5 x 10^5 nm^2 which is a significant improvement as compare to those areas obtained for the sample annealed in air.

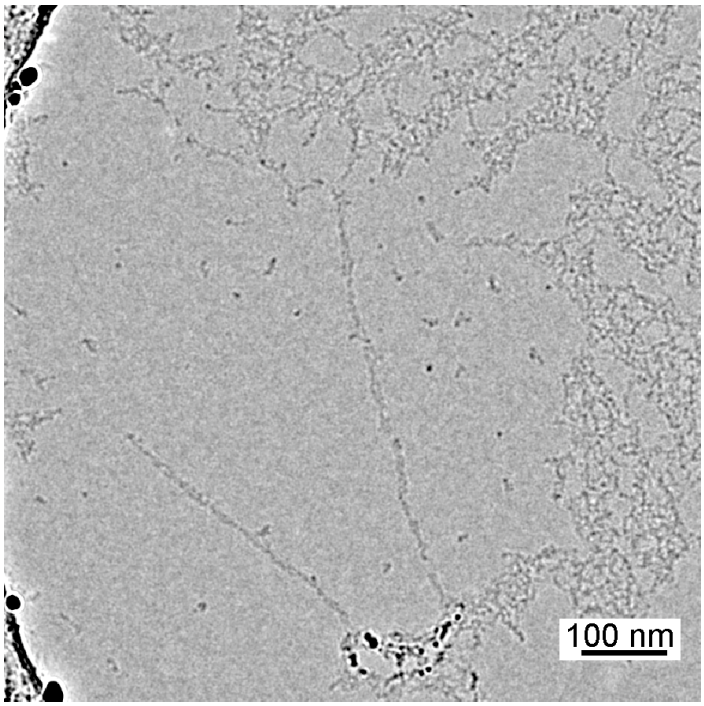

Figure 7.2.3. Low magnification TEM image of a graphene sample after annealing in UHV.

By TEM imaging is not possible to know or to discriminate the type of contamination that have been removed or the one that remained on the surface of graphene after annealing. It is known, for Au(111) and graphite surfaces, that larger and more complex hydrocarbons need higher activation energies for desorption.[99,100] This information leads to suggest that: (1) the reached temperature in the annealing process in UHV was not high enough; (2) the annealing time was too short to complete the removal of contamination; (3) the residual contamination is made, perhaps, of more complex or crosslinked hydrocarbons. Nevertheless, annealing in UHV showed to be a more effective cleaning method for graphene, reaching cleanness between 30 – 40 %.

Cleaning graphene by Pt-metal catalysis

Recently a cleaning method of graphene was reported[98] which resulted in 100 % graphene cleanness. This cleaning method relies upon the catalytic properties of platinum or palladium and moderate temperatures (300°C) to completely clean the graphene surface. Samples prepared following the reported procedure [i] (CVD-graphene/Si_3N_4 at 300°C for 30 minutes) were imaged by HRTEM to corroborate the cleaning effectiveness. The results show that graphene covering a hole (500 nm diameter) is atomically clean over the whole area that it spans (Figure 7.2.4).

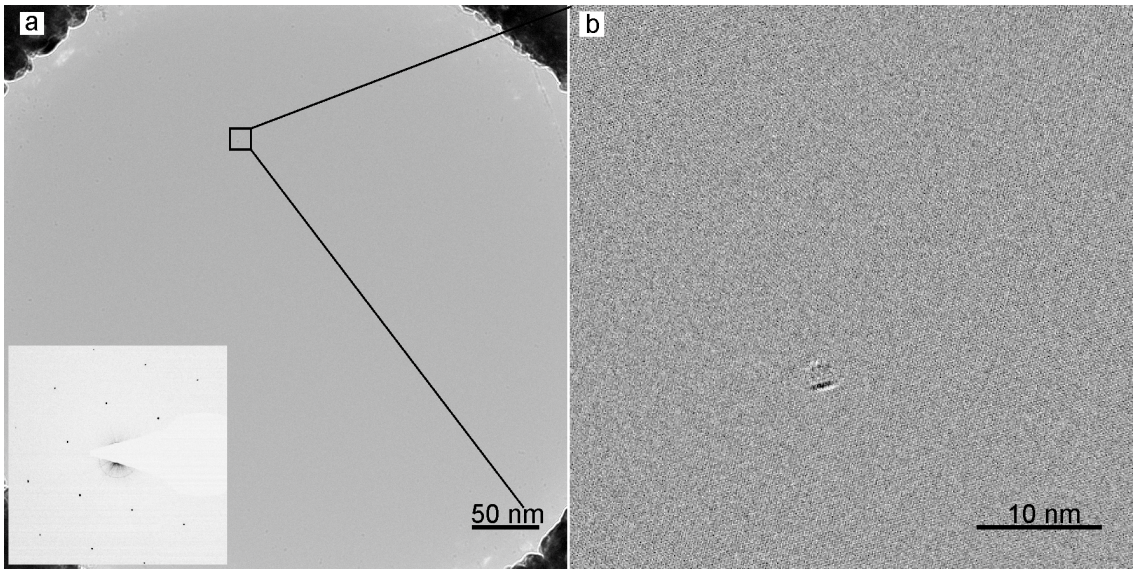

Figure 7.2.4. Cleaning graphene by Pt-metal catalysis. (a) Low magnification image of a 500 nm hole diameter covered with ultraclean graphene. Inset shows SAED pattern where the graphene reflexes are observed. (b) Averaged HRTEM image of clean graphene, the spot in the centre is a residual contamination.

At the magnification used in Figure 7.2.4 (a) it is not possible to distinguish the cleaned graphene from the vacuum but its existence is proven by SAED as seen in the inset. At higher magnification (Figure 7.2.4 (b)) the graphene lattice can be observed along with a small residual adsorbate. With these results the total cleanness of graphene by Pt-catalysis has been corroborated.

[i] Samples fabricated by Dr. Jean-Nicolas Longchamp. Physics Institute, University of Zurich, Zurich, Switzerland.

7.3 Dry-cleaning of graphene

Algara-Siller G., Lehtinen O., Turchanin A., Kaiser U. Dry-cleaning of graphene. Applied Physics Letters **2014**, 104, 153115.[101]

Porous structures (adsorbents) are widely used to remove or filter undesirable materials in a medium, commonly in liquid or in gas. The molecules they adsorb are commensurate to the size of the pores. The physical and chemical properties of the adsorbent, e.g. surface area, of the adsorbent are key, but not the only, factors for the adsorption properties. For example, activated alumina (dehydroxylated aluminium hydroxide) with high surface area has a large loading capacity for water, thus, it is normally used as desiccant and filter in production processes. Another example, molecular sieve 5A (the calcium form of an aluminosilicate matrix) with a pore size of 5 Å adsorbs molecules that fit through its pores, e.g. from Helium (2 Å) to Propylene (5 Å).[ii] A carbon based adsorbent — activated carbon — is a porous complex matrix with a large surface area, broad range of pore sizes (micropores, macropores an mesopores, <2 nm, >50 nm and between 2-50 nm respectively), and high adsorption capacity.[102] These 3 mentioned adsorbents were, therefore, used as dry-cleaning agents for graphene.

Materials and methods for dry-cleaning

Activated alumina[iii] and molecular sieve 5A[iv] beads were crushed to granulates in a mortar to increase the contact to the surface of graphene. The granulated adsorbents placed on a glass vial were regenerated at 300°C for 30 minutes and let to cool to $\sim$ 200°C, all under ambient conditions. The graphene samples were then embedded in the adsorbents for 30 minutes. Dry-cleaning of graphene with activated carbon (powder form) followed different methodology. The graphene sample was embedded in the activated carbon and then the temperature was raised by 5°C/minute from room temperature to $\sim$210°C and held for 30 minutes. All samples were let to cool down to room temperature. Before inserting each sample in to the TEM, they were blown gently to remove residual adsorbent granulates and particles.

[ii] Sigma-Aldrich technical information bulletin.
[iii] Edwards, Wilmington, MA, USA.
[iv] Sigma–Aldrich Co. LLC.

Characterisation of dry-cleaned graphene

The cleanness, ratio of contamination-free area to the total sample area, was obtained by analysis of low magnification HRTEM images for each sample.

Activated alumina

Figure 7.3.1 (a) shows a graphene sample after dry-cleaning with activated alumina, the cleanness on the sample varied between 15-40%. It was found that almost every hole with single-layer graphene had an atomically clean area which could reached up to $\sim 0.24\ \mu m^2$ (e.g. Figure 7.3.1 (b)). At high magnification (inset), the atomically cleanness of graphene is proved.

Molecular sieve 5A

A graphene sample which was dry-cleaned with molecular sieve 5A is shown in Figure 7.3.1 (c and d). After analysis of low magnification images, the cleanness resulted in 10-30% showing clean areas up to $0.06\ \mu m^2$. The dry-cleaning with molecular sieve 5A resulted, also, in atomically clean graphene as observed in the inset.

Activated carbon

In contrast to the other two adsorbents, activated carbon is highly effective in cleaning the contamination on graphene. The clean areas of graphene were, except for some residual contamination, as big as the holes ($\sim 1.2\ \mu m^2$), thus yielding to about 95% cleanness (Figure 7.3.1 (e and f)).

Table 7.3.1. Table summarizing the effectiveness of dry-cleaning methods

Sample	Cleanness [%]	Areas [μm^2]
Activated Alumina	15-40	0.24
Molecular sieve 5A	10-30	0.06
Activated Carbon	95	1.2

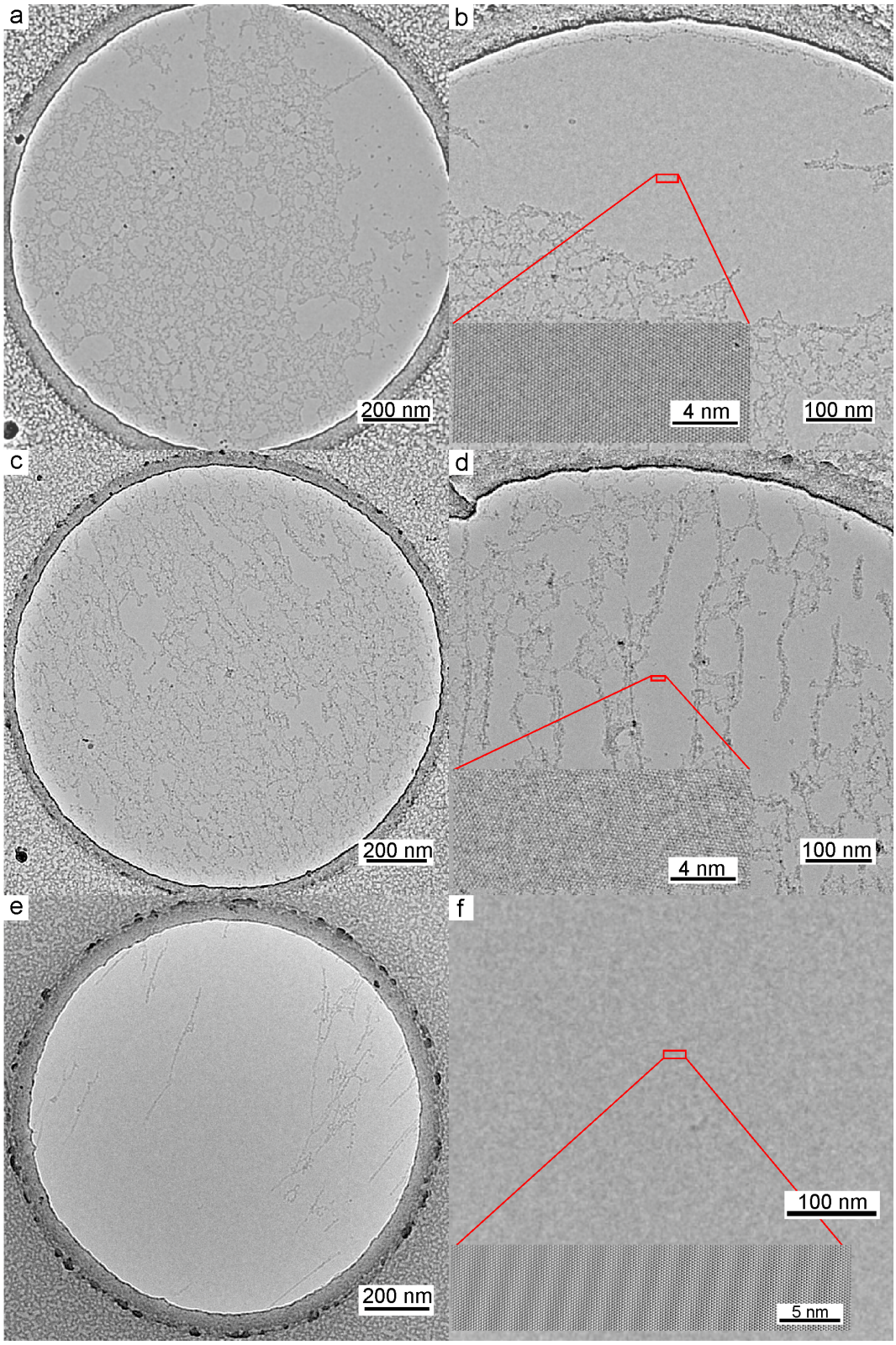

Figure 7.3.1. TEM images of dry-cleaning graphene with activated alumina (a and b), molecular sieve 5A (c and d) and activated carbon (e and f). Obtained cleanness for the three samples are 15-40%, 10-30% and $\sim$ 95%, respectively. The images (b, d and f) are examples of large clean areas in each of the samples. The insets are high magnification HRTEM images from the areas delimited by the red boxes, showing that the graphene samples have been atomically cleaned.

Characterisation of residual contamination after dry-cleaning

The residual contamination after the dry-cleaning methods can be described, as a first instance, by its appearance. For all dry-cleaning methods, the contamination laying on the surface of graphene is in a stripe-like form (see Figures 6.2.1, 6.2.6, 7.3.1) and in some cases the stripes of contamination converge towards residual adsorbent particles (Figure 7.3.2). Thus the observable stripes suggest that there were diffusion pathways to the adsorbents. To assert this evidence, detailed investigation of diffusion and adsorption should be performed with the right characterisation techniques, such investigations are out of the scope of this work.

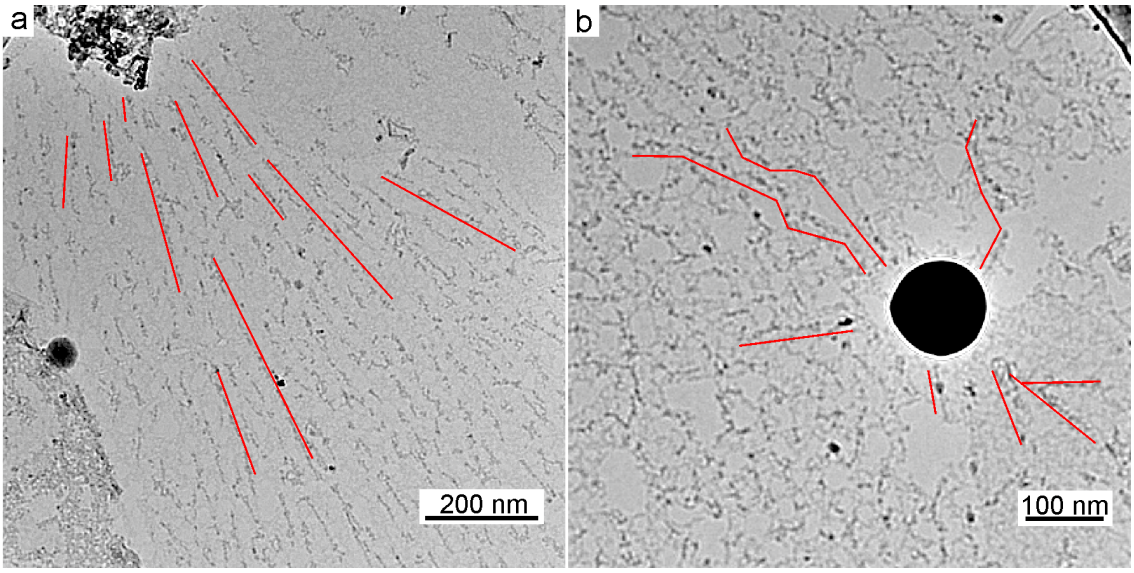

Figure 7.3.2. Examples of residual contamination after dry-cleaning treatment. Images (a and b) show stripe-like shape of the residual contamination which converge towards non-removed adsorbents. In this case the adsorbent is molecular sieve 5A.

The residual contamination after dry-cleaning with activated alumina and molecular sieve 5A has the appearance of carbonaceous contamination after qualitative comparison to the contamination of non-cleaned samples. Moreover, the carbonaceous nature of the residual contamination is affirmed by the growth of graphene adlayers from contamination under electron beam irradiation as described in Section 6.2.

Dry-cleaning with activated carbon, unlike with the other adsorbents, left behind contamination which due to its strong contrast can be regarded as non-carbonaceous contamination (see comparison in Figure 7.3.3), moreover this contamination crystallises by applying high electron doses.

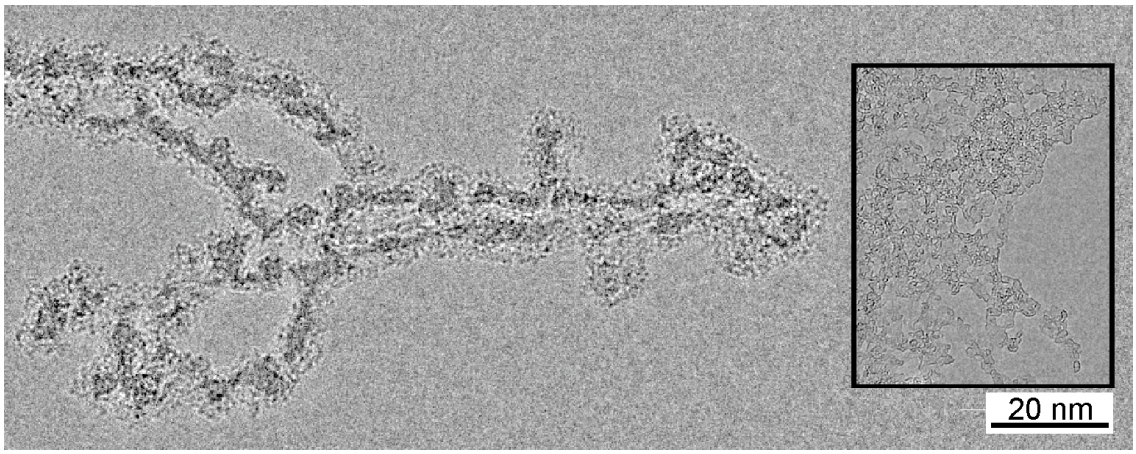

Figure 7.3.3. TEM image of residual contamination on graphene cleaned with activated carbon. In the inset TEM image of a non-cleaned graphene. The contamination on the dry-cleaned sample has stronger contrast and do not resemble the carbonaceous contamination of non-cleaned graphene(inset image).

Residual contamination characterised by EELS

Contrary to XPS, with EELS is possible to get local, elemental, and quantitative information of the residual contamination on free-standing graphene. EELS characterisation (at 80 kV) was performed on a CVD-graphene sample which was dry-cleaned with activated carbon. Three areas of interest were spotted within the sample: (1) Clean graphene, (2) non-cleaned graphene and (3) an area on graphene with residual contamination with high contrast, i.e. non-carbonaceous.

A clear indicator of the removal of carbonaceous contamination, apart from the cleanness shown by HRTEM, is the change in the features of the plasmon $\pi+\sigma$ peak in EELS. A comparison of the EEL spectra between cleaned and non-cleaned graphene is seen in Figure 7.3.4. The excitations at 10 eV and 20 eV in the plasmon peak of the non-cleaned graphene indicate additional carbon species,[103] while the observable difference in the peaks intensity is correlated to the amount of carbon material that was removed by the activated carbon. Effectively, dry-cleaning with activated carbon has remove carbonaceous contamination from the graphene surface. Nonetheless, as seen in Figures 7.3.1 (e) and 7.3.3, after dry-cleaning with activated carbon some contamination remains on the graphene.

To obtained the elemental composition of the residual contamination, an area with this type of contamination was studied with EELS by scanning over an energy-loss range between 0 eV and 600 eV (convergence angle $\sim$1 mrad and collection angle

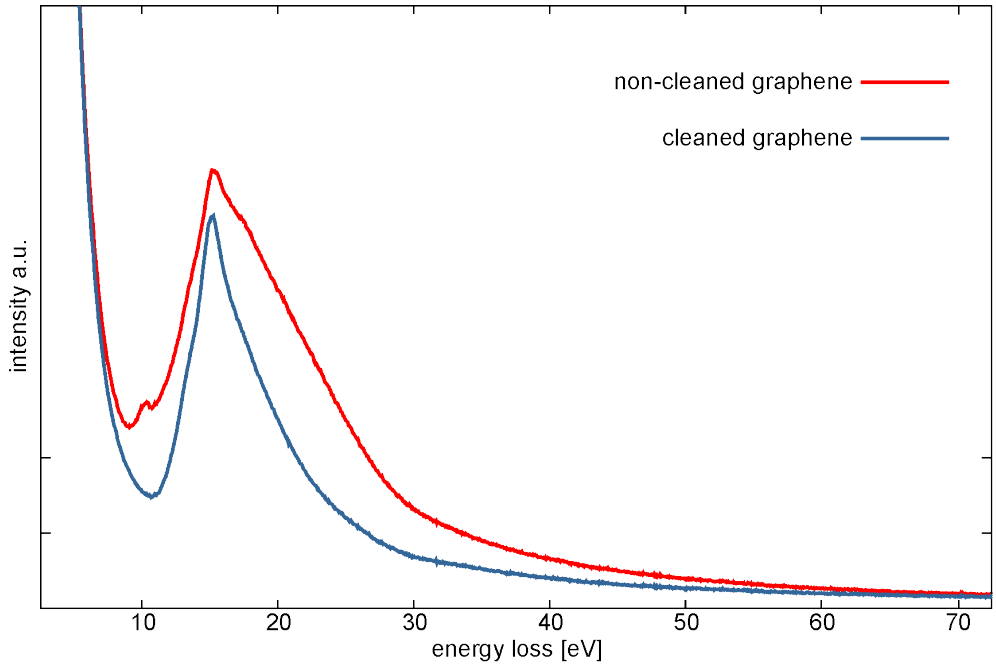

Figure 7.3.4. Two low-loss spectra of the C plasmon region ($\pi + \sigma$) of non-cleaned and cleaned graphene (red and blue respectively). The difference in their features is apparent and indicates a change in the amount of carbon material as for the carbon species.

3.3 mrad).

In the energy-loss range 95–165 eV, a set peaks was found (Figure 7.3.5). The peaks at 105 eV and 108 eV are distinctive of the Si-$L_{2,3}$ ionization edge for Si containing compounds.[104,105] The EELS results agree with the non-local XPS measurements of the contamination of a CVD-graphene sample, where Si is a prominent element in the sample and Quantifoil. The existence of Au in the residual contamination could not be obtained by the EELS studies because of the high energy-loss edge for Au (Au M_5 edge at 2206 eV).

Cleaning of bilayer and multilayer graphene

The cleaning methods reported in the last sections were performed in CVD-graphene which consists mostly of single-layer graphene but occasionally patches of bilayer or triplelayer are observed. It was found that the effects of cleaning by all the presented methods do not take place on bilayer or triplelayer graphene (Figure 7.3.6). Panels (a–c) show graphene that was cleaned with: UHV annealing, Pt-metal catalyst and activated carbon, respectively. These images demonstrate that the bilayers (delimited by the blue line) and the triplelayer (red line) remain, indeed, contaminated. It is interesting that the remaining contamination on these layered patches resembles hydrocarbon contamination, as seen in Figure 7.3.6 (d).

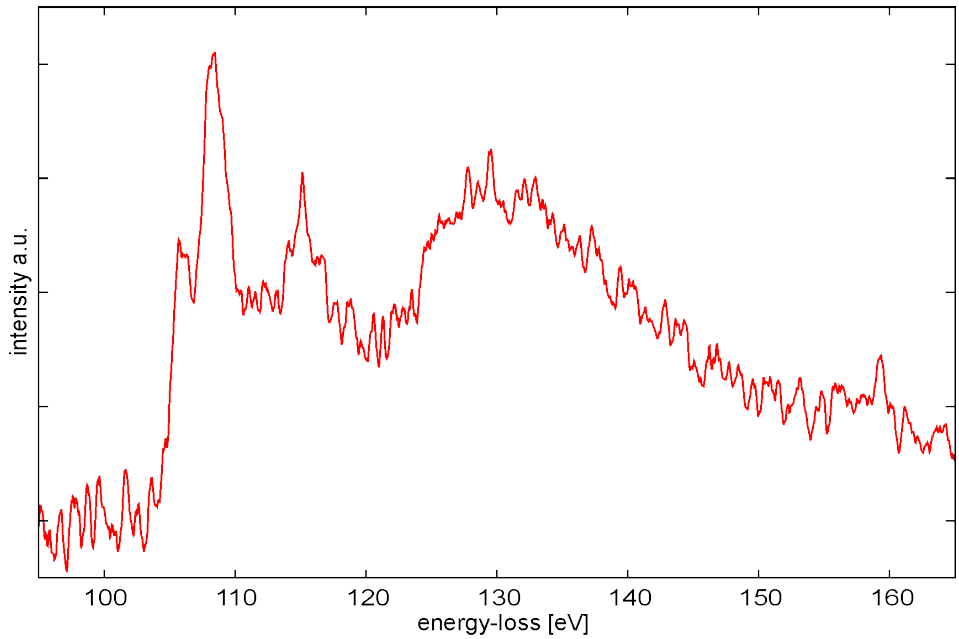

Figure 7.3.5. Background subtracted EEL spectrum (95–165 eV) of an area with residual contamination. Shape and position of peaks correspond to the Si $L_{2,3}$ ionization edge.

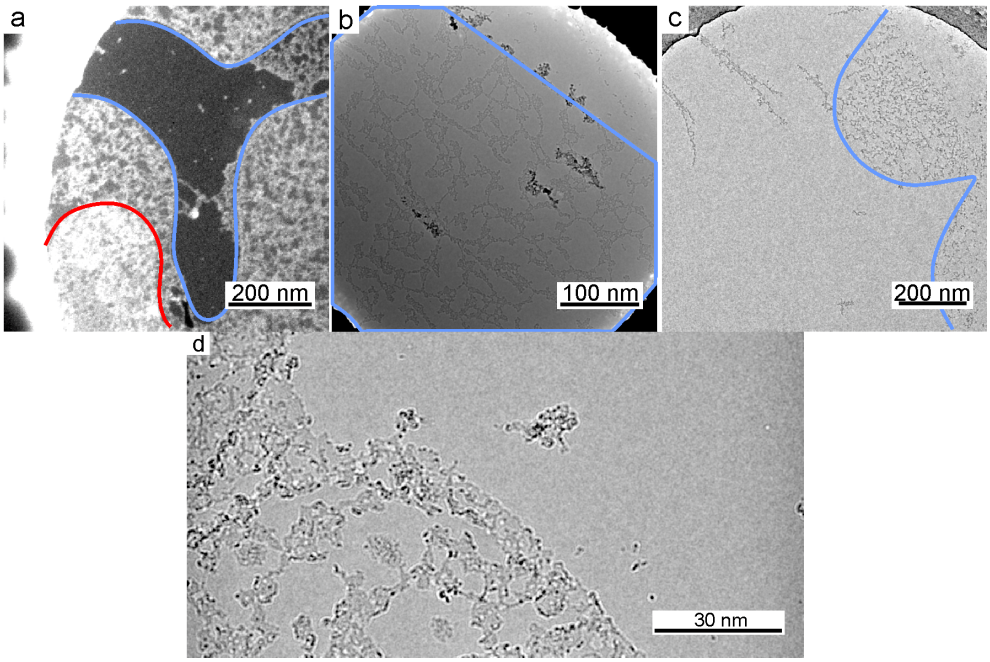

Figure 7.3.6. Images of graphene cleaned by: (a) UHV annealing (DF image), (b) Pt-metal catalyst and (c and d) dry-cleaning with activated carbon (HRTEM image). Patches of bilayer graphene (blue lines) and triplelayer (red line) remain contaminated. In (a) contamination is seen as bright features. (d) High magnification HRTEM image of the remnant contamination on bilayer graphene, in appearance similar to hydrocarbon contamination.

A clear explanation for this effect is beyond the topic of this thesis. However, based on recent literature on the translucency behaviour of single-layer graphene on another graphene layer (substrate)[106] it is possible to postulate that: by increasing the number of graphene substrate layers (limited to the value of range of the vdW interactions between adsorbates and the substrate),[99,107] the adsorption (desorption) energy of the contamination in bilayer or trilayer graphene is higher compared to single-layer graphene. Therefore a higher temperature during cleaning is required for desorption and/or migration of the contamination in order to clean bilayer and triple-layer graphene.

§ 8 Conclusions

The work presented in this thesis contributed to publications in various fields of research: materials science, chemistry and biology. The work is based on the use of a transmission electron microscope as analytical tool and on graphene. The wide range of characterisation capabilities achieved by the former have allowed the full characterisation of the latter. With the combination of the two, nano-objects were studied, the pristine structure of 2D materials described, new structures were fabricated, and atom dynamics unveiled.

Three differently produced graphene samples were investigated by TEM using SAED, DF and HRTEM techniques. The characterisation of the samples allowed to obtain the quality of each graphene, which was assessed based on grain size, defects and number of layers. Additionally, some structural characteristics such as the stacking configuration of bilayer graphene, i.e. turbostratic stacking, were related to the exhibited optical properties.

Once graphene was fully characterised, it was used as a substrate for TEM imaging of nano-objects. One important part that enabled this work was the development of graphene substrate preparation techniques, sample deposition methods and imaging conditions. The studied nano-objects (Au NCs, QDs, and nanodiamond with NVs) were created for biological applications such as drug delivery, biosensors and biolabeling. From their investigation by HRTEM, information about size, dispersion and structure was acquired. Transmission electron microscopy experiments on DNA deposited on graphene showed that the graphene treatment and the optimization of the sample deposition used in this work are further steps towards direct imaging of biological samples. Furthermore, with these experiments it was possible to corroborate the low signal contribution of graphene to the image and, also, the feasibility of graphene as substrate for transmission electron microscopy.

In another set of experiments, graphene was used as protective layer to reduce radiation damage in order to enable imaging the pristine structure of beam-sensitive two dimensional materials (MoS_2 and g-C_3N_4). The effects of radiation damage protection by graphene layers have been quantified by encapsulating MoS_2 between

graphene layers and obtaining the vacancy production cross-section. Also, with this set up it was possible to described the pristine structure of MoS_2 and to elucidate the elemental termination of the MoS_2 edges, a characteristic that directly relates to the electronic and magnetic properties of the material. The structure of g-C_3N_4, a two dimensional semiconductor, was described by the analysis of the HRTEM images and their FFTs. The position of atoms and the stacking configuration of g-C_3N_4 were obtained by doing complementary image calculations and compare the results to the experimental images.

Bilayer graphene was used as raw material to create by electron-beam engineering an one dimensional carbon nanostructure, i.e. SWCNT. It was shown by theoretical calculations that the formed SWCNT was flattened due to the van der Waals interactions of the bilayer graphene to which the SWCNT is attached to.

In other experiments, single-layer graphene with residual contamination served as surface template to grow a new graphene adlayer by the electron beam. The source of the carbon atoms for the graphene adlayer was the residual contamination. Due to the spatial resolution achieved by HRTEM imaging, the growth rate of the graphene adlayer was measured, and its crystallinity and edge termination were described.

Two layers of graphene encapsulating water allowed the formation of a new form of ice —square ice— at room temperature. The structure of square ice was fully described by image analysis, theoretical simulations and image calculations. Additionally, this experiment proved that phase transformations of matter in the two dimensional regime differ from phase transformations of bulk.

An occurring problem throughout this thesis was the contamination on the surface of graphene because, this contamination hindered the potential of TEM to image desirable and interesting details from all the studied samples. Existing methods to clean graphene were tried and characterised by TEM in order to measure and corroborate their efficiency to clean graphene. Although the cleaning methods showed to be efficient, these methods involve either UHV annealing or the deposition of metal-catalysts on the grid which for some applications are not suitable or desirable.

Thus, in this work we have developed a new method to remove the contamination from the surface of graphene by using common adsorbents — dry-cleaning—. This new method renders graphene effectively clean, i.e. $\sim$ 95% cleanness, enabling studies of pristine graphene and making graphene the ultimate substrate for TEM investigations.

Bibliography

[1] Reimer, L.; Kohl, H. *Transmission electron microscopy*, 5th ed.; Springer Science+Media: New York, 2008.

[2] Erni, R. *Aberration-corrected imaging in transmission electron microscopy*, 1st ed.; Imperial College London: London, 2010.

[3] Rose, H. H. *Philosophical Transactions of the Royal Society A* **2009**, *367*, 3809–23.

[4] Rose, A. *Adv. Elelctron* **1948**, *1*.

[5] Michelson, A. *Studies in Optics*, 1st ed.; The University of Chicago Press: Chicago, 1927.

[6] Peli, E. *Journal of the Optical Society of America. A* **1990**, *7*, 2032–40.

[7] Kukkonen, H.; Rovamo, J.; Tiippana, K.; Näsänen, R. *Vision Resolution* **1993**, *33*, 1431–1436.

[8] Williams, D.; Carter, C. B. *Transmission Electron Microscopy*, 2nd ed.; Springer Science+Media: New York, 2009.

[9] Mott, N.; Masey, H. *The theory of atomic collisions*; Oxford University Press: New York, 1965.

[10] Rutherford, E. *Philosophical Magazine* **1911**, *21*, 669–688.

[11] Pantelic, R. S.; Meyer, J. C.; Kaiser, U.; Stahlberg, H. *Solid State Communications* **2012**, *152*, 1375–1382.

[12] Novoselov, K. S.; Geim, A. K.; Morozov, S. V.; Jiang, D.; Zhang, Y.; Dubonos, S. V.; Grigorieva, I. V.; Firsov, A. A. *Science* **2004**, *306*, 666–9.

[13] Wallace, P. R. *Physical Review* **1947**, *71*, 622–634.

[14] Geim, A. K. *Science* **2009**, *324*, 1158877.

[15] Castro Neto, A. H.; Guinea, F.; Peres, N. M. R.; Novoselov, K. S.; Geim, A. K. *Reviews of Modern Physics* **2009**, *81*, 109–162.

[16] Lee, C.; Wei, X.; Kysar, J. W.; Hone, J. *Science* **2008**, *321*, 385–8.

[17] Frank, O.; Tsoukleri, G.; Parthenios, J.; Papagelis, K.; Riaz, I.; Jalil, R.; Novoselov, K. S.; Galiotis, C. *ACS Nano* **2010**, *4*, 3131–3138.

[18] Soldano, C.; Mahmood, A.; Dujardin, E. *Carbon* **2010**, *48*, 2127–2150.

[19] Girifalco, L. a.; Lad, R. a. *The Journal of Chemical Physics* **1956**, *25*, 693–697.

[20] Zhang, Y.; Small, J. P.; Pontius, W. V.; Kim, P. *Applied Physics Letters* **2005**, *86*, 073104.

[21] Blake, P.; Hill, E. W.; Castro Neto, A. H.; Novoselov, K. S.; Jiang, D.; Yang, R.; Booth, T. J.; Geim, A. K. *Applied Physics Letters* **2007**, *91*, 063124(3).

[22] Li, X.; Cai, W.; Colombo, L.; Ruoff, R. S. *Nano letters* **2009**, *9*, 4268–72.

[23] Li, X.; Cai, W.; An, J.; Kim, S.; Nah, J.; Yang, D.; Piner, R.; Velamakanni, A.; Jung, I.; Tutuc, E.; Banerjee, S. K.; Colombo, L.; Ruoff, R. S. *Science* **2009**, *324*, 1312–4.

[24] Meyer, J. C.; Girit, C. O.; Crommie, M. F.; Zettl, A. *Applied Physics Letters* **2008**, *92*, 123110 (1–3).

[25] Pantelic, R. S.; Suk, J. W.; Magnuson, C. W.; Meyer, J. C.; Wachsmuth, P.; Kaiser, U.; Ruoff, R. S.; Stahlberg, H. *Journal of structural biology* **2011**, *174*, 234–8.

[26] Meyer, J.; Eder, F.; Kurasch, S.; Skakalova, V.; Kotakoski, J.; Park, H.; Roth, S.; Chuvilin, A.; Eyhusen, S.; Benner, G.; Krasheninnikov, A.; Kaiser, U. *Physical Review Letters* **2012**, *108*, 1–6.

[27] Meyer, J.; Geim, A.; Katsnelson, M.; Novoselov, K.; Obergfell, D.; Roth, S.; Girit, C.; Zettl, A. *Solid State Communications* **2007**, *143*, 101–109.

[28] Huang, P. Y.; Ruiz-Vargas, C. S.; van der Zande, A. M.; Whitney, W. S.; Levendorf, M. P.; Kevek, J. W.; Garg, S.; Alden, J. S.; Hustedt, C. J.; Zhu, Y.; Park, J.; McEuen, P. L.; Muller, D. A. *Nature* **2011**, *469*, 389–392.

[29] Lehtinen, O.; Kurasch, S.; Krasheninnikov, A. V.; Kaiser, U. *Nature Communications* **2013**, *4*, 1–7.

[30] Lenski, D. R.; Fuhrer, M. S. *Journal of Applied Physics* **2011**, *110*, 013720.

[31] Campos-Delgado, J.; Botello-Méndez, A. R.; Algara-Siller, G.; Hackens, B.; Pardoen, T.; Kaiser, U.; Dresselhaus, M. S.; Charlier, J.-C.; Raskin, J.-P. *Chemical Physics Letters* **2013**, *584*, 142–146.

[32] Mø lhave, K.; Gudnason, S. B.; Pedersen, A. T.; Clausen, C. H.; Horsewell, A.; Bø ggild, P. *Ultramicroscopy* **2007**, *108*, 52–57.

[33] Girit, C. O.; Meyer, J. C.; Erni, R.; Rossell, M. D.; Kisielowski, C.; Yang, L.; Park, C.-H.; Crommie, M. F.; Cohen, M. L.; Louie, S. G.; Zettl, A. *Science* **2009**, *323*, 1705–1708.

[34] Campos-Delgado, J.; Algara-Siller, G.; Santos, C. N.; Kaiser, U.; Raskin, J.-P. *Small* **2013**, *9*, 3247–3251.

[35] Bistritzer, R.; MacDonald, A. H. *PNAS* **2011**, *108*, 12233–7.

[36] Mann, S. *Nature materials* **2009**, *8*, 781–92.

[37] Daniel, M.-C.; Astruc, D. *Chemical reviews* **2004**, *104*, 293–346.

[38] Zheng, J.; Nicovich, P. R.; Dickson, R. M. *Annual review of physical chemistry* **2007**, *58*, 409–431.

[39] Xie, J.; Zheng, Y.; Ying, J. Y. *Journal of the American Chemical Society* **2009**, *131*, 888–9.

[40] Pramanik, G. Near infrared emitting nanoemitters for bioimaging applications. Ph.D. Thesis, Ulm University, 2013.

[41] Wu, Y.; Eisele, K.; Doroshenko, M.; Algara-Siller, G.; Kaiser, U.; Koynov, K.; Weil, T. *Small* **2012**, *8*, 3465–3475.

[42] Amelia, M.; Avellini, T.; Monaco, S.; Impellizzeri, S.; Yildiz, I.; Raymo, F. M.; Credi, A. *Pure and Applied Chemistry* **2011**, *83*, 1–8.

[43] Zhang, B.; Zhang, Y.; Mallapragada, S. K.; Clapp, A. R. *ACS nano* **2011**, *5*, 129–138.

[44] Ermakova, A.; Pramanik, G.; Cai, J.-M.; Algara-Siller, G.; Kaiser, U.; Weil, T.; Tzeng, Y.-K.; Chang, H. C.; McGuinness, L. P.; Plenio, M. B.; Naydenov, B.; Jelezko, F. *Nano Letters* **2013**, *13*, 3305–3309.

[45] Gruber, A.; Dräbenstedt, A.; Tietz, C.; Fleury, L.; Wrachtrup, J.; von Borczyskowski, C. *Science* **1997**, *276*, 2012–2014.

[46] Theil, E. C. *Annual review of biochemistry* **1987**, *56*, 289–315.

[47] Kleinschmidt, A.; Zhang, R. *Z. Naturforschung* **1959**, *14b*, 770–779.

[48] Banfield Younghusband, H.; Inman, R. *Annual review of biochemistry* **1974**, *43*, 605–619.

[49] Nair, R. R.; Blake, P.; Blake, J. R.; Zan, R.; Anissimova, S.; Bangert, U.; Golovanov, A. P.; Morozov, S. V.; Geim, A. K.; Novoselov, K. S.; Latychevskaia, T. *Applied Physics Letters* **2010**, *97*, 153102.

[50] Calladine, C. R.; Drew, H. R.; Luisi, B.; Travers, A. *Understanding DNA*, 3rd ed.; Elsevier Academic Press: London, 2004.

[51] Singh, N.; Jabbour, G.; Schwingenschlögl, U. *The European Physical Journal B* **2012**, *85*, 392.

[52] Jin, C.; Lin, F.; Suenaga, K.; Iijima, S. *Physical Review Letters* **2009**, *102*, 195505.

[53] Meyer, J. C.; Chuvilin, A.; Algara-siller, G.; Biskupek, J.; Kaiser, U. *Nano* **2009**, *9*, 2683–2689.

[54] Komsa, H.-P.; Kotakoski, J.; Kurasch, S.; Lehtinen, O.; Kaiser, U.; Krasheninnikov, A. V. **2012**, *109*, 035503.

[55] Algara-Siller, G.; Severin, N.; Chong, S. Y.; Björkman, T.; Palgrave, R. G.; Laybourn, A.; Antonietti, M.; Khimyak, Y. Z.; Krasheninnikov, A. V.; Rabe, J. P.; Kaiser, U.; Cooper, A. I.; Thomas, A.; Bojdys, M. J. *Angewandte Chemie (International ed. in English)* **2014**, *53*, 1–6.

[56] Teter, D. M.; Hemley, R. J. *Science* **1996**, *271*, 53–55.

[57] Algara-Siller, G.; Kurasch, S.; Sedighi, M.; Lehtinen, O.; Kaiser, U. *Applied Physics Letters* **2013**, *103*, 203107.

[58] Radisavljevic, B.; Radenovic, A.; Brivio, J.; Giacometti, V.; Kis, A. *Nature Nanotechnology* **2011**, *6*, 147–50.

[59] Brivio, J.; Alexander, D. T. L.; Kis, A. *Nano letters* **2011**, *11*, 5148–53.

[60] Bollinger, M.; Lauritsen, J.; Jacobsen, K.; Nø rskov, J.; Helveg, S.; Besenbacher, F. *Physical Review Letters* **2001**, *87*, 196803.

[61] Botello-Méndez, A. R.; López-Urías, F.; Terrones, M.; Terrones, H. *Nanotechnology* **2009**, *20*, 325703.

[62] Krasheninnikov, A. V.; Banhart, F. *Nature Materials* **2007**, *6*, 723–33.

[63] Algara-Siller, G.; Santana, A.; Onions, R.; Suyetin, M.; Biskupek, J.; Bichoutskaia, E.; Kaiser, U. *Carbon* **2013**, *65*, 80–86.

[64] Chuvilin, A.; Meyer, J. C.; Algara-Siller, G.; Kaiser, U. *New Journal of Physics* **2009**, *11*, 083019.

[65] Jin, C.; Lan, H.; Peng, L.; Suenaga, K.; Iijima, S. *Physical Review Letters* **2009**, *102*, 205501–4.

[66] Chuvilin, A.; Kaiser, U.; Bichoutskaia, E.; Besley, N. A.; Khlobystov, A. N. *Nature Chemistry* **2010**, *2*, 450–453.

[67] Fischbein, M. D.; Drndić, M. *Applied Physics Letters* **2008**, *93*, 113107.

[68] Song, B.; Schneider, F.; Xu, Q.; Dekker, C.; Zandbergen, H. *Nano Letters* **2011**, *11*, 2247–2250.

[69] Charlier, J. C.; De Vita, A.; Blase, X.; Car, R. *Science* **1997**, *275*, 647–649.

[70] Liu, Z.; Suenaga, K.; Harris, P. J. F.; Iijima, S. *Physical Review Letters* **2009**, *102*, 015501–4.

[71] Rotkin, S.; Gogotsi, Y. *Materials Research Innovations* **2002**, *5*, 191–200.

[72] Chopra, N.; Benedict, L.; Crespi, V.; Cohen, M.; Louie, S.; Zettl, A. *Nature* **1995**, *377*, 135–138.

[73] Qi, L.; Yu, J.; Feng, J.; Li, J. *Carbon* **2010**, *48*, 2354–2360.

[74] Yang, L.; Han, J. *Physical Review Letters* **2000**, *85*, 154–7.

[75] Gülseren, O.; Yildirim, T.; Ciraci, S. *Physical Review B* **2002**, *65*, 153405(4).

[76] da Silva, L. B.; Fagan, S. B.; Mota, R. *Nano Letters* **2004**, *4*, 65–67.

[77] Westenfelder, B.; Meyer, J. C.; Biskupek, J.; Kurasch, S.; Scholz, F.; Krill III, C. E.; Kaiser, U. *Nano Letters* **2011**, *11*, 5123–5127.

[78] Barreiro, A.; Börrnert, F.; Avdoshenko, S. M.; Rellinghaus, B.; Cuniberti, G.; Rümmeli, M. H.; Vandersypen, L. M. K. *Scientific reports* **2013**, *3*, 1115.

[79] Zan, R.; Ramasse, Q. M.; Bangert, U.; Novoselov, K. S. *Nano Letters* **2012**, *12*, 3936–40.

[80] Yazyev, O. V.; Louie, S. G. *Physical Review B* **2010**, *81*, 195420.

[81] Koskinen, P.; Malola, S.; Häkkinen, H. *Physical Review Letters* **2008**, *101*, 115502.

[82] Koskinen, P.; Malola, S.; Häkkinen, H. *Physical Review B* **2009**, *80*, 16–18.

[83] Choi, E.-M.; Yoon, Y.-H.; Lee, S.; Kang, H. *Physical Review Letters* **2005**, *95*, 085701.

[84] Klein, J.; Kumacheva, E. *Science* **1995**, *269*, 816–819.

[85] Gavish, M.; Wang, J.; Eisenstein, M.; Lahav, M.; Leiserowitz, L. *Science* **1992**, *256*, 815–818.

[86] Zangi, R.; Mark, A. E. *Physical Review Letters* **2003**, *91*, 025502.

[87] Zangi, R.; Mark, A. E. *The Journal of Chemical Physics* **2003**, *119*, 1694.

[88] Nair, R. R.; Wu, H. a.; Jayaram, P. N.; Grigorieva, I. V.; Geim, a. K. *Science* **2012**, *335*, 442–4.

[89] Zheng, Y.; Su, C.; Lu, J.; Loh, K. P. *Angewandte Chemie (International ed. in English)* **2013**, *52*, 8708–12.

[90] Yuk, J. M.; Park, J.; Ercius, P.; Kim, K.; Hellebusch, D. J.; Crommie, M. F.; Lee, J. Y.; Zettl, A.; Alivisatos, A. P. *Science* **2012**, *336*, 61–4.

[91] Xu, K.; Cao, P.; Heath, J. R. *Science* **2010**, *329*, 1188–91.

[92] Koga, K.; Gao, G. T.; Tanaka, H.; Zeng, X. C. *Nature* **2001**, *412*, 802–5.

[93] Balandin, A. A. *Nature Materials* **2011**, *10*, 569–81.

[94] Pop, E.; Varshney, V.; Roy, A. K. *MRS Bulletin* **2012**, *37*, 1273–1281.

[95] Zhu, Y.; Murali, S.; Cai, W.; Li, X.; Suk, J. W.; Potts, J. R.; Ruoff, R. S. *Advanced Materials* **2010**, *22*, 3906–24.

[96] Davidson, S. *Metrologia* **2003**, *40*, 324–338.

[97] Cumpson, P.; Sano, N. *Metrologia* **2013**, *50*, 27–36.

[98] Longchamp, J.-N.; Escher, C.; Fink, H.-W. *Journal of Vacuum Science & Technology B* **2013**, *31*, 020605.

[99] Paserba, K. R.; Gellman, A. J. *The Journal of Chemical Physics* **2001**, *115*, 6737.

[100] Wetterer, S. M.; Lavrich, D. J.; Cummings, T.; Bernasek, S. L.; Scoles, G. *Journal of Physical Chemistry B* **1998**, *102*, 9266–9275.

[101] Algara-Siller, G.; Lehtinen, O.; Turchanin, A.; Kaiser, U. *Applied Physics Letters* **2014**, *104*, 153115.

[102] Bansal, R. C.; Donnet, J.-B.; Stoeckli, F. *Active carbon*, 1st ed.; Marcel Dekker, Inc.: New York, USA., 1988.

[103] Rhinow, D.; Weber, N.-E.; Turchanin, A. *The Journal of Physical Chemistry C* **2012**, *116*, 12295–12303.

[104] Lichtenberger, O.; Woltersdorf, J.; Hering, N.; Riedel, R. *Zeitschriff für anorganische und allgemeine Chemie* **2000**, *626*, 1881–1891.

[105] Schulmeister, K.; Mader, W. *Journal of Non-Crystalline Solids* **2003**, *320*, 143–150.

[106] Shih, C.-J.; Strano, M. S.; Blankschtein, D. *Nature Materials* **2013**, *12*, 866–9.

[107] Londero, E.; Karlson, E. K.; Landahl, M.; Ostrovskii, D.; Rydberg, J. D.; Schröder, E. *Journal of physics. Condensed Matter* **2012**, *24*, 424212.

List of publications

1. **Experimental observation of boron-nitride chains.** O. Cretu, H.-P. Komsa, O. Lehtinen, G. Algara-Siller, U. Kaiser, K. Suenaga, A.V. Krasheninnikov.
   Submitted (2014)

2. **Direct imaging of square ice in graphene nanochannels.** G. Algara-Siller, O. Lehtinen, F.C. Wang, R.R. Nair, U. Kaiser, H.A. Wu, A.K. Geim, I.V. Grigorieva.
   Submitted (2014)

3. **Triazine-based graphitic carbon nitride: a two-dimensional semiconductor.** G. Algara-Siller, N. Severin, S.Y. Chong, T. Björkman, R.G. Palgrave, A. Laybourn, M. Antonietti, Y.Z. Khimyak, A.V. Krasheninnikov, J.P. Rabe, U. Kaiser, A.I. Cooper, A. Thomas, M.J. Bojdys.
   Angewandte Chemie Int. Ed., 53 (2014)

4. **Dry-cleaning of graphene.** G. Algara-Siller, O. Lehtinen, A. Turchanin, U. Kaiser.
   Applied Physics Letters, 104 (2014)

5. **The pristine atomic structure of MoS_2 monolayer protected from electron radiation damage by graphene.** G. Algara-Siller, S. Kurasch, M. Sedighi, O. Lehtinen, U. Kaiser.
   Applied Physics Letters, 103 (2013).

6. **CVD synthesis of mono- and few-layer graphene using alcohols at low hydrogen concentration and atmospheric pressure.** J. Campos-Delgado, A.R. Botello-Méndez, G. Algara-Siller, B. Hackens, T. Pardoen, U. Kaiser, M.S. Dresselhaus, J-C. Charlier, J-P. Raskin.
   Chemical Physics Letters, 548 (2013).

7. **Detection of few metallo-protein molecules using color centers in nanodiamonds.** A. Ermakova, G. Pramanik, G. Algara-Siller, U. Kaiser, T. Weil, H.C. Chang, L.P. McGuinness, M.B. Plenio, B. Naydenov, F. Jelezko.
   Nano Letters, 13 (2013).

8. **Electron-beam engineering of single-walled carbon nanotubes from bilayer graphene.** G. Algara-Siller, A. Santana, R. Onions, M. Suyetin, J. Biskupek, E. Bichoutskaia, U. Kaiser.
   Carbon, 65 (2013).

9. **Twisted bi-layer graphene: microscopic rainbows.** J. Campos- Delgado, G. Algara-Siller, C.N. Santos, U. Kaiser, J.-P. Raskin.
   Small, 9 (2013).

10. **A quantum dot photoswitch for DNA detection, gene transfection, and live-cell imaging.** Y. Wu, K. Eisele, M. Doroshenko, G. Algara-Siller, U. Kaiser, K. Koynov, T. Weil.
    Small, 8 (2012)

11. **Graphene-based sample supports for in-situ high-resolution TEM electrical investigations.** B. Westenfelder, J.C. Meyer, J. Biskupek, G. Algara-Siller, J. Kusterer, U. Kaiser, C. Krill and F. Scholz.
    Journal of Physics D, 44 (2011)

12. **Experimental analysis of charge redistribution due to chemical bonding by high-resolution transmission electron microscopy.** J. C. Meyer, S. Kurasch, H. J. Park, V. Skakalova, D. Kuenzel, A. Gross, A. Chuvilin, G. Algara-Siller, S. Roth, T. Iwasaki, U. Starke, J. H. Smet and U. Kaiser.
    Nature Materials, 4 (2011)

13. **Single carbon atom chains. Synthesis and dynamics of one- dimensional carbon Species.** G. Algara-Siller, J.C. Meyer, A. Chuvilin and U. Kaiser.
    Imaging & Microscopy, 12, (2010) Editorial invitation. Non-peer reviewed. Re-printed in G.T.I. Laboratory Journal (Europe), 15 (2011)

14. **From graphene constrictions to single carbon chains.** A. Chuvilin, J.C. Meyer, G. Algara-Siller and U. Kaiser.
    New Journal of Physics, 11 (2009)

15. **Selective sputtering and atomic resolution imaging of atomically thin boron nitride membranes.** J.C. Meyer, A. Chuvilin, G. Algara-Siller, J. Biskupek, U. Kaiser.
    Nano Letters, 9 (2009)

List of Figures

Declaration

I declare that the presented Dissertation (doctoral thesis) was written independently without external support and that it is an original work. All statements which are literally or analogously taken from other than own publications have been identified as quotations and/or properly cited.

Ilmenau, 2014

Acknowledgements

I want, here, to express my gratitude to all people that have in some way or another shaped my education, to those who have been beside me along this long way, to those with whom I have spent laughs and love, and to those who are caring about me at the distance.

Recognition should be given to Prof. Ute Kaiser who enabled my experiments, studies and much more, also to Prof. Uwe Ritter who admitted me as his Ph.D. student.

Thanks to CONACyT-DAAD fellowship for the economic support.